Light Quark Fields in QCD: Numerical Simulations and Chiral Perturbation Theory

Dissertation
zur Erlangung des Doktorgrades
des Fachbereichs Physik
der Universität Hamburg

vorgelegt von
Enno E. Scholz
aus Norden/Ostfriesland

Hamburg
2005

Gutachter der Dissertation:	Prof. Dr. István Montvay Prof. Dr. Jochen Bartels
Gutachter der Disputation:	Prof. Dr. István Montvay Prof. Dr. Klaus Fredenhagen
Datum der Disputation:	12. Juli 2005
Vorsitzender des Prüfungsausschusses:	Prof. Dr. Gerhard Mack
Vorsitzender des Promotionsausschusses:	Prof. Dr. Günter Huber
Dekan des Fachbereichs Physik:	Prof. Dr. Günter Huber

Abstract

The interplay between numerical simulations of Quantum Chromodynamics on a lattice and Chiral Perturbation Theory is studied. We will demonstrate that by using partially quenched analysis techniques it is possible to extract Low Energy Constants from lattice simulations. The quark mass dependence of squared meson masses and meson decay constants extracted from our lattice data is investigated. Also the expectations for the (zero temperature) phase structure of Wilson fermions near zero quark masses are discussed and compared to the numerical outcome. A major topic will be, the way how twisted mass fermions facilitate reaching light quark masses in simulations with dynamical Wilson fermions. Modifications arising from this formulation in the TSMB-update algorithm, the definition and measurement of relevant quantities, as well as the Chiral Perturbation Theory formulae and the phase structure scenarios will be presented.

Zusammenfassung

Das Zusammenwirken zwischen numerischen Quantenchromodynamik-Simulationen auf dem Gitter und Chiraler Störungstheorie wird untersucht. Die Möglichkeit, mit Hilfe von sogenannten „partially quenched“ („teilweise unterdrückten“) Analysetechniken Werte für die Niederenergiekonstanten aus den Gittersimulationen zu erhalten, wird anhand unserer Daten demonstriert. Dafür wird die Quarkmassenabhängigkeit der quadrierten Mesonmassen und der mesonischen Zerfallskonstanten untersucht. Die möglichen Szenarien für die Phasenstruktur mit Wilson-Fermionen in der Nähe verschwindender Quarkmassen (auf Temperatur $T = 0$ Gittern) werden vorgestellt und mit unseren numerischen Resultaten verglichen. Ein Schwerpunkt bildet die Untersuchung, in welcher Weise Fermionen mit gedrehter Masse („twisted mass“) die Simulation leichter Quarkmassen mit dynamischen Wilson-Fermionen verbessern können. Die hierbei erforderlichen Anpassungen im TSMB-Update Algorithmus und bei der Definition sowie Messung relevanter Größen werden ebenso vorgestellt werden wie die nötigen Änderungen in den Formeln der Chiralen Störungstheorie sowie deren Auswirkungen auf die Phasenstrukturszenarien.

Contents

Introduction **1**

1 QCD on a lattice **5**

1.1 Formulation of QCD in discretized space-time 5

1.2 Measurement of basic quantities 7

1.2.1 Sommer-scale r_0/a 8

1.2.2 Correlators and masses 9

1.2.3 Error analysis 12

2 QCD with a twisted mass term **15**

2.1 The QCD$^{\mathrm{TM}}$ action 15

2.2 $\mathcal{O}(a)$ improvement 17

2.2.1 Improved correlators 18

2.2.2 Automatic improvement at full twist 20

2.2.3 Possible caveat 21

2.2.4 Critical mass 21

2.3 Currents, densities, and renormalization factors 21

2.3.1 Ward-Takahashi identities 22

2.3.2 Renormalized currents 26

2.4 Measurement of relevant quantities 26

2.4.1 Twist angle 28

2.4.2 Renormalization factors 29

2.4.3 Pion decay constant 29

2.4.4 Quark mass 30

3 QCD near zero quark mass **33**

3.1 Continuum χPT 33

3.2 Lattice χPT 37

3.2.1 Lattice artifacts in untwisted QCD . . . 37
3.2.2 χPT$^{\mathrm{TM}}$ . . . 39
3.3 The phase structure of lattice QCD . . . 40
3.3.1 Aoki- and normal-scenario . . . 40
3.3.2 Phase structure of QCD$^{\mathrm{TM}}$ . . . 42

4 Partially quenched QCD **47**
4.1 Pion masses and decay constants from PQχPT . . . 49
4.1.1 Sea quark mass dependence . . . 50
4.1.2 Valence quark mass dependence . . . 51
4.1.3 $\mathcal{O}(a^2)$ corrections . . . 53
4.1.4 NNLO-corrections . . . 53
4.2 PQχPT$^{\mathrm{TM}}$ . . . 54

5 Numerical simulations **57**
5.1 Updating algorithms . . . 57
5.1.1 Metropolis, Heatbath, Overrelaxation . . . 58
5.1.2 Boson algorithm: TSMB . . . 59
5.2 LECs from untwisted $N_f = 2$ simulations . . . 66
5.2.1 Numerical cost . . . 67
5.2.2 Partially quenched analysis . . . 69
5.2.3 Chiral fits from runs using the DBW2 gauge action . . . 79
5.2.4 Summary . . . 82
5.3 QCD$^{\mathrm{TM}}$ and phase structure studies . . . 83
5.3.1 Metastabilities and phase transitions . . . 84
5.3.2 Improved gauge actions . . . 88
5.3.3 Z-factors and pion decay constant from QCD$^{\mathrm{TM}}$-simulations . . . 95

Conclusions **101**

A Notations and conventions **103**

B Improved gauge actions **107**

C Update and measurement routines **109**

References **115**

Nicht allein in Rechnungssachen
Soll der Mensch sich Mühe machen;
Sondern auch der Weisheit Lehren
Muß man mit Vergnügen hören.

Wilhelm Busch, *Max und Moritz*

Introduction

Today it is widely accepted that four fundamental forces describe the interactions between elementary particles: the gravitational, electro-magnetic, weak, and strong force. A consistent description of the latter three by quantum field theory exists, which is known to be the *Standard Model (SM)* of elementary particle physics. Historically led by the success to describe the electro-magnetic interactions by a $\mathrm{U}(1)_E$ gauge theory, *Quantum Electrodynamics (QED)*, the SM unifies the electro-magnetic and the weak interactions to a $\mathrm{SU}(2)_W \otimes \mathrm{U}(1)_Y$ electro-weak gauge theory (formulated by Glashow, Weinberg, and Salam, *GWS-theory*). A $\mathrm{SU}(3)_C$ gauge theory, *Quantum Chromodynamics (QCD)*, describes the strong interactions. Another ingredient to the SM is the Higgs-mechanism, which dynamically generates the masses of the elementary particles. In QED the bosonic force carrier between (electro-magnetically) charged particles is known to be the photon, while the weak force carriers are the W- and Z-bosons. The strong interaction is mediated between color charged particles by the *gluons*, the gauge-bosons of QCD. The fermionic elementary particles are the *leptons* (e, ν_e; μ, ν_μ; τ, ν_τ) and *quarks* (up, down; charm, strange; top, bottom). Up to now it is experimentally observed that both appear in three families. These particles are characterized by different quantum numbers and each of them is accompanied by an antiparticle. The leptons only interact electro-weakly according to their charge, while the quarks also interact strongly.

While the leptons and electro-weak gauge bosons are in principle observable as free particles, this is not true for the quarks and gluons for reasons which will be explained later. Observed are the hadrons, which are built out of quarks: the mesons (π, K, ρ, ...), consisting of a quark and an antiquark, and the baryons (proton, neutron, Δ, Ξ, ...), which are bound states made out of three quarks. The baryons, which are of fermionic character, form the nuclear matter. The mesons, being of bosonic character, can be seen as the residual force carriers of QCD, which interact between baryons to result in the nuclear forces. From a historic point of view, the *quark model* was introduced by Gell-Mann and Zweig in 1964: all the particles observed by that time (i.e., hadrons, sometimes called the "particle zoo") could be grouped into families of particles with similar masses and showing characteristic patterns of the isospin and strangeness quantum numbers. Examples are the pseudo-scalar meson octet or the baryon octet and decuplet. The quark model explains this structure with the existence of three different quark flavors (with todays knowledge the three lightest ones: up, down, and strange). This was known as the "Eightfold Way". Mathematically speaking, the arrangement into the families is based on the $\mathrm{SU}(3)_F$ flavor symmetry among the three light quark flavors. This (approximately) realized flavor symmetry is also the basis for *Chiral Perturbation Theory (χPT)*, a phenomenological approach to the low energy region of the strong interactions, first described by Weinberg in 1968 and in 1984 worked out by Gasser and Leutwyler. Applying the quark model observed particles like the Δ^{++} or the Δ^{-} have to consist of three identical quarks in identical states, which would have been forbidden due to Pauli's exclusion principle. The solution, proposed by Gell-Mann and Fritzsch, was to introduce an additional color

charge. They formulated the interactions between these color charges as a $SU(3)_C$ gauge theory: QCD. The charges are allowed to take three different values (often denoted red, green, blue). The afore mentioned "statistics problem" only requires a minimal number of different colors $N_C = 3$. But from experimental data, e.g., the $\pi_0 \to 2\gamma$ decay or the total cross section for e^+e^- annihilation into hadrons, one deduces $N_C = 3$ to hold for a quantitative agreement.

In contrast to the Abelian nature of the U(1) symmetry group of QED, the SU(3) of QCD is a non-Abelian group. This causes self-couplings among the gluons, which are absent in the case of the photon. This has important consequences: it leads to a running of the coupling constant, which grows towards larger distances (small energies) as found by GROSS and WILCZEK, and independently by POLITZER and also by 'T HOOFT (unpublished). The vanishing of the coupling at small distances is referred to as *asymptotic freedom*. The strong coupling at large distances leads to *color confinement*, explaining the fact that quarks and gluons since being color charged cannot be observed as free particles. Only color neutral states (color singlets) are allowed as free particles. Further this behavior of the coupling renders the application of perturbation theory in the low energy regime impossible. Perturbation theory is based on an expansion in the coupling constant, leading to the FEYNMAN-diagram approach, which proved to be successful in QED. What is needed at low energies is a non-perturbative ansatz, if one wants to extract the low lying hadronic spectrum and decay rates from a first principle approach. Comparing the experimentally measured quantities with the predictions of such a calculation could either exclude or give hints on physics beyond the SM, if a sufficient precision has been reached. Also other theoretically possible states of purely gluonic content (so-called glueballs) can only be treated non-perturbatively.

In 1974, WILSON proposed a regularization procedure for gauge theories, which discretizes a finite box of the Euclidean space-time: the *lattice regularization*. Together with the connection between quantum field theories and statistical mechanics this regularization opened the door for the needed non-perturbative approach. The key is to use Monte Carlo simulation techniques in numerical simulations. But it turned out that the computing power available at that time was not sufficient to produce results referring to full QCD. Over the years not only the computing power evolved (up to now still according to MOORE's law), but also the simulation techniques for incorporating fermion fields (in case of QCD the quarks) improved substantially. The gauge part is not that computationally demanding, therefore the first simulations were done for pure gauge theories. Apart from WILSON's plaquette gauge action, other formulations have been tried, which are claimed to be less sensitive to the introduced discretization. For the fermion part there are different discretization ansätze on the market, each with their own benefits and shortcomings. The original fermion discretization by WILSON explicitly breaks chiral symmetry even at vanishing quark masses. This breaking only disappears as fast as the discretization length is decreased at a fixed physical box size (*continuum limit*). An improvement in the sense that a subgroup of this symmetry remains unbroken is achieved, if the KOGUT-SUSSKIND (staggered) fermion formulation is used. This is computationally cheap, but some mathematically questionable "root-trick" has to be applied, if one wants to deal with a number of fermions different from an integer multiple of four. These problems are all related to the appearance of fermion doublers in lattice discretized theories as shown by the NIELSEN-NINOMIYA-theorem. Using overlap fermions, which respect the GINSPARG-WILSON-relation, or domain-wall fermions, by which a disentanglement of the

chiral limit (i.e., the limit in which explicit chiral symmetry breaking vanishes) from the continuum limit is achieved, circumvents these problems. However, these lattice fermions are computationally very expensive.

Present day lattice QCD simulations are done with two or three dynamical fermions. A rule of thumb is "the lighter—the more expensive", which is generally valid for every fermion discretization. Still it is too costly to aim for realistic light quarks, but the region where low energy effects are to set in has been reached. In this thesis we will study the low energy region by numerical simulations using mainly the *Two-Step Multi-Boson (TSMB)* algorithm invented in 1996 by MONTVAY and here applied for ordinary WILSON-fermions. The interplay between lattice simulations and χPT will be enlightened: the latter can be used for extrapolating the numerical results to realistic light quark masses, while the non-perturbative lattice approach is a first-principle ansatz to bridge between QCD and χPT. Also it will be possible to disentangle lattice discretization errors from the numerical results by using a lattice version of χPT. For the first time dynamical simulations with *twisted mass fermions* as advocated by FREZZOTTI, GRASSI, SINT, and WEISZ are performed, which shed new light on the (zero-temperature) phase structure of lattice QCD near zero quark mass.

This work is organized as follows: in the first chapter we shortly review the formulation of QCD in a finite volume of discretized Euclidean space-time, i.e., on a lattice, using WILSON fermions and plaquette gauge action. The extraction of physically relevant quantities in such a framework is discussed afterwards. The second chapter is devoted to the introduction of (lattice) QCD with a twisted mass term (QCD^{TM}). We show the advantages of this approach in general and in particular for simulating light quark flavors. The renormalization procedure of currents and densities is presented as well as the modifications which arise due to the twisted mass term in measuring various observables. QCD in the vicinity of zero quark mass is considered in Chapter 3. First we briefly discuss χPT in the continuum and apply this to lattice QCD. Also the phase structure of lattice QCD with two flavors of WILSON quarks will be considered within the framework of lattice χPT. Chapter 4 introduces the concept of partial quenching, a method to obtain additional information from dynamical simulations at relatively low computational costs. In the last chapter after a description of how to generate configuration samples (the updating process), we will present our numerical data: We performed a series of simulations aiming for an extraction of *Low Energy* or GASSER-LEUTWYLER *constants (LECs)* from lattice data. A second major topic in our numerical studies is to demonstrate the advantages of twisted mass fermions if light quark flavors are treated numerically. From the outcome of this studies we were able to enlighten the phase structure picture of lattice QCD near zero quark mass, too. The appendix contains a collection of notations and conventions used throughout this work. Here, we also very briefly describe the class of improved gauge actions, which were applied at some stages of our studies with twisted mass QCD. Details about the updating and measuring routines that were developed and used are also postponed to this part.

The numerical simulations were part of two larger projects. The study for the extraction of the LECs from untwisted QCD simulations was done participating in the *qq+q-Collaboration* (DESY Hamburg and Westfälische Wilhelms-Universität Münster). For the dynamical twisted mass simulations and related phase structure studies, we joined into a larger collaboration together with NIC/DESY Zeuthen, Freie Universität Berlin, and Humboldt Universität zu Berlin plus the afore mentioned members of the qq+q-Collaboration.

Chapter 1

QCD on a lattice

1.1 Formulation of QCD in discretized space-time

The Lagrangian of Quantum Chromodynamics (QCD) in Euclidean space-time reads

$$\begin{aligned} \mathcal{L}_{\mathrm{QCD}}[A,\bar{\psi},\psi] &= \frac{1}{4}F^a_{\mu\nu}(x)F^{a\,\mu\nu}(x) \,+\, \bar{\psi}(x)(\not{D}+m)\psi(x) && (1.1)\\ F^a_{\mu\nu} &\equiv \partial_\mu A^a_\nu \,-\, \partial_\nu A^a_\mu \,+\, g f^{abc} A^b_\mu A^c_\nu, && (1.2)\\ \not{D} &= \gamma_\mu D_\mu \,=\, \gamma_\mu\Big(\partial_\mu \,-\, igT^a A^a_\mu\Big). && (1.3) \end{aligned}$$

Here $\bar{\psi}$, ψ are the fields for N_f flavors of quarks. Their masses are summarized in m. F is the field strength tensor of the gluon field A, which also couples to the quark fields via the covariant derivative D_μ with strength g. The T^a are the generators of SU(3), with structure constants f^{abc}.

In what follows we will focus on Wilson's proposal [1] to regularize the theory by discretizing a finite box of the Euclidean space-time. A regularization is needed, e.g., in perturbation theory to treat the occurring divergencies in a proper way. Other possible regularization methods are, e.g., dimensional regularization or Pauli-Villars regularization. The here chosen ansatz will allow for studying QCD non-perturbatively, too.

Formally the continuous space-time Ω_{cont} is now restricted to a set of discretized space-time points $\Omega \subset \mathbb{Z}^4$, $x = x_{\mathrm{cont}}/a \in \Omega$, where a is the lattice spacing. The fields $\bar{\psi}, \psi$ now only "live" on these points. The gauge field connects neighboring points x and $x+\hat{\mu}$ in direction μ, therefore it is expressed in terms of link variables $U_\mu(x) \in \mathrm{SU}(N)$ (in case of QCD: $N=3$), which can be related to the gauge fields:

$$U_\mu(x) \,\equiv\, \exp\Big(igaT^b A^b_\mu(x)\Big). \tag{1.4}$$

Consequently one has for the link connecting x and $x-\hat{\mu}$

$$U_{-\mu}(x) = U^\dagger_\mu(x-\hat{\mu}). \tag{1.5}$$

The lattice version of the QCD action now consists of the gauge part $S_g[U]$ and the fermion part $S_f[U,\bar{\psi},\psi]$. Clearly each of these has to be constructed gauge invariant and in a way that the continuum Lagrangian is reproduced in the limit of vanishing lattice spacing

$a \to 0$ and infinite volume $V \to \infty$, which is referred to as the continuum limit. To build a gauge invariant object out of the link variables, the simplest choice is the plaquette: a closed path in a plane given by two directions μ, ν with side length a and starting point x:

$$U_{\mu\nu}(x) \equiv U_\mu(x) U_\nu(x+\hat{\mu}) U_\mu^\dagger(x+\hat{\nu}) U_\nu^\dagger(x). \tag{1.6}$$

The action described in [1], and therefore referred to as Wilson Plaquette action, is

$$S_g[U] = \beta \sum_x \sum_{\substack{\mu,\nu=1 \\ \mu<\nu}}^{4} \left(1 - \frac{1}{N} \mathrm{ReTr} U_{\mu\nu}(x)\right), \tag{1.7}$$

here β is meant to be the gauge coupling parameter, which is related in the case of a non-Abelian SU(N) to the bare gauge coupling g via

$$\beta = \frac{2N}{g^2}. \tag{1.8}$$

For a fixed renormalized coupling the dependence of the bare coupling on the cut-off introduced by the lattice regularization is given by the Callan-Symanzik renormalization group equations [2, 3].

In case of the fermion action, one has to be aware of the fermion doubling problem. If one discretizes the fermion action naïvely, in d dimensions one would end up with 2^d fermions instead of only one. Because the lattice introduces a momentum cut-off, the fermion propagator encounters poles not only at the origin but also at each corner of the Brillouin zone. Dealing with Wilson fermions [1] this can be cured by adding a mass term of the order $1/a$ for the unwanted doublers. Now these decouple in the continuum limit and one stays with one fermion. The action for Wilson fermions read

$$S_f[U, \bar{\psi}, \psi] = \sum_{x,y} \bar{\psi}(y) \boldsymbol{Q}(y, x; [U]) \psi(x), \tag{1.9}$$

where $\boldsymbol{Q}$ is the fermion matrix:

$$\boldsymbol{Q}(y, x; [U]) \equiv \delta(x, y) - \kappa \sum_{\mu=1}^{4} \Big(\delta(x+\hat{\mu}, y) U_\mu(x) \Big(r + \gamma_\mu\Big) + \delta(x-\hat{\mu}, y) U_\mu^\dagger(x-\hat{\mu}) \Big(r - \gamma_\mu\Big) \Big), \tag{1.10}$$

with κ being the hopping parameter, which is related to the mass parameter $\mu_\kappa = 1/(2\kappa) = am_0 + 4r$. The parameter r in front of the doubler-removing terms is referred to as Wilson parameter ($0 < |r| \leq 1$, usually $r = 1$). This additional term explicitly breaks chiral symmetry as realized in the massless limit of the continuum theory. Therefore, one expects restoration of this symmetry property only in the limit $a \to 0$. Other fermion actions exist like, e.g., the Kogut-Susskind (staggered) action, domain-wall or the overlap-action, which possess improved or even exact chiral symmetry. But either these actions are numerically much more expensive, as it is the case for the domain-wall or overlap-action, or they suffer from other insuffiency, like the "root-trick" for staggered fermions.

Given the action in a discretized formulation, it is now possible to generate ensembles of field configurations by using Monte-Carlo techniques. Details on how the right distribution

according to the QCD-action is obtained are given in Sec. 5.1. Having these ensembles, one can start measuring expectation values of observables $\mathcal{O}$ on them:

$$\langle \mathcal{O} \rangle \;=\; \frac{\int \mathcal{D}[A,\bar{\psi},\psi]\, \mathcal{O}\, e^{-(S_g+S_f)}}{\int \mathcal{D}[A,\bar{\psi},\psi] e^{-(S_g+S_f)}} \tag{1.11}$$

The masses of the quarks have to be tuned via the hopping parameter, while the gauge coupling sets the lattice spacing and therefore also the volume simulated. Details of the measurements and how the scale is set will be described in the remainder of this chapter.

1.2 Measurement of basic quantities

Once a set of gauge field configurations is produced via some simulation techniques, one can start to "measure" physical quantities on this set. Usually while running a simulation only easily obtainable observables are determined like the plaquette expectation value, lowest and highest eigenvalue of the fermion matrix, and the value of the Polyakov-line. These quantities contain useful information to tune the algorithm parameters: the plaquette expectation value signals if the run has reached an equilibrium or is still thermalizing, and the eigenvalues set the bounds $[\epsilon, \lambda]$ for the polynomial approximations used in the TSMB-algorithm (Sec. 5.1.2). Also the autocorrelation of the plaquette is a good estimate for the correlation of the produced field configurations. But to measure some interesting physical quantities, some more effort has to be done.

First it is crucial to determine the physical distance scale of the simulation. One way is to extract it from the Sommer scale parameter r_0 [4, 5]. This will be described in more detail in the following section. Other possibilities to set the scale are using, for instance, the measured mass of the ρ-meson or the pion decay constant, neither of which will be discussed in this work. The different hadronic masses can be measured from correlators with the proper operator insertions as discussed later.

The basic quantities for the above mentioned measurements are the Wilson loops for r_0 and the propagator of the fermion fields for the correlators. The Wilson loop $W(r,t)$ with sides (r,t) is defined as the expectation value of the product of gauge links on all planar rectangular paths with spatial length r and temporal length t. To improve the signal of such a measurement, different smearing techniques on the gauge links may be applied: in this work we choose to use APE-smearing [6], which consists of several steps replacing a gauge link by its original value plus a weighted sum of neighboring spatial gauge links ("staples"). The resulting smeared Wilson loops are then denoted by $W_{ij}(r,t)$, where i,j label the different smearing levels on the two spatial sides of the path.

The propagator of the fermion field is simply given by the inverse of the fermion matrix $\boldsymbol{Q}^{-1}$. This inversion can be done using standard inversion algorithms, like the Conjugate Gradient Solver (CGS) or the (stabilized) Bi-Conjugate Gradient Solver (BiCG(Stab)). Instead of inverting the full matrix $\boldsymbol{Q}[U]$, one solves the equation

$$\boldsymbol{Q}[U]\, x \;=\; s \tag{1.12}$$

for a given source vector s. Because the mentioned inversion-solvers require a Hermitian and positive definite matrix, one practically applies $\tilde{\boldsymbol{Q}}^2$ on the source $\boldsymbol{Q}^\dagger s$ (for the definition of the squared Hermitian fermion matrix $\tilde{Q}^2$ cf. Eq. (5.12)). To speed up the inversions

the preconditioned fermion matrix may be used (cf. Sec. 5.1.2 and App. C). As for the Wilson loops the quality of the extracted quantities improves, too, if some smearing is applied. Our choice was to apply Jacobi-smearing [7] to the point-like source and sink or only to the source. To lower the autocorrelation the source may be chosen randomly on each configuration.

1.2.1 Sommer-scale r_0/a

As proposed by Sommer [4] the scale in dynamical simulations can be set by computing r_0/a from the static quark potential [8, 9, 10]. This method has the advantage that it works well at medium distances, which is comfortable when simulating dynamical quarks. An alternative would be, for instance, to use the "string tension" σ, which would, however, require computations at large distances.

With $F(r)$ being the force between two static quarks at distance r, the Sommer parameter r_0 is defined via

$$r^2\, F(r)|_{r=R(c)} \;=\; c \tag{1.13}$$

by requiring that

$$R(1.65) \equiv r_0 \;\simeq\; 0.49 \text{ fm}, \tag{1.14}$$

where this estimate is given by several phenomenological models. On the lattice the static quark potential is obtained from the Wilson loops:

$$V(r) \;=\; -\lim_{t\to\infty} \frac{1}{t} \log W(r,t). \tag{1.15}$$

If APE-smearing is applied, one can either use just one level of smeared Wilson loops $W_{ii}(r,t)$ or first solve the generalized eigenvalue problem to extract the ground state energy [11]: the solutions of

$$W_{ij}(r,t)\phi(r)_j^{(k)} \;=\; \lambda^{(k)}(r;t,t_0) W_{ij}(r,t_0)\phi(r)_j^{(k)} \tag{1.16}$$

give the eigenvector $\phi(r)_j^{(0)}$ corresponding to the largest eigenvalue $\lambda^{(0)}(r;t_0+1,t_0)$. This is used to project the matrix to the ground state:

$$\tilde{W}_0(r,t) = \phi(r)_i^{(0)}\, W_{ij}(r,t)\, \phi(r)_j^{(0)}. \tag{1.17}$$

Now it is possible to estimate the ground state energy by

$$\tilde{E}_0(r,t) \;=\; \log\left(\frac{\tilde{W}_0(r,t)}{\tilde{W}_0(r,t+1)}\right) \tag{1.18}$$

and obtain the potential $V(r)$ by averaging over different values of $t, t>1$.

Given the potential, one may rewrite Eq. (1.13) as

$$r_0^2 \left.\frac{dV}{dr}\right|_{r_0} \;=\; 1.65 \tag{1.19}$$

and using as a fit ansatz [12]

$$V(\boldsymbol{r}) \;=\; V_0 \;+\; \sigma\, r \;-\, e\left[\frac{1}{\boldsymbol{r}}\right]. \tag{1.20}$$

Finally, one arrives at

$$r_0 \;=\; \sqrt{\frac{1.65 - e}{\sigma}}. \tag{1.21}$$

Here $r = |\boldsymbol{r}|$, and $\left[\frac{1}{\boldsymbol{r}}\right]$ is the tree-level lattice Coulomb term, calculated from

$$\left[\frac{1}{\boldsymbol{r}}\right] \;=\; 4\pi \int \frac{d^3\boldsymbol{k}}{(2\pi)^3}\, \cos(\boldsymbol{k}\boldsymbol{r})\, D_{00}(0,\boldsymbol{k}), \tag{1.22}$$

where D_{00} is the time-time component of the gauge field propagator, which depends on the used gauge action [13, 14].

It is also possible to calculate r_0 by using Eq. (1.13) directly: the force is interpolated by

$$F(r) \;=\; f_1 \;+\; f_2 \frac{1}{r^2}, \tag{1.23}$$

with an estimate for the force at distance r_I:

$$F(r_I) \;=\; V(\boldsymbol{r}) \;-\; V\left(\boldsymbol{r} - \frac{\boldsymbol{r}}{r}\right), \tag{1.24}$$

$$r_I^{-2} \;=\; \left[\frac{1}{\boldsymbol{r}}\right] \;-\; \left[\frac{1}{\boldsymbol{r} - \frac{\boldsymbol{r}}{r}}\right]. \tag{1.25}$$

Another more direct way uses Creutz ratios [15, 16], which are defined as

$$\chi(r,t) \;=\; \frac{W(r,t)W(r-1,t-1)}{W(r,t-1)W(r-1,t)}, \tag{1.26}$$

to extract the force via

$$F(r) \;=\; -\log \chi(r,t). \tag{1.27}$$

1.2.2 Correlators and masses

The zero three-momentum two-point functions or correlators at a time-slice distance $(x_4 - y_4)$ are given by

$$C_{XY}(x_4 - y_4) \;=\; \frac{1}{V_s} \sum_{\boldsymbol{x},\boldsymbol{y}} \left\langle X_x^\dagger Y_y \right\rangle, \tag{1.28}$$

with

$$X_x \;=\; \bar{q}'(x) \Gamma_X q(x). \tag{1.29}$$

V_s denotes the spatial lattice volume. The following pseudo-scalar, axial-vector and vector operators are used for various quantities discussed below:

$$\Gamma_P \;=\; \gamma_5, \tag{1.30}$$

$$\Gamma_{A_4} \;=\; \gamma_4\gamma_5, \tag{1.31}$$

$$\Gamma_{V_i} \;=\; \gamma_i. \tag{1.32}$$

Because of $q(x)\bar{q}(y) = Q_{xy}^{-1}$, one can write

$$C_{XY}(x_4 - y_4) \;=\; \frac{1}{V_s} \sum_{\boldsymbol{x},\boldsymbol{y}} \mathrm{Tr}\left({Q_{yx}^\dagger}^{-1} \gamma_5 \Gamma_X^\dagger Q_{xy}^{-1} \Gamma_Y \gamma_5 \right). \tag{1.33}$$

In practice, once the propagator has been calculated by inverting the fermion matrix, the various correlators can be obtained by insertion of the different operators. If smearing on the source and sink or just on the source is applied one gets correlators C^{ss}_{XY} or C^{ls}_{XY}, respectively. Since the inversion of Q need not necessarily be performed with the same mass parameter (even not with the same fermion action) as was used during the simulation in which the gauge field configuration was produced, it is possible to calculate masses, decay constants etc. of mesons consisting of quarks having masses different from the simulated ones. These quarks are called valence quarks in contrast to sea quarks in the path integral. Valence quarks only appear as final states and not in the virtual quark lines, which were simulated. How such results can be interpreted will be discussed in Chapter 4.

In general the masses and amplitudes are extracted from the asymptotic behavior of the correlators [17]:

$$C_{XY}(t \equiv |x_4 - y_4|) = \frac{\xi^2_{XY}}{2m_p}\left(e^{-m_p t} + (-1)^{X+Y} e^{-m_p(T-t)}\right), \tag{1.34}$$

$$\xi_{XY} = \sqrt{\langle 0|X_0|p\rangle\langle 0|Y_0|p\rangle}. \tag{1.35}$$

Here $|p\rangle$ denotes the zero-momentum state of the particle described by the operators X and Y, which mass is given by m_p. The time parity of the operators X and Y is given by $(-1)^X$ and $(-1)^Y$, respectively. By fitting over a range $[t_{\min}, T/2]$, where T is the lattice extension in time direction, both m_p and ξ_{XY} are obtained. The value $t_{\min}$ is chosen such, that the behavior of the correlators shows a plateau in the effective mass $m_{\text{eff}}(t)$, which is defined implicitly by

$$\frac{C_{XY}(t)}{C_{XY}(t+1)} = \frac{e^{-m_{\text{eff}}(t)\cdot t} + (-1)^{X+Y} e^{-m_{\text{eff}}(t)\cdot(T-t)}}{e^{-m_{\text{eff}}(t)\cdot(t+1)} + (-1)^{X+Y} e^{-m_{\text{eff}}(t)\cdot(T-t-1)}}. \tag{1.36}$$

In the following the physical quantities in question are listed with a brief description how they are obtained. It should be kept in mind, that the extracted quantities from the correlator always come in units of the lattice spacing a. One has to use the scale r_0/a to revert them into physical units.

- **Pion mass m_π**
  The pion mass is simply extracted from the C^{ss}_{PP} correlator by the above described methods: $am_\pi = m_{PP}$. It is also possible to use no smearing (ll) or just smear the source (ls), but the (ss) usually gives a better signal.

- **Rho mass m_ρ**
  In the case of the rho mass one uses the spatial averaged vector correlator

  $$C^{ss}_{VV} = \frac{1}{3}\sum_{i=1}^{3} C^{ss}_{V_iV_i}, \tag{1.37}$$

  and identifies $am_\rho = m_{VV}$.

- **Pion decay constant f_π**
  The pion decay constant is defined by

  $$f_\pi \equiv \frac{\langle 0|A_{4\,0}|\pi\rangle}{m_\pi}. \tag{1.38}$$

A direct way is to use m_π from C_{PP} and fit the correlator $C_{A_4A_4}$ to its asymptotic behavior, and then use $\langle 0|A_{4\,0}|\pi\rangle = \sqrt{\xi^2_{A_4A_4}}$. In the case of low quark masses it turned out, that one gets a better signal if the amplitude-ratio

$$r_{A_4P} = \frac{\langle 0|A_{4\,0}|\pi\rangle}{\langle 0|P_0|\pi\rangle} \tag{1.39}$$

is used, which should be taken from the asymptotic behavior of the correlator-ratio

$$\frac{C^{ls}_{A_4P}(t)}{C^{ls}_{PP}(t)} \;=\; r_{A_4P}\,\tanh\left[m_{PP}\left(\frac{T}{2}-t\right)\right]. \tag{1.40}$$

From the fit of C^{ss}_{PP} one knows m_{PP} and $g^s_\pi = \sqrt{(\xi^{ss}_{PP})^2}$. Also taking ξ^{ls}_{PP} from C^{ls}_{PP} one defines

$$g^l_\pi = \frac{(\xi^{(ls)}_{PP})^2}{g^s_\pi}. \tag{1.41}$$

The decay constant is then evaluated via

$$f_\pi \;=\; \frac{r_{A_4P}g^l_\pi}{m_\pi}. \tag{1.42}$$

Taking into account the renormalization factor Z_A for the lattice axial-vector current, the pion decay constant in lattice units then reads

$$\frac{af_\pi}{Z_A} \;=\; \frac{r_{A_4P}g^l_\pi}{m_{PP}}. \tag{1.43}$$

- **Quark mass m_q** and **m_q^{PCAC}**
  A practical physical definition of the quark mass is to take

$$M_{r_0} \equiv \left(\left(\frac{r_0}{a}\right)(am_\pi)\right)^2, \tag{1.44}$$

which assumes $m_q \propto m^2_\pi$. This relation should hold for small quark masses. By using available lattice data [18] it has been shown [19], that for the strange quark mass one gets

$$M_{r_0,\mathrm{strange}} \;\equiv\; 3.1. \tag{1.45}$$

Therefore:

$$m_q \;=\; \frac{M_{r_0}}{3.1}\,m_{\mathrm{strange}}. \tag{1.46}$$

Also it is possible to extract the quark mass via the partially conserved axial-vector current (PCAC) relation from the correlators:

$$m_q^{\mathrm{PCAC}} \;=\; \frac{\langle 0|\partial_4 A_4|\pi\rangle}{2\langle 0|P|\pi\rangle} \;=\; \frac{f_\pi}{2g^l_\pi}m^2_\pi. \tag{1.47}$$

Again taking renormalization factors for the lattice currents into account, one ends up with

$$Z_q a m_q \;=\; \frac{1}{2}\,r_{A_4P}\,m_{PP} \tag{1.48}$$

with $Z_q = Z_P/Z_A$, and Z_P being the renormalization factor for the pseudo-scalar current.

1.2.3 Error analysis

Unfortunately every quantity determined on the lattice by numerical simulations comes with a statistical error. In addition to the statistical error there are systematic errors, too. The latter may arise from finite volume, finite size effects due to the lattice discretization and other more simulation-dependent issues like in case of the TSMB-algorithm, e.g., the polynomial approximation. The finite size and volume effects can be studied by running simulations with different values for the coupling with the volume fixed or vice versa. Also there are studies, which estimate these effects by Chiral Perturbation Theory (cf. Sec. 3.2.1). Taking this together one should always reach for a systematic error below the statistical one. The statistical error arises because only a finite number of "measurements" is performed, i.e., only a finite number of configurations to sample the path integral is produced. Now we will discuss how to obtain an estimate for the statistical error.

Statistical error for primary quantities

In case of independent configurations with respect to the measured quantity, the simple variance would give a reliable error estimate, otherwise one has to consider the autocorrelation of the measured quantity. First we discuss how to obtain this for a primary quantity, i.e., a directly measured quantity like the expectation value of some correlator. Let $A_\alpha, \alpha = 1, 2, 3, \ldots$ be the exact expectation values of such primary quantities, and $a_\alpha^{(n)}, n = 1, \ldots, N$ the finite sets of measurements. For large enough statistics ($N \gg 1$), one can use $\bar{a}_\alpha$ as an estimate for A_α:

$$A_\alpha \simeq \overline{a_\alpha} \equiv \frac{1}{N} \sum_{i=1}^{N} a_\alpha^{(i)}. \tag{1.49}$$

The error is then given by

$$\sigma(A_\alpha)^2 = \frac{2\tau_{\text{int}}}{N} \left(\overline{a_\alpha^2} - (\overline{a_\alpha})^2 \right), \tag{1.50}$$

where the integrated autocorrelation τ_{int} is taken from the normalized autocorrelation function

$$C_{A_\alpha A_\alpha}(t) = \frac{\langle a_\alpha^{(i)} a_\alpha^{(i+t)} \rangle}{\langle a_\alpha^{(i)} a_\alpha^{(i)} \rangle}, \tag{1.51}$$

by

$$\tau_{\text{int}} = \frac{1}{2} + \sum_{t=1}^{\infty} C_{A_\alpha A_\alpha}(t). \tag{1.52}$$

(In case of independent measurements one has $\tau_{\text{int}} = \frac{1}{2}$ and Eq. (1.50) reduces to the simple variance.)

Statistical error for secondary quantities

The before discussed method does not work for secondary quantities $f(A)$, which are functions of the primary ones like r_0/a or the pion mass. A widely known method is to use so-called Jackknife-blocking, where one determines the error from the deviation of

the results taken on different subsets (blocks) of the measurements. In [20] an advanced method was proposed: the *Linearization method*. The basic assumption is that, again for large enough statistics, the deviation of the considered quantity from the exact ones can be written as

$$f(\overline{a}) - f(A) \simeq \sum_{\alpha} (\overline{a_\alpha} - A_\alpha) \frac{\partial f(A)}{\partial A_\alpha}. \tag{1.53}$$

Here $f(\overline{a})$ is obtained by using the measured (primary) expectation values $\overline{a}$. The values of the derivatives should be constants at the true expectation values and can therefore be estimated by

$$\frac{\partial f(A)}{\partial A_\alpha} \simeq \left.\frac{\partial f(A)}{\partial A_\alpha}\right|_{A=\bar{a}} \equiv \overline{f_\alpha}. \tag{1.54}$$

Now the deviation may be written as

$$f(\overline{a}) - f(A) \simeq \sum_{\alpha} (\overline{a_\alpha} - A_\alpha)\overline{f_\alpha} = \overline{a_{\hat{f}}} - A_{\hat{f}}, \tag{1.55}$$

with

$$A_{\hat{f}} \equiv \sum_{\alpha} A_\alpha \overline{f_\alpha} \tag{1.56}$$

being a linear combination of primary quantities and therefore a primary quantity itself. It can be estimated by

$$\overline{a_{\hat{f}}} \equiv \sum_{\alpha} \overline{a_\alpha}\overline{f_\alpha}. \tag{1.57}$$

The variance of $f(A)$ is given by

$$\sigma^2 \simeq \left\langle (\overline{a_{\hat{f}}} - A_{\hat{f}})^2 \right\rangle, \tag{1.58}$$

where $\langle \ldots \rangle$ denotes an average over an infinite set of different measurements, each with the same statistics. Consequently it is possible to obtain the estimate of the error by the integrated autocorrelation of $A_{\hat{f}}$, which is a primary quantity.

To implement this method one can derive the expressions for $\frac{\partial f(A)}{\partial A_\alpha}$ analytically or numerically by varying the primary quantities. The latter method is very convenient in practical applications and has been used for most of the discussed quantities in this work.

Chapter 2

QCD with a twisted mass term

From a historic point of view, the addition of a twisted mass term to the QCD action can be traced back to the work of Osterwalder and Seiler [21]. A similar term, considered as coupled to an external field, has been used in the investigation of the phase structure of lattice QCD by, e.g., [22, 23, 24, 25]. Recently Frezzotti and Rossi [26] demonstrated that under certain circumstances the twisted mass approach leads to $\mathcal{O}(a)$ improvement of operators without the need of adding counterterms. Another property, which is very interesting from our point of view of simulating light quark masses, is that with this modification the operator in the fermion determinant gets a positive lower bound. This should improve simulations with light quarks, which are plagued by *exceptional configurations*, i.e., configurations with very small eigenvalues, which are not sufficiently suppressed by the fermion determinant. Using the twisted mass QCD action ($\mathrm{QCD}^{\mathrm{TM}}$) in dynamical simulations is nowadays viewed as a candidate for a competition with the numerical fast (but theoretically maybe ill-defined) staggered fermion action [27]. An improved chiral behavior, like for the numerical expensive overlap- or Ginsparg-Wilson fermions, may also be expected [28]. Also it has been advocated, that using $\mathrm{QCD}^{\mathrm{TM}}$ in "four-fermion-physics" is advantageous [29, 30], since wrong parity and chirality mixings are avoidable in the computation of CP-conserving matrix elements of the $\Delta S = 1, 2$ effective weak Hamiltonian.

After defining the $\mathrm{QCD}^{\mathrm{TM}}$ action, we will discuss its improvement property. The remainder of this chapter is devoted to defining and renormalizing the currents properly, and demonstrating how important quantities like the pion mass and decay constant and quark mass can be extracted. Details on the implementation in the numerical simulations and the presentation of numerical results obtained with $\mathrm{QCD}^{\mathrm{TM}}$ will be postponed to Chapter 5.

2.1 The $\mathrm{QCD}^{\mathrm{TM}}$ action

The starting point of $\mathrm{QCD}^{\mathrm{TM}}$ is to combine two fermion flavors u, d into a (chiral) isospin doublet

$$\chi(x) \;=\; \begin{pmatrix} u(x) \\ d(x) \end{pmatrix}$$

and write the fermion action with a *twisted mass term* proportional to $\gamma_5\tau_3$, where τ_3 acts in flavor space. The twisted mass action in the χ- or *twisted basis*, which is the formulation

most suitable in numerical simulations, reads

$$\begin{aligned} S_\chi^{\mathrm{TM}}[U,\bar\chi,\chi] &= \sum_{xy}\bar\chi(y)\Big(\frac{\mathbb{1}_{\mathrm{flavor}}}{2\kappa}Q(y,x;[U]) \;+\; i\mu\,\gamma_5\tau_3\,\delta_{xy}\Big)\chi(x) \\ &\equiv \sum_{x,y}\bar\chi(y)\,Q_\chi^{\mathrm{TM}}(y,x;[U])\,\chi(x), \end{aligned} \tag{2.1}$$

with the (untwisted) fermion matrix Q given by Eq. (1.10) and μ being the twisted mass parameter. For the rest of this chapter we will drop the superscript $^{\mathrm{TM}}$ to keep notations simple. We will refer to

$$\mu_\kappa \;=\; \frac{1}{2\kappa} \;=\; am_0 \;+\; 4r \tag{2.2}$$

as the untwisted bare quark mass in lattice units. Splitting m_0 into a critical mass parameter m_{crit}, at which for vanishing twisted mass parameter $\mu = 0$ the action describes massless quarks, and an offset quark mass $\tilde m$:

$$m_0 \;=\; m_{\mathrm{crit}} \;+\; \tilde m, \tag{2.3}$$

one defines the *twist angle* ω

$$\tan\omega \;=\; \frac{\mu}{a\tilde m}. \tag{2.4}$$

It follows that by definition $\mu_\kappa = \mu_{\kappa\,\mathrm{crit}}$ corresponds to $\omega = \frac{\pi}{2}$ (full twist). Since in a simulation only μ_κ and μ are known a priori, we will have to discuss how to obtain this angle later. For the moment we might use it for the definition of the *physical basis*: by introducing new fields $\bar\psi, \psi$, which are related to the previous ones by a chiral transformation

$$\psi(x) \;\equiv\; \exp\Big[i\frac{\omega}{2}\gamma_5\tau_3\Big]\,\chi(x) \;=\; \Big(\cos\frac{\omega}{2} \;+\; i\gamma_5\tau_3\sin\frac{\omega}{2}\Big)\,\chi(x) \tag{2.5}$$

$$\bar\psi(x) \;\equiv\; \bar\chi(x)\exp\Big[i\frac{\omega}{2}\gamma_5\tau_3\Big] \;=\; \bar\chi(x)\,\Big(\cos\frac{\omega}{2} \;+\; i\gamma_5\tau_3\sin\frac{\omega}{2}\Big), \tag{2.6}$$

and a mass parameter m_q,

$$m_q\cos\omega \;=\; a\tilde m, \;\; m_q\sin\omega \;=\; \mu, \tag{2.7}$$

the action now reads:

$$\begin{aligned} S_{\mathrm{phys}}[\bar\psi,\psi,U] &= \sum_x\Bigg\{m_q\bar\psi(x)\psi(x) \;-\; \frac{1}{2}\sum_{\mu=\pm1}^{\pm4}\bar\psi(x+\hat\mu)U_\mu(x)\gamma_\mu\psi(x) \\ &\quad + \Big[\Big(am_{\mathrm{crit}}+4r\Big)\bar\psi(x) \;-\; \frac{r}{2}\sum_{\mu=\pm1}^{\pm4}\bar\psi(x+\hat\mu)U_\mu(x)\Big]\,\exp[-i\omega\gamma_5\tau_3]\,\psi(x)\Bigg\} \\ &\equiv \sum_{x,y}\bar\psi(y)\,Q_{\mathrm{phys}}(y,x;[U])\,\psi(x). \end{aligned} \tag{2.8}$$

In this basis the twist only appears in the (unphysical) Wilson term, which is needed to remove the fermion doublers. Therefore, we have an action that describes a doublet of mass-degenerate quarks. Mass non-degenerate quarks can be achieved by adding a term

$$\mu_\Delta\tau_1\delta_{xy} \tag{2.9}$$

to Q_χ as proposed in [31][1]. Because of

$$\exp[i\frac{\omega}{2}\gamma_5\tau_3]\,\tau_1\,\exp[i\frac{\omega}{2}\gamma_5\tau_3] \;=\; \tau_1$$

the physical basis can be defined as before, but due to τ_1 the mass term now is non-diagonal. By performing an isospin-rotation around the τ_2 axis, a diagonal mass term can be achieved, too. Defining

$$\hat{\bar{\psi}}(x) \equiv \bar{\psi}(x)\,\frac{1}{\sqrt{2}}(1+i\tau_2), \quad \hat{\psi}(x) \equiv \frac{1}{\sqrt{2}}(1-i\tau_2)\psi(x), \tag{2.10}$$

and simultaneously converting the matrix ($\hat{\bar{\psi}}Q_{\text{phys, diag}}\hat{\psi} = \bar{\psi}Q_{\text{phys}}\psi$):

$$\begin{aligned} Q_{\text{phys, diag}} &= \frac{1}{2}(1-i\tau_2)Q_{\text{phys}}(1+i\tau_2) \\ &= \delta_{xy}\,(m_q \,-\tau_3\mu_\Delta) \,+\, \ldots, \end{aligned}$$

one ends up with fermion fields of masses $m_q + \mu_\Delta$ and $m_q - \mu_\Delta$.

What makes the twisted mass formulation interesting, especially for simulating light quark masses, is that the operator appearing in the fermion determinant is bounded from below. This can easily be seen, writing in flavor space

$$Q_\chi \;=\; D\mathbb{1} \,+\, i\mu\gamma_5\tau_3,$$

where for the moment we just consider the case with degenerate quark flavors ($\mu_\Delta = 0$). The fermion determinant in the full flavor space can be rewritten as a product of determinants in the single flavor space:

$$\begin{aligned} \det(Q_\chi) &= \det(D+i\mu\gamma_5)\,\det(D-i\mu\gamma_5) \\ &= \det(\gamma_5 D\gamma_5 + i\mu\gamma_5)\,\det(D-i\mu\gamma_5) \\ &= \det(D^\dagger D \,+\, \mu^2). \end{aligned} \tag{2.11}$$

$D^\dagger D$ is a Hermitian and positive operator, while μ^2 provides the lower bound. A similar proof can be given for non-zero μ_Δ, if the relation $\mu^2 > \mu_\Delta^2$ holds, cf. [31]. For completeness, we mention the Hermiticity property of the twisted mass fermion matrix:

$$Q^\dagger \;=\; \gamma_5\tau_1 Q \tau_1\gamma_5, \tag{2.12}$$

which, of course, holds independently of the basis considered[2].

2.2 $\mathcal{O}(a)$ improvement

The effect of lattice discretization effects can be represented by *Symanzik's continuum effective action*, cf. the discussion of the lattice formulation of χPT in Sec. 3.2. This

[1] Compared to this work, the rôles of τ_1 and τ_3 are interchanged there.

[2] In case of mass-degenerate quarks ($\mu_\Delta = 0$) the following is true as well:

$$Q^\dagger \;=\; \gamma_5\tau_a Q \tau_a\gamma_5, \quad a = 1,2.$$

approach is used to include such effects into the analysis rather than reducing them. Since the latter seems desirable, one can construct on the basis of *Symanzik's improvement program* improved lattice actions like the *Clover action*, where extra-terms are added to S_f, which are designed to remove cut-off effects up to some given order of the lattice spacing.

In this section we will demonstrate that at maximal twist ($\omega = \frac{\pi}{2}$) relevant observables, like hadron masses and some matrix elements, obtained with the QCD$^{\mathrm{TM}}$ action already are $\mathcal{O}(a)$ improved. This means that $\mathcal{O}(a)$ lattice artifacts are absent and the continuum limit is reached with corrections $\mathcal{O}(a^2)$. We remark that the definition of ω depends on how the critical quark mass is defined. An important assumption is that the critical mass is an odd function of the Wilson parameter r [26]. If one defines m_{crit} as the value of the mass parameter, where the pion mass vanishes, one may run into trouble as soon as there is no unique solution [32]. This may occur due to the phase structure of lattice QCD (cf. Sec. 3.3). The solution is to define ω in a proper way, which ensures automatic $\mathcal{O}(a)$ improvement. We provided such a definition [33] (cf. Sec. 2.4.1), as has been shown by [34, 35].

2.2.1 Improved correlators

Making the assumption that m_{crit} is an odd function of the Wilson parameter r

$$m_{\mathrm{crit}}(r) \;=\; -m_{\mathrm{crit}}(-r), \tag{2.13}$$

which always can be achieved by a suitable definition [26, 32, 35], one can show that either the Wilson average, or the mass average of the expectation values of a (multi-)local, multiplicatively renormalizable, and gauge invariant operator $\langle O \rangle$ defined as

$$\langle O \rangle^{\text{Wilson aver}}_{r,m_q,\omega} \;=\; \frac{\langle O \rangle_{r,m_q,\omega} + \langle O \rangle_{-r,m_q,\omega}}{2}, \tag{2.14}$$

$$\langle O \rangle^{\text{Mass aver}}_{r,m_q,\omega} \;=\; \frac{\langle O \rangle_{r,m_q,\omega} + (-1)^{P_{R_5}[O]} \langle O \rangle_{r,-m_q,\omega}}{2}, \tag{2.15}$$

respectively, is $\mathcal{O}(a)$ improved. $P_{R_5}[O]$ is the R_5 parity of an operator O

$$\mathcal{R}_5\, O \;=\; (-1)^{P_{R_5}[O]}\, O, \tag{2.16}$$

corresponding to the transformation

$$\mathcal{R}_5 : \left\{ \begin{array}{lcl} \psi(x) & \rightarrow & \gamma_5 \psi(x) \\ \bar{\psi}(x) & \rightarrow & -\bar{\psi}(x)\gamma_5 \end{array} \right. , \tag{2.17}$$

which obviously fulfills $\mathcal{R}_5^2 = \mathbb{1}$ and is an element of the chiral group $\mathrm{SU}(2) \otimes \mathrm{SU}(2)$. Here, improvement up to order a means, that the continuum limit is reached in the following way:

$$\langle O \rangle^{\text{improved}} \;=\; \langle O \rangle^{\text{cont}} \;+\; \mathcal{O}(a^2).$$

We will sketch the proof as presented in [26], valid for $\mu_\Delta = 0$. The extension to $\mu_\Delta \neq 0$ is possible. We will comment on this in Sec. 2.2.2. The Symanzik expansion of $\langle O \rangle$ schematically reads:

$$\langle O \rangle_{r,m_q,\omega} \;=\; \Big[\zeta_{r,\omega} \;+\; a m_q \xi_{r,\omega}\Big] \langle O \rangle^{\text{cont}}_{m_q} \;+\; a \sum_l (m_q)^{n_l} \eta^{O_l}_{r,\omega} \langle O_l \rangle^{\text{cont}}_{m_q} \;+\; \mathcal{O}(a^2), \tag{2.18}$$

with

$$n_l \;\equiv\; d[O] - d[O_l] + 1, \tag{2.19}$$

where $d[O]$ counts the dimension of the operator O. The sum over l has to cover all contributing operators $O_l \neq O$. Using the symmetry of the lattice action under the spurionic transformation

$$\mathcal{R}_5^{\rm sp} \;=\; \mathcal{R}_5 \times (r \to -r) \times (m_q \to -m_q) \tag{2.20}$$

one gets the following expression for the (lattice) correlators (at fixed ω)

$$\langle O \rangle_{r,m_q,\omega} \;=\; (-1)^{P_{R_5}[O]} \langle O \rangle_{-r,-m_q,\omega}. \tag{2.21}$$

Since the continuum correlators have a definite transformation behavior (in the continuum action the effect of $\mathcal{R}_5$ is $m_q \to -m_q$):

$$\langle O \rangle^{\rm cont}_{m_q} \;=\; (-1)^{P_{R_5}[O]} \langle O \rangle^{\rm cont}_{-m_q}, \tag{2.22}$$

too, one can prove that the averages Eqs. (2.14), (2.15) are $\mathcal{O}(a)$ improved by additionally using

$$P_{R_5}[O] \;+\; P_{R_5}[O_l] \;+\; n_l \;=\; 1 \bmod 2. \tag{2.23}$$

The latter follows from the definition of n_l and the additional symmetry enjoyed by the QCD$^{\rm TM}$ action $\mathcal{R}_5 \times \mathcal{D}_d$, where

$$\mathcal{D}_d \;\equiv\; \left\{ \begin{array}{lcl} U_\mu(x) & \to & U_\mu^\dagger(-x-\hat{\mu}) \\ \psi(x) & \to & e^{i\frac{3\pi}{2}} \psi(-x) \\ \bar{\psi}(x) & \to & \bar{\psi}(-x) e^{i\frac{3\pi}{2}} \end{array} \right. . \tag{2.24}$$

A special case arises for $\omega = \pm\frac{\pi}{2}$. If $\mathcal{P}$ is the normal parity transformation

$$\begin{array}{rcl} \mathcal{P} & \equiv & \left\{ \begin{array}{lcl} U_4(x) & \to & U_4(Px) \\ U_k(x) & \to & U_k^\dagger(Px-\hat{k}),\; k=1,2,3 \\ \psi(x) & \to & \gamma_4 \psi(Px) \\ \bar{\psi}(x) & \to & \bar{\psi}(Px)\gamma_4 \end{array} \right. , \\ Px = P(\boldsymbol{x},t) & \equiv & (-\boldsymbol{x},t) \end{array} \tag{2.25}$$

then also $\mathcal{P} \times (\omega \to -\omega)$ does not change the action and can be used to define an improved twist average in analogy to the preceding averages. Finally, we note that the change $\omega \to \omega + \pi$ has the same effect as $r \to -r$. Consequently every ω-even operator, i.e., every parity even operator, is automatically $\mathcal{O}(a)$ improved at maximal twist ($\omega = \frac{\pi}{2}$). This can easily be seen from the Wilson average, since for a parity even operator O

$$\langle O \rangle_{r,m_q,\omega=\frac{\pi}{2}} \;=\; \langle O \rangle_{r,m_q,\omega=-\frac{\pi}{2}} \;=\; \langle O \rangle_{-r,m_q,\omega=\frac{\pi}{2}}$$

holds. We will repeat the argument leading to automatic improvement without the assumption on $m_{\rm crit}$ in Sec. 2.2.2, and now continue showing that masses extracted from two-point correlators are such ω even quantities.

The two-point correlation function of a multiplicatively renormalizable operator O with definite parity p_O ($\mathcal{P}O = (-1)^{p_O} O$)

$$C_{OO}(\boldsymbol{x},t)_{\omega,r,m_q} \;=\; \langle O^\dagger(\boldsymbol{x},t) O(\boldsymbol{x},t) \rangle_{\omega,r,m_q} \tag{2.26}$$

leads to the spatial Fourier-transform

$$C_{OO}(\boldsymbol{k},t)_{\omega,r,m_q} \;=\; \sum_{\boldsymbol{x}} e^{i\boldsymbol{k}\boldsymbol{x}}\, C_{OO}(\boldsymbol{x},t)_{\omega,r,m_q}, \tag{2.27}$$

for which we write the spectral decomposition

$$C_{OO}(\boldsymbol{k},t)_{\omega,r,m_q} \;=\; \sum_{n} \frac{e^{-E_n(\boldsymbol{k})_{\omega,r,m_q}\cdot t}}{2E_n(\boldsymbol{k})_{\omega,r,m_q}}\, |\Omega_n(\boldsymbol{k})_{\omega,r,m_q}|^2. \tag{2.28}$$

Here, $\Omega_n(\boldsymbol{k})_{\omega,r,m_q}$ denotes the matrix element of O between the vacuum and the eigenstate with energy $E_n(\boldsymbol{k})_{\omega,r,m_q}$. Since $\mathcal{P}\times(\omega\to-\omega)$ is a symmetry, we have

$$C_{OO}(\boldsymbol{k},t)_{\omega,r,m_q} \;=\; C_{OO}(-\boldsymbol{k},t)_{-\omega,r,m_q}, \tag{2.29}$$

which implies

$$E_n(\boldsymbol{k})_{\omega,r,m_q} \;=\; E_n(-\boldsymbol{k})_{-\omega,r,m_q}, \tag{2.30}$$

and similar for the modulus of Ω. Since we are interested in the mass, with $M = E(\boldsymbol{k}=0)$ we showed, that this is indeed even under a change $(\omega\to-\omega)$:

$$M_{n;\,\omega,r,m_q} \;=\; E_n(0)_{\omega,r,m_q} \;=\; E_n(0)_{-\omega,r,m_q} \;=\; M_{n;\,-\omega,r,m_q}, \tag{2.31}$$

and therefore automatically $\mathcal{O}(a)$-improved at full twist.

2.2.2 Automatic improvement at full twist

We will now consider the physical basis, Eq. (2.8), at $\omega = \frac{\pi}{2}$:

$$-\exp[-i\omega\gamma_5\tau_3] \;=\; i\gamma_5\tau_3$$

and follow the argument given in [35]. The expansion of an expectation value of some multiplicative renormalizable, gauge invariant, and in general multi-local operator O reads

$$\langle O\rangle \;=\; \zeta\langle O\rangle^{\text{cont}} \;+\; \sum_{k=1}^{\infty} a^k \sum_{l^k} [\xi_{l^k} m_q^{n_{l^k}} \langle O_{l^k}\rangle^{\text{cont}}], \tag{2.32}$$

where the inner sum includes all contributing operators O_{l^k} and

$$n_{l^k} = d[O] - d[O_{l^k}] + k, \tag{2.33}$$

with $d[O]$ the dimension of the operator O. The maximal twisted QCD$^{\text{TM}}$ ($\mu_\Delta = 0$) action is invariant under $\mathcal{D}_d\times\mathcal{P}\times(m_q\to-m_q)$. We remark that at maximal twist $(m_q\to-m_q)$ is formal equivalent to

$$\mathcal{R}_5^b \;\equiv\; \left\{ \begin{array}{lcl} \psi(x) & \to & i\gamma_5\tau_b\psi(x) \\ \bar\psi(x) & \to & \bar\psi(x) i\gamma_5\tau_b \end{array} \right. \tag{2.34}$$

with $b = 1, 2$. In case of a mass non-degenerate doublet the former remains valid for $b = 1$ only, formally equivalent to $(m_q\to-m_q)\times(\mu_\Delta\to-\mu_\Delta)$. This implies for some parity even operator the vanishing of all terms proportional to some odd power of a: the reason is that parity is an exact symmetry of the continuum theory and $\mathcal{D}_d O(x) = (-1)^{d[O]} O(-x)$.

We showed without any assumption on m_{crit} the improvement property of a parity even operator at full twist, but did not define the twist angle yet. Since the above argument relied on the parity property of the continuum theory, it is natural to define ω in such a way that matrix elements given in the physical basis also respect this symmetry, see Sec. 2.4.1.

2.2.3 Possible caveat

At a first glance the above argument did not make any assumptions about the size of the quark mass (and the related pion mass) compared to the cut-off introduced by the lattice regularization. This is somewhat misleading. Of course, to reproduce the continuum in a proper way, the explicit breaking of chiral symmetry (cf. Chapter 3) should be driven by the mass term and not by the Wilson term in the lattice action. Naïvely one would expect a bound

$$\frac{m_q}{\Lambda_{\mathrm{QCD}}} \gg a\Lambda_{\mathrm{QCD}}.$$

Assuming $\Lambda_{\mathrm{QCD}} \approx 300$ MeV and present status $a \approx 0.1$ fm, one ends up with $m_q \gg 47$ MeV. An obvious attempt to weaken this restrictive condition is to use an already $\mathcal{O}(a)$ improved fermion action. The authors of [35] showed an alternative, which is to use the twist angle definition which will be given below. In this case the leading infrared divergent contributions (terms proportional to $(a/m_\pi^2)^{2k}$, $k = 1, 2, 3\ldots$) to some parity even and therefore automatically $\mathcal{O}(a)$ improved quantity are eliminated. With this result, the limit on the quark mass is reduced to

$$\frac{m_q}{\Lambda_{\mathrm{QCD}}} \gg (a\Lambda_{\mathrm{QCD}})^2$$

resulting in $m_q \gg 7$ MeV for the above example. The authors of [34, 32] also arrived at this conclusion considering lattice χPT and the phase structure of lattice QCD$^{\mathrm{TM}}$.

2.2.4 Critical mass

The critical mass (m_{crit}), or the related critical hopping parameter ($\kappa_{\mathrm{crit}} = 1/(2\mu_{\kappa\,\mathrm{crit}})$) has to be defined via the twist angle (m_{crit} is the point where the twist is maximal) to get consistent results. First attempts to show the automatic improvement in quenched twisted mass simulations [36, 37] looked promising, even with a definition of the critical mass by the vanishing of the pion mass in the untwisted theory. Going to lighter quark masses, this attempt failed, resulting in some "bending phenomenon" [28], which was cured by the proper definition of the critical mass [38, 39].

2.3 Currents, densities, and renormalization factors

The currents and densities, of course, should be defined in the physical basis. We list the vector, axial-vector currents and pseudo-scalar and scalar densities (physical basis denoted by a hat):

$$\hat{V}^a_{\mu x} = \bar{\psi}_x \gamma_\mu \frac{\tau_a}{2} \psi_x, \qquad \hat{A}^a_{\mu x} = \bar{\psi}_x \gamma_\mu \gamma_5 \frac{\tau_a}{2} \psi_x, \tag{2.35}$$

$$\hat{S}^0_x = \bar{\psi}_x \psi_x, \qquad \hat{P}^a_x = \bar{\psi}_x \gamma_5 \frac{\tau_a}{2} \psi_x, \tag{2.36}$$

their relation to the currents in the twisted basis is (replacing $\psi \to \chi$ gives V, A, S, P):

$$\hat{V}^a_{\mu x} = \begin{cases} \cos\omega\, V^a_{\mu x} + \sin\omega\, \epsilon_{ab3} A^b_{\mu x}, & a = 1,2 \\ V^3_{\mu x}, & a = 3 \end{cases} \tag{2.37}$$

$$\hat{A}^a_{\mu x} = \begin{cases} \cos\omega\, A^a_{\mu x} + \sin\omega\, \epsilon_{ab3} V^b_{\mu x}, & a = 1,2 \\ A^3_{\mu x}, & a = 3 \end{cases} \tag{2.38}$$

$$\hat{S}^0_x = \cos\omega\, S^0_x + 2i \sin\omega\, P^3_x \tag{2.39}$$

$$\hat{P}^a_x = \begin{cases} P^a_x, & a = 1,2 \\ \cos\omega\, P^3_x + \frac{i}{2}\sin\omega\, S^0_x, & a = 3 \end{cases} . \tag{2.40}$$

In [40] it has been shown that the twisted theory is renormalizable just like the untwisted one. This means that one has to renormalize the bare coupling g_0^2 and the subtracted bare mass $\tilde{m} = m_0 - m_{\rm crit}$:

$$g_R^2 = Z_g g_0^2, \quad m_R = Z_m \tilde{m} = Z_m (m_0 - m_{\rm crit}), \tag{2.41}$$

and, in addition, also renormalize the twisted mass multiplicatively

$$\mu_R = Z_\mu \mu. \tag{2.42}$$

2.3.1 Ward-Takahashi identities

From Eq. (2.8) we now want to derive the *Ward-Takahashi identities* (WTI) in the physical basis for a mass degenerate doublet. We are considering the change of an observable under the infinitesimal local chiral ($\mathrm{SU}(2) \otimes \mathrm{SU}(2)$) transformation

$$\psi(x) \to \psi'(x) = \Big(\mathbb{1} + \frac{i}{2}\alpha_{VSx}\tau_S + \frac{i}{2}\alpha_{ASx}\gamma_5\tau_S\Big)\psi(x) \tag{2.43}$$

$$\bar{\psi}(x) \to \bar{\psi}'(x) = \bar{\psi}(x)\Big(\mathbb{1} - \frac{i}{2}\alpha_{VSx}\tau_S + \frac{i}{2}\alpha_{ASx}\gamma_5\tau_S\Big), \tag{2.44}$$

where always a summation over $S = 1,2,3$ has to be performed, implying the vector and axial-vector WTI. The vector WTI is

$$\begin{aligned} &\left\langle O\left[\Big(\frac{S_{\rm phys}\overleftarrow{\partial}}{\partial\psi(x)}\frac{\tau_S}{2}\psi(x)\Big) - \Big(\bar{\psi}(x)\frac{\tau_S}{2}\frac{\overrightarrow{\partial}\, S_{\rm phys}}{\partial\bar{\psi}(x)}\Big)\right]\right\rangle = \\ &= \left\langle \Big(\frac{O\,\overleftarrow{\partial}}{\partial\psi(x)}\frac{\tau_S}{2}\psi(x)\Big) - \Big(\bar{\psi}(x)\frac{\tau_S}{2}\frac{\overrightarrow{\partial}\, O}{\partial\bar{\psi}(x)}\Big)\right\rangle. \end{aligned} \tag{2.45}$$

This results in

$$\begin{aligned} &\Bigg\langle O\Bigg[i\sin\omega\,(am_{\rm crit} + 4r)\bar{\psi}(x)\gamma_5\frac{\tau_S\tau_3 - \tau_3\tau_S}{2}\psi(x) \\ &-\frac{1}{4}\sum_{\mu=\pm1}^{\pm4}\Big(\bar{\psi}(x+\hat{\mu})U_\mu(x)\Big(\gamma_\mu + r\cos\omega - ir\sin\omega\,\gamma_5\tau_3\Big)\tau_S\psi(x) \\ &-\bar{\psi}(x)U_\mu(x-\hat{\mu})\tau_S\Big(\gamma_\mu + r\cos\omega - ir\sin\omega\,\gamma_5\tau_3\Big)\psi(x-\hat{\mu})\Big)\Bigg]\Bigg\rangle \\ = &\left\langle \Big(\frac{O\,\overleftarrow{\partial}}{\partial\psi(x)}\frac{\tau_S}{2}\psi(x)\Big) - \Big(\bar{\psi}(x)\frac{\tau_S}{2}\frac{\overrightarrow{\partial}\, O}{\partial\bar{\psi}(x)}\Big)\right\rangle. \end{aligned} \tag{2.46}$$

The axial-vector WTI is

$$\Big\langle O\Big[\Big(\frac{S_{\rm phys}\,\overleftarrow{\partial}}{\partial\psi(x)}\gamma_5\frac{\tau_S}{2}\psi(x)\Big)\;+\;\Big(\bar\psi(x)\gamma_5\frac{\tau_S}{2}\frac{\overrightarrow{\partial}\,S_{\rm phys}}{\partial\bar\psi(x)}\Big)\Big]\Big\rangle\;=$$
$$=\;\Big\langle\Big(\frac{O\,\overleftarrow{\partial}}{\partial\psi(x)}\gamma_5\frac{\tau_S}{2}\psi(x)\Big)\;+\;\Big(\bar\psi(x)\gamma_5\frac{\tau_S}{2}\frac{\overrightarrow{\partial}\,O}{\partial\bar\psi(x)}\Big)\Big\rangle, \tag{2.47}$$

which gives

$$\begin{aligned}&\Big\langle O\Big[\Big(m_q+\cos\omega\,(am_{\rm crit}+4r)\Big)\bar\psi(x)\gamma_5\tau_S\psi(x)\\
&-i\sin\omega\,(am_{\rm crit}+4r)\bar\psi(x)\frac{\tau_3\tau_S+\tau_S\tau_3}{2}\psi(x)\\
&-\frac{1}{4}\sum_{\mu=\pm1}^{\pm4}\Big(\bar\psi(x+\hat\mu)U_\mu(x)\Big(\gamma_\mu+r\cos\omega-ir\sin\omega\,\gamma_5\tau_3\Big)\gamma_5\tau_S\psi(x)\\
&+\bar\psi(x)U_\mu(x-\hat\mu)\gamma_5\tau_S\Big(\gamma_\mu+r\cos\omega-ir\sin\omega\,\gamma_5\tau_3\Big)\psi(x-\hat\mu)\Big)\Big]\Big\rangle\\
=\;&\Big\langle\Big(\frac{O\,\overleftarrow{\partial}}{\partial\psi(x)}\gamma_5\frac{\tau_S}{2}\psi(x)\Big)\;+\;\Big(\bar\psi(x)\gamma_5\frac{\tau_S}{2}\frac{\overrightarrow{\partial}\,O}{\partial\bar\psi(x)}\Big)\Big\rangle.\end{aligned} \tag{2.48}$$

These relations suggest to construct the point-split currents

$$\begin{aligned}\hat V^{T\text{p-s}}_{\mu x}\;&=\;\frac{1}{2}\Big[\bar\psi(x+\hat\mu)U_\mu(x)\Big(\gamma_\mu+r\cos\omega\Big)\frac{\tau_T}{2}\psi(x)\\
&\quad+\bar\psi(x)U^\dagger_\mu(x)\Big(\gamma_\mu-r\cos\omega\Big)\frac{\tau_T}{2}\psi(x+\hat\mu)\Big],\end{aligned} \tag{2.49}$$

$$\begin{aligned}\hat V^{3\text{p-s}}_{\mu x}\;&=\;\frac{1}{2}\Big[\bar\psi(x+\hat\mu)U_\mu(x)\Big(\gamma_\mu+r\cos\omega-ir\sin\omega\gamma_5\tau_3\Big)\frac{\tau_3}{2}\psi(x)\\
&\quad+\bar\psi(x)U^\dagger_\mu(x)\Big(\gamma_\mu-r\cos\omega+ir\sin\omega\gamma_5\tau_3\Big)\frac{\tau_3}{2}\psi(x+\hat\mu)\Big],\end{aligned} \tag{2.50}$$

$$\begin{aligned}\hat A^{T\text{p-s}}_{\mu x}\;&=\;\frac{1}{2}\Big[\bar\psi(x+\hat\mu)U_\mu(x)\Big(\gamma_\mu-ir\sin\omega\,\gamma_5\tau_3\Big)\gamma_5\frac{\tau_T}{2}\psi(x)\\
&\quad+\bar\psi(x)U^\dagger_\mu(x)\Big(\gamma_\mu+ir\sin\omega\gamma_5\tau_3\Big)\gamma_5\frac{\tau_T}{2}\psi(x+\hat\mu)\Big],\end{aligned} \tag{2.51}$$

$$\hat A^{3\text{p-s}}_{\mu x}\;=\;\frac{1}{2}\Big[\bar\psi(x+\hat\mu)U_\mu(x)\gamma_\mu\gamma_5\frac{\tau_3}{2}\psi(x)\;+\;\bar\psi(x)U^\dagger_\mu(x)\gamma_\mu\gamma_5\frac{\tau_3}{2}\psi(x+\hat\mu)\Big], \tag{2.52}$$

where $T = 1, 2$. They fulfill the WTI:

$$\begin{aligned}
&\left\langle O\partial^*_\mu \hat{V}^{T\text{p-s}}_{\mu x}\right\rangle + \left\langle \Big(\frac{O\overleftarrow{\partial}}{\partial\psi(x)}\frac{\tau_T}{2}\psi(x)\Big) - \Big(\bar\psi(x)\frac{\tau_T}{2}\frac{\overrightarrow{\partial}O}{\partial\bar\psi(x)}\Big)\right\rangle = \\
&= \epsilon_{3Tk}\sin\omega\left\langle O\Big[(am_{\text{crit}}+4r)\bar\psi(x)\tau_k\gamma_5\psi(x)\right. \\
&\quad \left. -\frac{r}{4}\sum_{\mu=\pm1}^{\pm4}\Big(\bar\psi(x+\hat\mu)U_\mu(x)\tau_k\gamma_5\psi(x) - \bar\psi(x)U_\mu(x-\hat\mu)\tau_k\gamma_5\psi(x-\hat\mu)\Big)\Big]\right\rangle, \qquad (2.53)
\end{aligned}$$

$$\left\langle O\partial^*_\mu \hat{V}^{3\text{p-s}}_{\mu x}\right\rangle + \left\langle \Big(\frac{O\overleftarrow{\partial}}{\partial\psi(x)}\frac{\tau_3}{2}\psi(x)\Big) - \Big(\bar\psi(x)\frac{\tau_3}{2}\frac{\overrightarrow{\partial}O}{\partial\bar\psi(x)}\Big)\right\rangle = 0, \qquad (2.54)$$

$$\begin{aligned}
&\left\langle O\partial^*_\mu \hat{A}^{T\text{p-s}}_{\mu x}\right\rangle + \left\langle \Big(\frac{O\overleftarrow{\partial}}{\partial\psi(x)}\gamma_5\frac{\tau_T}{2}\psi(x)\Big) + \Big(\bar\psi(x)\gamma_5\frac{\tau_T}{2}\frac{\overrightarrow{\partial}O}{\partial\bar\psi(x)}\Big)\right\rangle = \\
&= \left\langle O\Big[2\Big(m_q+\cos\omega\,(am_{\text{crit}}+4r)\Big)\underbrace{\bar\psi(x)\gamma_5\frac{\tau_T}{2}\psi(x)}_{=\hat P^T_x}\right. \\
&\quad \left. -\frac{r}{4}\cos\omega\sum_{\mu=\pm1}^{\pm4}\Big(\bar\psi(x+\hat\mu)U_\mu(x)\tau_T\gamma_5\psi(x) + \bar\psi(x)U_\mu(x-\hat\mu)\tau_T\gamma_5\psi(x-\hat\mu)\Big)\Big]\right\rangle, \qquad (2.55)
\end{aligned}$$

$$\begin{aligned}
&\left\langle O\partial^*_\mu \hat{A}^{3\text{p-s}}_{\mu x}\right\rangle + \left\langle \Big(\frac{O\overleftarrow{\partial}}{\partial\psi(x)}\gamma_5\frac{\tau_3}{2}\psi(x)\Big) + \Big(\bar\psi(x)\gamma_5\frac{\tau_3}{2}\frac{\overrightarrow{\partial}O}{\partial\bar\psi(x)}\Big)\right\rangle = \\
&= \left\langle O\Big[\bar\psi(x)\Big(m_q+(am_{\text{crit}}+4r)e^{-i\omega\gamma_5\tau_3}\Big)\gamma_5\tau_3\psi(x)\right. \\
&\quad \left. -\frac{r}{4}\sum_{\mu=\pm1}^{\pm4}\Big(\bar\psi(x+\hat\mu)U_\mu(x)e^{-i\omega\gamma_5\tau_3}\gamma_5\tau_3\psi(x) + \bar\psi(x)U_\mu(x-\hat\mu)e^{-i\omega\gamma_5\tau_3}\gamma_5\tau_3\psi(x-\hat\mu)\Big)\Big]\right\rangle. \qquad (2.56)
\end{aligned}$$

The third component of the vector current is always exactly conserved, therefore we write $\hat{V}^{3\text{cons}}_{\mu x} \equiv \hat{V}^{3\text{p-s}}_{\mu x}$. The situation for the rest is intermediate: at full twist, we obtain an exactly conserved axial-vector current $\hat{A}^{T\text{p-s}}_{\mu x}$. Without any twist ($\omega = 0$) we recover the situation, where $\hat{V}^{T\text{p-s}}_{\mu x}$ are exactly conserved, too. We also note that as a consequence of the exact axial-vector WTI (at full twist) one has $Z_P = Z_\mu^{-1}$, with Z_P being the renormalization constant for the pseudo-scalar density (remember that for $T = 1, 2$: $P^T = \hat{P}^T$). With the transformation rules Eqs. (2.37), (2.38), it becomes clear that the exactly conserved currents are the vector currents in the twisted basis $V^S_{\mu x}$. By inspecting the

WTI in the twisted basis directly, one gets for the vector WTI:

$$\begin{aligned}
&\Big\langle O\Big[i\mu\bar\chi(x)\frac{\tau_3\tau_S-\tau_S\tau_3}{2}\gamma_5\chi(x)\\
&-\frac{1}{4}\sum_{\mu=\pm1}^{\pm4}\Big(\bar\chi(x+\hat\mu)U_\mu(x)\tau_S\Big(\gamma_\mu+r\Big)\chi(x)\;-\;\bar\chi(x)U_\mu(x-\hat\mu)\tau_S\Big(\gamma_\mu+r\Big)\chi(x-\hat\mu)\Big)\Big]\Big\rangle\\
=\;&\Big\langle\Big(\frac{O\overleftarrow{\partial}}{\partial\chi(x)}\frac{\tau_S}{2}\chi(x)\Big)\;-\;\Big(\bar\chi(x)\frac{\tau_S}{2}\frac{\overrightarrow{\partial}O}{\partial\bar\chi(x)}\Big)\Big\rangle
\end{aligned}\tag{2.57}$$

and defines a conserved vector current:

$$V_{\mu x}^{S\text{cons}}\;=\;\frac{1}{2}\Big[\bar\chi(x+\hat\mu)U_\mu(x)\Big(\gamma_\mu+r\Big)\frac{\tau_S}{2}\chi(x)\;+\;\bar\chi(x)U_\mu^\dagger(x)\Big(\gamma_\mu-r\Big)\frac{\tau_S}{2}\chi(x+\hat\mu)\Big],\tag{2.58}$$

leading to

$$\begin{aligned}
\Big\langle O\partial_\mu^* V_{\mu x}^{S\text{cons}}\Big\rangle+\Big\langle\Big(\frac{O\overleftarrow{\partial}}{\partial\chi(x)}\frac{\tau_S}{2}\chi(x)\Big)\;-\;\Big(\bar\chi(x)\frac{\tau_S}{2}\frac{\overrightarrow{\partial}O}{\partial\bar\chi(x)}\Big)\Big\rangle\;&=\\
=\;\mu\Big\langle O\Big[\underbrace{\bar\chi(x)\,i\gamma_5\frac{\tau_3\tau_S-\tau_S\tau_3}{2}\chi(x)}\Big]\Big\rangle.&\\
=\begin{cases}2\epsilon_{S3k}P_k, & S=1,2\\ 0, & S=3\end{cases}&
\end{aligned}\tag{2.59}$$

This is referred to as the PCVC (partially conserved vector current)-relation in the twisted basis, in contrast to the PCAC (partially conserved axial-vector current)-relation in untwisted QCD. For completeness, the axial-vector WTI in the twisted basis reads

$$\begin{aligned}
&\Big\langle O\Big[\bar\chi(x)\Big(\mu_\kappa\gamma_5\tau_S+i\mu\frac{\tau_3\tau_S+\tau_S\tau_3}{2}\Big)\chi(x)\\
&-\frac{1}{4}\sum_{\mu=\pm1}^{\pm4}\Big(\bar\chi(x+\hat\mu)U_\mu(x)\Big(\gamma_\mu+r\Big)\gamma_5\tau_S\chi(x)\;+\;\bar\chi(x)U_\mu(x-\hat\mu)\gamma_5\tau_S\Big(\gamma_\mu+r\Big)\chi(x-\hat\mu)\Big)\Big]\Big\rangle\\
=\;&\Big\langle\Big(\frac{O\overleftarrow{\partial}}{\partial\chi(x)}\gamma_5\frac{\tau_S}{2}\chi(x)\Big)\;+\;\Big(\bar\chi(x)\gamma_5\frac{\tau_S}{2}\frac{\overrightarrow{\partial}O}{\partial\bar\chi(x)}\Big)\Big\rangle,
\end{aligned}\tag{2.60}$$

leading to the definition of a point-split current

$$A_{\mu x}^{\text{Sp-s}}\;=\;\frac{1}{2}\Big[\bar\chi(x+\hat\mu)U_\mu(x)\gamma_\mu\gamma_5\frac{\tau_S}{2}\chi(x)\;+\;\bar\chi(x)U_\mu^\dagger(x)\gamma_\mu\gamma_5\frac{\tau_S}{2}\chi(x+\hat\mu)\Big].\tag{2.61}$$

The axial-vector WTI then becomes

$$\left\langle O\partial^*_\mu A^{\text{Sp-s}}_{\mu x}\right\rangle + \left\langle \Big(\frac{O\ \overleftarrow{\partial}}{\partial\chi(x)}\gamma_5\frac{\tau_S}{2}\chi(x)\Big) \;+\; \Big(\bar\chi(x)\gamma_5\frac{\tau_S}{2}\frac{\overrightarrow{\partial}\ O}{\partial\bar\chi(x)}\Big)\right\rangle \;=$$

$$= \left\langle O\Big[2\mu_\kappa \underbrace{\bar\chi(x)\gamma_5\frac{\tau_S}{2}\chi(x)}_{=P^S_x} + i\mu \underbrace{\bar\chi(x)\frac{\tau_3\tau_S+\tau_S\tau_3}{2}\chi(x)}_{=\begin{cases}0, & S=1,2\\ S^0_x, & S=3\end{cases}}\right.$$

$$\left. -\frac{r}{4}\sum_{\mu=\pm1}^{\pm4}\Big(\bar\chi(x+\hat\mu)U_\mu(x)\gamma_5\tau_S\chi(x)+\bar\chi(x)U_\mu(x-\hat\mu)\gamma_5\tau_S\chi(x-\hat\mu)\Big)\Big]\right\rangle. \tag{2.62}$$

2.3.2 Renormalized currents

Because the vector current is always ($S = 1, 2, 3$) exactly conserved in the twisted basis we adopt the following renormalization strategy [31]: the currents get renormalized in the twisted basis, with constants Z_V, Z_A, ..., ensuring that one has $Z_V = 1$ if the conserved vector current is used. The renormalized charged ($T = 1, 2$) currents in the physical basis (denoted with a check) now become

$$\check V^T_{\mu x} \;=\; Z_V\cos\omega\, V^T_{\mu x} \;+\; Z_A\sin\omega\,\epsilon_{Ta3}A^a_{\mu x}, \tag{2.63}$$

$$\check A^T_{\mu x} \;=\; Z_A\cos\omega\, A^T_{\mu x} \;+\; Z_V\sin\omega\,\epsilon_{Ta3}V^a_{\mu x}, \tag{2.64}$$

while for $a = 3$ (neutral currents) one simply has:

$$\check V^3_{\mu x} \;=\; Z_V\, V^3_{\mu x} \;=\; Z_V\,\hat V^3_{\mu x}, \tag{2.65}$$

$$\check A^3_{\mu x} \;=\; Z_A\, A^3_{\mu x} \;=\; Z_A\,\hat A^3_{\mu x}. \tag{2.66}$$

For $T = 1, 2$ the pseudo-scalar densities are identical in both bases, giving

$$\check P^T_x \;=\; Z_P P^T_x \;=\; Z_P\hat P^T_x. \tag{2.67}$$

The situation for $\hat P^3_x$ is more involved, since it mixes with the scalar density in the twisted basis. We will not use the latter; details on its renormalization can be found in [31]. For the WTI we have:

$$\langle\partial^*_\mu\check V^S_{\mu x}\,\hat O_y\rangle \;=\; \mathcal{O}(a), \tag{2.68}$$

$$\langle\partial^*_\mu\check A^T_{\mu x}\,\hat O_y\rangle \;=\; 2m_R\,\langle\check P^T_x\,\hat O_y\rangle \;+\; \mathcal{O}(a). \tag{2.69}$$

We will use the expressions for the charged currents in Sec. 2.4.1 to determine the twist angle.

2.4 Measurement of relevant quantities

In the remainder of this chapter we will consider degenerate doublets ($\mu_\Delta = 0$) and use $\tau_\pm, \tau_3$ as the basis in flavor space for practical purposes, which will become clear later

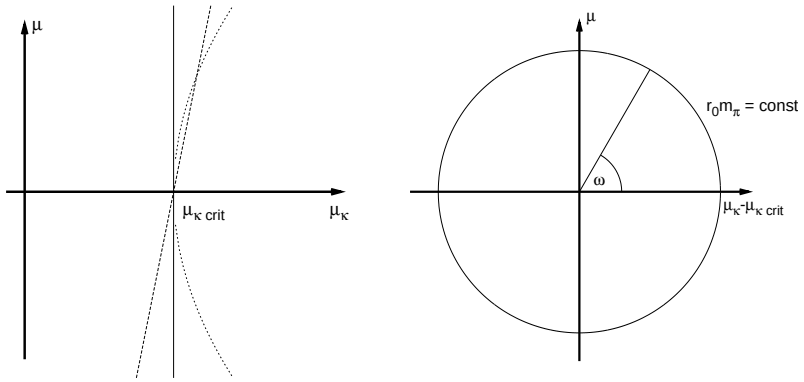

Figure 2.1: Left panel: *Possible lines of maximal twist in the μ_κ-μ plane, which intersect the μ_κ-axis at the value for the critical mass.* Right panel: *Circle of constant pion mass (equivalent to constant quark mass) in the continuum limit, when the line of maximal twist is a straight line perpendicular to the μ_κ axis (solid line in left panel).*

when we discuss how to apply QCD$^{\rm TM}$ in our measurement code (App. C.1). In this basis the renormalized charged physical currents read

$$\check{V}^{\pm}_{\mu x} = Z_V \cos\omega\, V^{\pm}_{\mu x} \mp i Z_A \sin\omega\, A^{\pm}_{\mu x}, \tag{2.70}$$

$$\check{A}^{\pm}_{\mu x} = Z_A \cos\omega\, A^{\pm}_{\mu x} \mp i Z_V \sin\omega\, V^{\pm}_{\mu x}. \tag{2.71}$$

Before starting we want to make some general considerations concerning the extraction of physical quantities from simulations. First we note that in a numerical simulation only the twisted basis can be used, since the critical mass and related the twist angle are a priori unknown and have to be measured afterwards. The input parameter to a numerical simulation are μ_κ and μ, μ_Δ and not $m_q \pm \mu_\Delta$ and ω. For the same reason, it is practically not possible to run a simulation exactly at full twist. One may perform a series of simulations and tuning the input parameters to reach this point, but the simple assumption that the critical mass does not depend on the twisted mass parameter is in practice only a first approximation. In general the critical line in the μ_κ-μ plane can be anything reasonable (Fig. 2.1, left panel). To us the best strategy seemed to be running simulations at different values of μ_κ with fixed μ and determining the quantities as functions of the measured twist angle. Afterwards an interpolation to full twist can be performed to get an improved estimate. Taking into account the fact that in the continuum limit physical quantities become independent of ω at a fixed value of the quark mass (i.e., when moving around the circle shown in Fig. 2.1, right panel), these results can be directly compared to untwisted ($\mu = 0$) ones at the same mass.

How to obtain relevant quantities like the twist angle, renormalization factors, the pion decay constant, and the quark mass in the presence of a twisted mass term will be discussed now. Since the charged pseudo-scalar currents are the same in both bases, the pion mass can be obtained from the C_{PP} correlator like in the untwisted case (cf. Sec. 1.2.2). The situation is different for the rho mass, which now has to be extracted from $C_{A_iA_i}$ at full twist; we also used this definition for $\omega \neq \frac{\pi}{2}$. In general, either the $C_{A_iA_i}$ or $C_{V_iV_i}$ correlator are to be considered and the one giving the better signal should be chosen.

2.4.1 Twist angle

As mentioned before, the twist angle ω (together with the renormalization constants) is defined by imposing the WTIs to hold for the physical currents. We introduce the auxiliary angles

$$\omega_V = \arctan\left(\frac{Z_A}{Z_V}\tan\omega\right), \tag{2.72}$$

$$\omega_A = \arctan\left(\frac{Z_V}{Z_A}\tan\omega\right), \tag{2.73}$$

with which Eqs. (2.63), (2.64) can be rewritten as

$$\check{V}^T_{\mu x} = \mathcal{N}_V(\cos\omega_V\, V^T_{\mu x} + \sin\omega_V\, \epsilon_{Ta3} A^a_{\mu x}), \tag{2.74}$$

$$\check{A}^T_{\mu x} = \mathcal{N}_A(\cos\omega_A\, A^T_{\mu x} + \sin\omega_A\, \epsilon_{Ta3} V^a_{\mu x}), \tag{2.75}$$

$$\mathcal{N}_X \equiv \frac{Z_X}{\cos\omega_X\,\sqrt{1+\tan\omega_V\,\tan\omega_A}},\quad X = V, A. \tag{2.76}$$

The twist angle ω is now given in terms of the two auxiliary ones as

$$\omega = \arctan\left(\sqrt{\tan\omega_V\,\tan\omega_A}\right). \tag{2.77}$$

In case of full twist ($\omega = \frac{\pi}{2}$) all these three angles coincide, otherwise they differ by lattice artifacts. In the continuum limit $\frac{Z_V}{Z_A}$ tends towards 1 and they agree in general. In the following we will discuss different ansätze, how to measure these angles from correlators.

- **vector WTI**
  From Eq. (2.68) (neglecting $\mathcal{O}(a)$ and now using $\tau^{\pm}$) one gets

  $$\tan\omega_V(x_4 - y_4) = -i\frac{\sum_{\boldsymbol{x},\boldsymbol{y}}\left\langle \partial^*_4 V^+_{4x}\hat{O}^-_y\right\rangle}{\sum_{\boldsymbol{x},\boldsymbol{y}}\left\langle \partial^*_4 A^+_{4x}\hat{O}^-_y\right\rangle}, \tag{2.78}$$

  where for O^-_y one might use P^-_y.

  Here the notation indicates that the result depends on the timeslice distance $(x_4 - y_4)$. In practice one assumes that this distance can be chosen large enough, when this dependence is negligible.

- **parity conservation**
  By observing that $\mathcal{P}\times(\mu\to-\mu)$ is a symmetry of the action, in the physical basis the following correlators should vanish:

  $$\sum_{\boldsymbol{x},\boldsymbol{y}}\sum_{i=1}^{3}\langle\check{A}^+_{ix}\check{V}^-_{iy}\rangle = 0,\quad \sum_{\boldsymbol{x},\boldsymbol{y}}\langle\check{V}^+_{4x}\check{P}^-_y\rangle = 0 \tag{2.79}$$

  resulting in solutions for ω_V and ω_A. In the first case, the spatial components have to be used [41], because for $\check{V}^-_{\mu x}$ one can only give an estimate, e.g., based on the result for ω_V from the second equation. This estimate also contains spurious axial components. If taking the time component, the lightest and therefore dominating

state in the correlator would be the pion and not the heavier state associated with the time component of the physical vector current. This leads to the wrong condition $\langle 0|\check{A}_{4x}|\pi\rangle = 0$. Instead with the spatial components the dominating state is the rho, leading to the right condition $\langle 0|\check{A}_{ix}|\rho\rangle = 0$.

The angles are then obtained by the following formulae, where for ω_A the first result is needed:

$$\tan\omega_V(x_4-y_4) = -i\,\frac{\sum_{\boldsymbol{x},\boldsymbol{y}}\langle V^+_{4x}P^-_y\rangle}{\sum_{\boldsymbol{x},\boldsymbol{y}}\langle A^+_{4x}P^-_y\rangle}, \tag{2.80}$$

$$\tan\omega_A(x_4-y_4) = \frac{i\sum_{\boldsymbol{x},\boldsymbol{y},i}\langle A^+_{ix}V^-_{iy}\rangle + \tan\omega_V\,\sum_{\boldsymbol{x},\boldsymbol{y},i}\langle A^+_{ix}A^-_{iy}\rangle}{\sum_{\boldsymbol{x},\boldsymbol{y},i}\langle V^+_{ix}V^-_{iy}\rangle - i\tan\omega_V\,\sum_{\boldsymbol{x},\boldsymbol{y},i}\langle V^+_{ix}A^-_{iy}\rangle}. \tag{2.81}$$

The same symmetry considerations also hold, if the derivatives of the currents were used instead. In case of ω_V this would then yield the same result as derived from the vector WTI (Eq. (2.78) with $O = P$).

Both these definitions of the twist angle are local ones and do not involve any extrapolation (to the chiral limit of vanishing pion or quark mass), which would give rise to another ambiguity. This definition is suitable in case of PQχPT$^{\mathrm{TM}}$(cf. Sec. 4.2), too. There one needs to know the twist angle for the valence quarks independently from the sea quarks.

2.4.2 Renormalization factors

Once the twist angles have been determined, these also allow us to estimate the ratio of renormalization factors $\frac{Z_A}{Z_V}$. From Eqs. (2.72), (2.73) we have:

$$\frac{Z_A}{Z_V} = \sqrt{\frac{\tan\omega_V}{\tan\omega_A}}. \tag{2.82}$$

Z_V can be determined separately by considering ratios of correlators including the vector current to those where it has been replaced by the conserved current, e.g.,

$$Z_V = \frac{\langle V^+_{4x}\quad P^-_y\rangle}{\langle V^{+\mathrm{cons}}_{4x}P^-_y\rangle}. \tag{2.83}$$

In Sec. 5.3.3 we will also show in which way the ratio Z_m/Z_μ can be obtained in a special set-up of performed simulations.

2.4.3 Pion decay constant

The pion decay constant, defined in analogy to the untwisted case, Eq. (1.38), is like the pion mass a basic quantity. Taking the recipe from the untwisted case, Eq. (1.42), one could either use the correlator $\langle A^+_4P^-\rangle$ or $\langle V^+_4P^-\rangle$ in the twisted basis, since both contain the relevant physical axial-vector current. We are interested in an interpolation to full twist, where $\mathcal{O}(a)$ improvement is guaranteed. From

$$V^+_{4x} = \frac{1}{Z_V}\Big(\cos\omega\,\check{V}^+_{4x} + i\sin\omega\,\check{A}^+_{4x}\Big),$$
$$A^+_{4x} = \frac{1}{Z_A}\Big(\cos\omega\,\check{A}^+_{4x} + i\sin\omega\,\check{V}^+_{4x}\Big)$$

it can be seen that in the first case the unwanted contribution is multiplied by $\cos\omega$, while in the latter by $\sin\omega$. Therefore, the first should give the better signal, if one is already close to $\omega = \frac{\pi}{2}$. In this way one extracts $af_{\chi\pi}/Z_V$: We define the amplitude ratio

$$r_{V_4P} \;=\; \frac{-i\langle 0|V_{4\,0}^{+}|\pi\rangle}{\langle 0|P_0^{+}|\pi\rangle}, \tag{2.84}$$

which can be extracted from the ratio of the correlators C_{V_4P} and C_{PP} according to Eq. (1.40). Further the pion mass from the C_{PP} correlator (m_{PP}), and the amplitude g_π^l is needed, Eq. (1.41). The pion decay constant then is obtained according to

$$\frac{af_{\chi\pi}}{Z_V} \;=\; \frac{r_{V_4P}\, g_\pi^l}{m_{PP}}. \tag{2.85}$$

By using the conserved vector current, $Z_V = 1$ is achieved. Clearly $f_{\chi\pi}$ is not the physical decay constant, which only can be extracted from the physical current, or by interpolating results taken at different twist angles with V^+ to $\omega = \frac{\pi}{2}$. It should be noted, that $f_{\chi\pi}$ extracted from A^+ undergoes a sign change at $\omega = \frac{\pi}{2}$ by definition.

At maximal twist it is possible to extract f_π only from the fit to the C_{PP} correlator, as has been presented in [36]. We now repeat the argument given there: since by using the exactly conserved vector current the PCVC-relation in the twisted basis is an exact identity, and the relation between the multiplicative renormalization constants for the pseudo-scalar density and the quark mass entering that relation, $Z_P = Z_\mu^{-1}$ holds. One has

$$f_\pi m_\pi^2 \;=\; \partial_\mu \,\langle 0|V_{\mu\,0}^{2}|\pi\rangle \;=\; 2\mu\,\langle 0|P_0^{1}|\pi\rangle, \tag{2.86}$$

where μ is the twisted mass entering the action, Eq. (2.1). Both quantities, m_π and $\langle 0|P^1|\pi\rangle$, can be extracted from the C_{PP} correlator in a single fit (cf. Eq. (1.34)).

2.4.4 Quark mass

A working definition of the quark mass in the twisted basis is to define it through the PCAC-relation in the twisted basis up to a renormalization factor $Z_q = Z_P/Z_A$:

$$Z_q a m_\chi^{\mathrm{PCAC}}(x_4 - y_4) \;=\; \frac{\sum_{\boldsymbol{x},\boldsymbol{y}}\langle \partial_4^* A_{4x}^{+} P_y^{-}\rangle}{2\sum_{\boldsymbol{x},\boldsymbol{y}}\langle P_x^{+} P_y^{-}\rangle}. \tag{2.87}$$

One has to compute the derivative of the correlators or use Eq. (1.47) like in the untwisted case. At maximal twist the axial-vector current in the twisted basis becomes the physical vector current, which leads to $am_\chi^{\mathrm{PCAC}} \to \mathcal{O}(a)$ for $\omega \to \frac{\pi}{2}$ even for a non-zero twisted mass term and therefore also allows a determination of the critical hopping parameter. Actually this definition measures just the untwisted part, and therefore has different signs, depending on the twist angle or, equivalently, if $\tilde{m}$ is positive or negative. Including also

the twisted vector current, a "true" quark mass definition would be

$$\begin{aligned} am_q^{\mathrm{PCAC}}(x_4 - y_4) &\equiv \frac{\sum_{\boldsymbol{x},\boldsymbol{y}} \langle \partial_4^* \check{A}_{4x}^+ \check{P}_y^- \rangle}{2 \sum_{\boldsymbol{x},\boldsymbol{y}} \langle \check{P}_x^+ \check{P}_y^- \rangle} \\ &= \frac{Z_A \cos\omega \sum_{\boldsymbol{x},\boldsymbol{y}} \langle \partial_4^* A_{4x}^+ P_y^- \rangle - i Z_V \sin\omega \sum_{\boldsymbol{x},\boldsymbol{y}} \langle \partial_4^* V_{4x}^+ P_y^- \rangle}{2 Z_P \sum_{\boldsymbol{x},\boldsymbol{y}} \langle P_x^+ P_y^- \rangle} \\ &= \frac{\mathcal{N}_A}{2 Z_P} \frac{\cos\omega_A \sum_{\boldsymbol{x},\boldsymbol{y}} \langle \partial_4^* A_{4x}^+ P_y^- \rangle - i \sin\omega_A \sum_{\boldsymbol{x},\boldsymbol{y}} \langle \partial_4^* V_{4x}^+ P_y^- \rangle}{\sum_{\boldsymbol{x},\boldsymbol{y}} \langle P_x^+ P_y^- \rangle}, \end{aligned} \tag{2.88}$$

which for a non-zero twisted mass term should not vanish at maximal twist, but is completely given by the vector current in the twisted basis.

Using Eq. (1.46) for a quark mass definition based on the pion mass extracted from C_{PP} also gives a "true" definition, because the pion mass does not vanish at the critical mass, but is given there exclusively by the non-zero twisted component, too.

Chapter 3

QCD near zero quark mass

The low energy region of QCD is dominated by the effects originating from the three lightest quarks: up, down and strange. In 1968, Weinberg proposed an effective Lagrangian approach to deal with the low energy dynamics of the strong interactions [42] based on the non-linear realization of spontaneously broken symmetry in the light pseudo-Goldstone boson sector. Gasser and Leutwyler [43, 44] defined this effective Lagrangian as an expansion in the quark masses and momenta: Chiral Perturbation Theory (χPT), using a set of *Low Energy Constants (LECs)*, also referred to as *Gasser-Leutwyler constants*. In the first section of this chapter, we will present the basics for χPT in the continuum. The lattice formulation of QCD has to deal with the problem that simulations at realistic dynamical quark masses are computationally very demanding and with todays computer resources are still out of reach. The simulated points by the qq+q Collaboration (cf. Sec. 5.2) reached a lightest pion mass of $\approx$ 370 MeV and lightest quark mass of $\approx {}^1\!/_4\, m_{\text{strange}}$. Compared to the real world [45] $m_\pi = 139.57018(35)$ MeV and $m_{\text{down}}/m_{\text{strange}} \approx {}^1\!/_{17} \sim {}^1\!/_{22}$, $m_{\text{up}}/m_{\text{down}} \approx {}^3\!/_{10} \sim {}^7\!/_{10}$ it becomes clear, that an extrapolation of lattice results to lower quark masses is needed. For that reason we will discuss the lattice version of χPT, too, which furthermore allows for a treatment of effects of the lattice discretization and finite box size. This is the fundament for the partially quenched χPT we used for our numerical analysis (Sec. 5.2) and which will be introduced in the following chapter. On the one hand, chiral effective theories provide us with the extrapolations needed for lattice results. On the other hand, the lattice opens the opportunity to determine the universal constants appearing in such theories from a first principle approach. The latter would be impossible by perturbative methods in QCD, since the strongly interacting low energy sector is non-perturbative. In the remainder of this chapter we will use the lattice version of χPT to discuss the phase structure of lattice QCD near zero quark mass.

3.1 Continuum χPT

Decomposing the fermion fields into their right- and left-handed parts

$$\psi_{L,R} \;\equiv\; \frac{1 \mp \gamma_5}{2}\,\psi, \quad \bar{\psi}_{L,R} \;\equiv\; \bar{\psi}\,\frac{1 \pm \gamma_5}{2} \tag{3.1}$$

the QCD-Lagrangian (1.1) becomes

$$\mathcal{L}_{\text{QCD}} \;=\; \frac{1}{4} F^a_{\mu\nu}(x) F^{a\,\mu\nu}(x) + \bar{\psi}_L(x) \not{D} \psi_L(x) + \bar{\psi}_R(x) \not{D} \psi_R(x) + m(\bar{\psi}_L \psi_R + \bar{\psi}_R \psi_L). \tag{3.2}$$

In the massless case ($m = 0$) this Lagrangian is invariant under a global $\mathrm{SU}(N_f)_L \otimes \mathrm{SU}(N_f)_R$ transformation of the right- and left-handed fermion fields in flavor space:

$$\psi_L \to \exp(-i\boldsymbol{\theta_L} \cdot \boldsymbol{\lambda})\,\psi_L, \quad \psi_R \to \exp(-i\boldsymbol{\theta_R} \cdot \boldsymbol{\lambda})\,\psi_R. \tag{3.3}$$

It is also possible to split these transformations into a vector and axial-vector part:

$$\psi \to \exp(-i\boldsymbol{\theta_V} \cdot \boldsymbol{\lambda})\,\psi, \quad \psi \to \exp(-i\boldsymbol{\theta_A} \cdot \boldsymbol{\lambda}\gamma_5)\,\psi, \tag{3.4}$$

with $\boldsymbol{\theta_V} = \frac{\boldsymbol{\theta_L}+\boldsymbol{\theta_R}}{2}$ and $\boldsymbol{\theta_A} = \frac{\boldsymbol{\theta_L}-\boldsymbol{\theta_R}}{2}$. The $\boldsymbol{\lambda}$ are the generators of the symmetry group, i.e., the Pauli matrices for SU(2) or the Gell-Mann matrices for SU(3). In case of non-zero mass-degenerate fermions, only the $\mathrm{SU}(N_f)_V$ vector transformations leave the Lagrangian invariant. Here, we did not take the $\mathrm{U}(1)_A$ and $\mathrm{U}(1)_V$ symmetries into account: the first is not anomaly-free (referred to as Adler-Bell-Jackiw-anomaly [46, 47]), while the latter just imposes conservation of the numbers of quarks.

Since the up-, down- and strange-quark masses are small, one would expect the chiral symmetry $\mathrm{SU}(3)_\chi \equiv \mathrm{SU}(3)_V \otimes \mathrm{SU}(3)_A$ to be at least approximately realized in nature. Because this is not the case, but the hadronic spectrum can be classified in $\mathrm{SU}(3)_V$ representations, one is driven to the assumption, that the full $\mathrm{SU}(3)_\chi$ is spontaneously broken down to $\mathrm{SU}(3)_V$. By *Goldstone's theorem* one expects an octet of pseudo-scalar massless bosons to appear. The lightest octet of pseudo-scalar mesons (i.e., bosonic hadrons), which are much lighter than the other hadronic states, can be identified as the "would-be Goldstone bosons". Their masses are due to the fact that the full chiral symmetry is only approximate and it is explicitly broken by the non-vanishing quark masses.

A very convenient way to formulate a low energy theory, whose interactions are constrained by the underlying Goldstone nature, is to use an *effective theory* in the parametrization

$$\Sigma(\Phi) \;\equiv\; \exp\left(\frac{2i\Phi}{f_0}\right) \tag{3.5}$$

of the Goldstone fields

$$\Phi(x) \;\equiv\; \frac{1}{2}\boldsymbol{\lambda}\boldsymbol{\phi} \;=\; \frac{1}{\sqrt{2}}\begin{pmatrix} \frac{1}{\sqrt{2}}\pi^0 + \frac{1}{\sqrt{6}}\eta_8 & \pi^+ & K^+ \\ \pi^- & -\frac{1}{\sqrt{2}}\pi^0 + \frac{1}{\sqrt{6}}\eta_8 & K^0 \\ K^- & \bar{K}^0 & -\frac{2}{\sqrt{6}}\eta_8 \end{pmatrix}. \tag{3.6}$$

Here we already introduced the symbol f_0, which will be the pion decay constant in lowest order. Under a chiral rotation Σ transforms as

$$\Sigma \;\to\; L\,\Sigma\,R^\dagger, \quad L, R \in \mathrm{SU}(3). \tag{3.7}$$

The vacuum state $\Sigma_0 = \mathbb{1}$, corresponding to $\phi = 0$, is only invariant under a vector transformation ($L = R$), leading to the spontaneous chiral symmetry breaking.

Up to some energy scale Λ_χ, the fields $\Phi(x)$ are considered as the only hadronic degrees of freedom. (This scale should be below the mass of the rho-meson, $m_\rho \approx 770$ MeV.) The effective Lagrangian is now organized as an expansion in powers of the momenta and quark masses with respect to this scale: $(p^2/\Lambda_\chi^2)^n$, $(m_q/\Lambda_\chi)^n$:

$$\mathcal{L} \;=\; \sum_n \mathcal{L}_{2n}. \tag{3.8}$$

One has to construct all possible terms to a given order, which respect the underlying symmetries (i.e., chiral-, and Lorentz-symmetry). Further, the breaking of the symmetry has to be realized by the same pattern as in the original QCD-Lagrangian. This is achieved by rewriting the Lagrangian, Eq. (1.1) or (3.2), in terms of sources l_μ, r_μ, s, p:

$$\begin{aligned}\mathcal{L} &= \mathcal{L}_{m=0} + i\bar{\psi}\gamma_\mu\frac{1+\gamma_5}{2}r_\mu\psi + i\bar{\psi}\gamma_\mu\frac{1-\gamma_5}{2}l_\mu\psi \\ &\quad +\bar{\psi}_L(s+ip)\psi_R + \bar{\psi}_R(s-ip)\psi_L. \end{aligned} \tag{3.9}$$

Observe that this Lagrangian is invariant under the *local* SU(3) transformations $L(x), R(x)$:

$$\psi_L \to L(x)\psi_L, \quad \psi_R \to R(x)\psi_R,$$

if the external fields are treated as gauge fields:

$$l_\mu \to L(x)l_\mu L^\dagger(x) + i\big(\partial_\mu L(x)\big)L(x)^\dagger \tag{3.10}$$

$$r_\mu \to R(x)r_\mu R^\dagger(x) + i\big(\partial_\mu R(x)\big)R(x)^\dagger \tag{3.11}$$

$$(s+ip) \to L(x)(s+ip)R^\dagger(x). \tag{3.12}$$

Further, in the effective Lagrangian the covariant derivative

$$D_\mu\Sigma = \partial_\mu\Sigma + il_\mu\Sigma - i\Sigma r_\mu \tag{3.13}$$

is introduced, which transforms like $D_\mu\Sigma \to L(D_\mu\Sigma)R^\dagger$. The field strength tensors have to be defined as

$$L_{\mu\nu} = \partial_\mu l_\nu - \partial_\nu l_\mu + i[l_\mu, l_\nu], \tag{3.14}$$

$$R_{\mu\nu} = \partial_\mu r_\nu - \partial_\nu r_\mu + i[r_\mu, r_\nu], \tag{3.15}$$

which results in $L_{\mu\nu} \to LL_{\mu\nu}L^\dagger$ and $R_{\mu\nu} \to RR_{\mu\nu}R^\dagger$. This transformation pattern of the external fields is often referred to as a *spurionic symmetry*.

In this way from $\Sigma, D_\mu\Sigma, L_{\mu\nu}, R_{\mu\nu}$, and $(s+ip)$ one can construct the effective Lagrangian, which has the required symmetry properties. The bare QCD-Lagrangian is obtained in the limit $l_\mu = r_\mu = p = 0$ and $s = m$. The external fields l_μ, r_μ can be used to also include electro-magnetic and weak interactions. Since we want to restrict ourselves to the study of pure QCD effects, all external fields except the mass generating scalar field s will be set to zero. By this choice the covariant derivative reduces to the normal one: $D_\mu \to \partial_\mu$. To lowest order in the effective Lagrangian one gets

$$\mathcal{L}_2 = \frac{f_0^2}{4}\mathrm{Tr}[\partial_\mu\Sigma\partial^\mu\Sigma^\dagger] - \frac{f_0^2}{4}\mathrm{Tr}[\chi\Sigma^\dagger + \Sigma\chi^\dagger], \tag{3.16}$$

where

$$\chi \equiv 2B_0\,(s+ip) \tag{3.17}$$

is the external field related to the quark masses. B_0 is a positive constant with the dimension of a mass, and f_0 can be identified via the axial-vector current to be the pion decay constant at tree-level. We want to note that the vacuum scalar density, which is an order parameter for the spontaneous chiral symmetry since

$$\langle 0|\bar{\psi}\psi|0\rangle = \langle 0|\bar{\psi}_L\psi_R|0\rangle + \langle 0|\bar{\psi}_R\psi_L|0\rangle, \tag{3.18}$$

can be related to B_0 via

$$\sum_{i=u,d,s} m_i \langle 0|\bar{\psi}_i \psi_i|0\rangle \;=\; -(m_u + m_d + m_s) f_0^2 B_0. \tag{3.19}$$

With this lowest order effective Lagrangian one finds for the boson masses

$$\begin{aligned} m_{\pi^\pm}^2 &= B_0(m_u + m_d), \qquad m_{K^\pm}^2 = B_0(m_s + m_u), \\ m_{K^0}^2 &= B_0(m_s + m_d). \end{aligned}$$

At the next higher order, besides *chiral loops* constructed from the propagators and interactions of $\mathcal{L}_2$, also tree-level terms have to be taken into account:

$$\begin{aligned} \mathcal{L}_4 \;=\; & -L_1[\mathrm{Tr}(\partial_\mu \Sigma \partial^\mu \Sigma^\dagger)]^2 \;-\; L_2 \mathrm{Tr}(\partial_\mu \Sigma \partial_\nu \Sigma^\dagger)\mathrm{Tr}(\partial^\mu \Sigma \partial^\nu \Sigma^\dagger) \\ & -L_3 \mathrm{Tr}[(\partial_\mu \Sigma \partial^\mu \Sigma^\dagger)^2] \;+\; L_4 \mathrm{Tr}(\partial_\mu \Sigma \partial^\mu \Sigma^\dagger)\mathrm{Tr}(\chi \Sigma^\dagger + \Sigma \chi^\dagger) \\ & +L_5 \mathrm{Tr}[\partial_\mu \Sigma \partial^\mu \Sigma^\dagger (\chi \Sigma^\dagger + \Sigma \chi^\dagger)] \;-\; L_6 [\mathrm{Tr}(\chi \Sigma^\dagger + \Sigma \chi^\dagger)]^2 \\ & -L_7 [\mathrm{Tr}(\chi \Sigma^\dagger - \Sigma \chi^\dagger)]^2 \;-\; L_8 \mathrm{Tr}(\chi \Sigma^\dagger \chi \Sigma^\dagger + \Sigma \chi^\dagger \Sigma \chi^\dagger). \end{aligned} \tag{3.20}$$

Here we skipped terms with coefficients L_9, L_{10} which would describe couplings to the external field tensors $L_{\mu\nu}, R_{\mu\nu}$, and also two terms which are not coupled to the Σ-field at all, and therefore are not of interest. The constants L_i describe the left-over influence of the high energy interactions in this low energy expansion and are the afore mentioned *low energy constants (LECs)* or *Gasser-Leutwyler constants*. When dealing with chiral SU(2), three of these operators become redundant and only L_1, L_2, L_4, L_6, and L_7 have to be considered. We would also like to mention some arbitrariness in defining the LECs and quark masses, known as the *Kaplan-Manohar mass ambiguity* [48]: shifting the LECs and simultaneously the quark masses in a certain way will lead to identical results.

A power counting argument due to Weinberg [49] gives the overall chiral dimension for a general connected diagram with N_d vertices of $\mathcal{O}(p^d), d = 2, 4, \ldots$ and L loops to be

$$D \;=\; 2L \;+2\; \;+\; \sum_d N_d (d-2). \tag{3.21}$$

This allows one to identify the relevant loop contributions and tree-level contributions up to some given order. For example, the leading order $D = 2$ is obtained with $L = 0$ and $d = 2$, i.e., only the tree-level contributions from $\mathcal{L}_2$; while for the second order one has to consider both $L = 0, d = 4$ (tree-level from $\mathcal{L}_4$) and $L = 2, d = 2$ (one-loop from $\mathcal{L}_2$). The loop-contributions are in general divergent and have to be renormalized. If considered only to some specific order, the Lagrangian is not-renormalizable, as it is an effective theory. But the operators at the next higher order guarantee the renormalizability of the loop-integrals up to that given order. Practically therefore the LECs have to be renormalized, e.g., at next-to-leading (NLO) by using dimensional regularization:

$$L_i^{\mathrm{ren}} \;=\; L_i \;-\; \Gamma_i \frac{\mu^{2\epsilon}}{32\pi^2}\left(\frac{1}{\hat{\epsilon}} - 1\right) \tag{3.22}$$

with some numerical constants Γ_i [43, 44]. Of course, the LECs are now defined at some reference mass scale μ. The relation between different scales follows directly to be:

$$L_i^{\mathrm{ren}}(\mu_2) \;=\; L_i^{\mathrm{ren}}(\mu_1) \;+\; \frac{\Gamma_i}{(4\pi)^2} \log \frac{\mu_1}{\mu_2}. \tag{3.23}$$

The remaining part of the loop integration enters the formulae in a non-polynomial contribution of the form

$$m_q^n \log m_q^m,$$

referred to as *chiral logarithms*. At this stage we want to postpone giving explicit formulae for the pion mass and decay constant until the discussion of the lattice formulation of χPT used in conjunction with partial quenching (Chapter 4).

One way to gather informations about the LECs is of course to use experimental data and phenomenological estimates as an input and try to obtain a set of values, which best describes this data. From their origins in $\mathcal{L}_4$, it becomes clear that L_1, L_2, and L_3 should be sensitive to elastic $\pi\pi$ and πK processes, while L_4, L_5 generate mass corrections to the decay constants. The masses of the pseudo-scalar mesons itself will be affected by L_6, L_7, L_8. In Sec. 5.2 we describe how some of these LECs can be obtained by lattice simulations. In contrast to experiment, where the quark masses are fixed by nature, such simulations are also able to vary these parameters. That is turning a disadvantage of the lattice approach, the fact that one still needs an extrapolation in the quark masses, into an unique opportunity for testing the prediction of χPT via a first principle approach.

3.2 Lattice χPT

When applying χPT to lattice results, one has to be aware of several aspects related to the specific formulation on the lattice. First of all, the lattice regularization introduces artifacts due to the finite value of the lattice spacing and the finite volume. If Wilson fermions are used, the doublers are removed by introducing an additional mass term for the unwanted fermions. Because in χPT the mass term is the origin of explicit symmetry breaking, one has to treat the symmetry breaking caused by lattice artifacts on the same footing. We will discuss this point in the following section. Also effects originating from the finite volume can be treated in χPT. First we will concentrate on lattice QCD without a twisted mass term and provide a treatment of lattice artifacts occurring there, and in a second step account for QCD$^{\mathrm{TM}}$ as the underlying theory for the lattice χPT$^{\mathrm{TM}}$.

3.2.1 Lattice artifacts in untwisted QCD

Non-zero lattice spacing

In this section we want to explain in which way effects of non-zero lattice spacings can be incorporated in χPT. For a recent overview on this we refer to [50]. A perturbative treatment of discretization effects can be done using the *Symanzik's effective action* [51]: here, one considers an action in the continuum, which describes the lattice theory below the cut-off $1/a$. This effective theory is organized in powers of the lattice spacing a:

$$S_{\mathrm{Symanzik}} \;=\; S_0 \;+\; \sum_{n=1}^{\infty} a^n S_n. \tag{3.24}$$

By construction, S_0 is the continuum QCD-action. In case of Wilson fermions the first relevant term, S_1, in this expansion is known to be the Pauli-term [52]:

$$aS_1 \;=\; ac_{\mathrm{SW}} \bar{\psi} \sigma_{\mu\nu} F^{\mu\nu} \psi, \tag{3.25}$$

with the Sheikholeslami-Wohlert parameter c_{SW}, which is in general a function of the gauge coupling β and the Wilson parameter r. This term breaks chiral symmetry in the same way as the usual mass term does. One therefore may include an additional "mass parameter" ρ in the chiral Lagrangian, with the same spurionic symmetry properties as the ordinary mass term χ. This new term is usually related to the afore mentioned parameters via

$$\rho = 2W_0\, a\, c_{\mathrm{SW}}, \tag{3.26}$$

where W_0 is an unknown dimensionful constant.[1] Of course, this term should be small compared to the scale up to which the chiral expansion holds. The lowest order effective Lagrangian including lattice artifacts now reads [53]:

$$\mathcal{L}_2^a \;=\; \frac{f_0^2}{4}\mathrm{Tr}[\partial_\mu \Sigma \partial^\mu \Sigma^\dagger] - \frac{f_0^2}{4}\mathrm{Tr}[(\chi+\rho)\Sigma^\dagger + \Sigma(\chi^\dagger+\rho^\dagger)]. \tag{3.27}$$

At $\mathcal{O}(a^2)$ not only terms enter, which break the chiral symmetry explicitly, but at NLO only the latter are relevant for the chiral Lagrangian, as has been shown in [54]. Up to $\mathcal{O}(a)$ or $\mathcal{O}(a^2)$ in the NLO-Lagrangian, one has to introduce five [53] or eight [54] new low-energy constants (W_i and W_i'), respectively:

$$\begin{aligned}
\mathcal{L}_4^a \;=\;& \mathcal{L}_4 \;+\; W_4\mathrm{Tr}[\partial_\mu \Sigma \partial^\mu \Sigma^\dagger]\mathrm{Tr}[\rho\Sigma^\dagger + \Sigma\rho^\dagger] \\
& + W_5\mathrm{Tr}[\partial_\mu \Sigma \partial^\mu \Sigma^\dagger(\rho\Sigma^\dagger + \Sigma\rho^\dagger)] \\
& - W_6\mathrm{Tr}[\chi\Sigma^\dagger + \Sigma\chi^\dagger]\mathrm{Tr}[\rho\Sigma^\dagger + \Sigma\rho^\dagger] \;-\; W_6'[\mathrm{Tr}(\rho\Sigma^\dagger + \Sigma\rho^\dagger)]^2 \\
& - W_7\mathrm{Tr}[\chi\Sigma^\dagger - \Sigma\chi^\dagger]\mathrm{Tr}[\rho\Sigma^\dagger - \Sigma\rho^\dagger] \;-\; W_7'[\mathrm{Tr}(\rho\Sigma^\dagger - \Sigma\rho^\dagger)]^2 \\
& - W_8\mathrm{Tr}[\rho\Sigma^\dagger\chi\Sigma^\dagger + \Sigma\rho^\dagger\Sigma\chi^\dagger] \;-\; W_8'\mathrm{Tr}[\rho\Sigma^\dagger\rho\Sigma^\dagger + \Sigma\rho^\dagger\Sigma\rho^\dagger].
\end{aligned} \tag{3.28}$$

In continuum χPT, the expansion was done in the parameters

$$\epsilon \sim \frac{p^2}{\Lambda^2} \sim \frac{\chi}{\Lambda^2}. \tag{3.29}$$

Adding the lattice artifacts, another parameter

$$\delta \sim \frac{\rho}{\Lambda^2} \tag{3.30}$$

occurs and the question about its relative ordering arises. At not too small quark masses and moderate lattice spacings the power counting scheme

$$\{\epsilon, \delta\} \ll \{\epsilon^2, \epsilon\delta\} \ll \{\delta^2\}, \tag{3.31}$$

may be sufficient. This means that $\mathcal{O}(a^2)$ is neglected, as applied in [53] (which also implies $\delta \ll \epsilon$). Of course, this is not the case, if one uses improved fermion actions, which are designed such that they correct for $\mathcal{O}(a)$ effects. There is another caveat present due to the phase structure of lattice QCD near zero quark mass. We will focus on that point in Sec. 3.3.

[1] Some authors define $W_0^* = W_0 c_{\mathrm{SW}}$.

Finite volume effects

Effects arising from only considering a finite volume ($L^3 \times T$) may also be taken into account. For a recent review on these we refer to [55]. In the literature, two ansätze are discussed:

Gasser and Leutwyler [56] proved that in an isotropic lattice with periodic boundary conditions the volume dependence only shows up in the propagators, which now also have to be periodic in all spatial directions. The momentum integrals have to be replaced by sums over the discretized momenta on the lattice. In that way it is possible to apply χPT to obtain values for the masses and decay constants at a given lattice size: $M(L), F(L)$ and consequently determine the corrections $M(L) - M(\infty)$, and $F(L) - F(\infty)$. Cf. [57] for recent results relevant for this work.

The second ansatz due to Lüscher is based on the relation between the mass shift in finite volume L^3 (assuming $T \to \infty$) and the scattering amplitude of the particle in question with the pion in infinite volume [58]. Cf. [59, 60, 61] for recent results.

For the combination of lattice sizes and pion masses we simulated (cf. the discussion concerning this point in Sec. 5.2), the finite size effects turned out to be small according to the findings of [57] or [60, 61], therefore we will not deal much more with this.

3.2.2 χPT$^{\mathrm{TM}}$

For the analysis of lattice data generated with a twisted mass action it is necessary to extend χPT including lattice artifacts to this situation. Because QCD$^{\mathrm{TM}}$ is organized in doublets of fermion fields, one is now restricted to an even number of quark-fields in the chiral Lagrangian, too. We follow [62] to work in the physical basis in the chiral Lagrangian. After introducing the additional mass term according to

$$\chi \;\to\; \chi(\omega) \;=\; 2B_0\, m \exp[-i\omega\tau_3] \tag{3.32}$$

the fields are shifted

$$\Sigma \;\to\; \Sigma' \;=\; \exp[i\frac{\omega}{2}\tau_3]\,\Sigma\,\exp[i\frac{\omega}{2}\tau_3] \tag{3.33}$$

by an axial rotation and χ, ρ accordingly to get a diagonal mass term independent of ω. Therefore, the ρ-term, modeling the lattice artifacts,

$$\rho(\omega) \;= 2W_0\, a\, c_{SW}\; \exp[i\omega\tau_3] \tag{3.34}$$

now depends on the twist angle. This replacement has to be done in $\mathcal{L}_2^a$, Eq. (3.27), and $\mathcal{L}_4^a$, Eq. (3.28). As a consequence the minimum of the effective action, around which one has to expand the fields, is no longer located at vanishing meson fields corresponding to $\Sigma_0 = \mathbb{1}$ but gets shifted in the τ_3 direction [62]. A detailed study of this potential will lead to different possible phase structures of lattice QCD near zero quark mass (see next section). A feature of the so obtained formulae [62, 34], is that the $\mathcal{O}(a)$-improvement manifests itself in the way, that lattice terms of that order always appear with a factor $\cos\omega$ and therefore vanish at maximal twist. This is the manifestation of "automatic" $\mathcal{O}(a)$ improvement discussed before. We postpone to give the explicit formulae until we discussed PQχPT$^{\mathrm{TM}}$(Sec. 4.2).

3.3 The phase structure of lattice QCD

The remainder of our treatment of QCD near zero quark mass will be a discussion of the (zero-temperature) phase structure of lattice QCD using Wilson fermions. First we will follow the ansatz of Sharpe and Singleton for a pair of untwisted fermions ($N_f = 2$) and use χPT including lattice discretization effects to conclude that two different phase structure scenarios are possible. These phase structures show up as a consequence of a "competition" between the mass term χ and the lattice artifacts term ρ, as introduced in the previous section. We will show that, depending on the sign of the lattice term, one encounters a situation with an *Aoki phase* present or not. The latter we will refer to as the *normal scenario*. The main features of the Aoki phase are that flavor and parity are broken spontaneously and $\langle\bar{\psi}i\gamma_5\tau_3\psi\rangle$ has a non-zero value. The extension to QCD$^{\mathrm{TM}}$ is discussed afterwards, which will lead to an extended phase structure picture for lattice QCD.

As an appetizer for this section we want to restate the "history" of the phase structure of untwisted Wilson fermions ($N_f = 2$) a little and also already mention some of our findings based on numerical simulations, which we will present in detail in Sec. 5.3. First numerical studies (cf. [63] for an overview and references therein) supported the existence of an Aoki phase at weak coupling, while a recent work by Ilgenfritz et al. [25] only found such a phase for couplings $\beta < 4.6$ (using Wilson Plaquette action for the gauge part). On the contrary, already [64] reported on metastabilities in the plaquette expectation value in the region $4.8 \leq \beta \leq 5.22$: Depending on the starting condition, i.e., starting either from an ordered or disordered configuration, the runs thermalized at different values for the average plaquette. The JLQCD-collaboration [65] reported on a similar bulk first-order phase transition in the $N_f = 3$ case, using improved Wilson fermions and plaquette gauge action. This phase transition weakened with increasing β. They also took improved gauge actions (RG-improved and Lüscher-Weisz gauge action (cf. App. B)) into account with the result that the phase transition disappeared, too. During our numerical studies of the twisted mass action, we also found strong metastabilities and were able to relate these to phases in which the measured quark mass has opposite signs. The presence of these metastabilities implies a lower bound on the pion mass, which came out to be unsatisfactory high, if Wilson gauge action was employed. Switching to RG-improved gauge actions improved the situation (for details, cf. Sec. 5.3.2).

3.3.1 Aoki- and normal-scenario

We will discuss the chiral Lagrangian based ansatz of Sharpe and Singleton [66, 67] leading to two different phase structure scenarios for $N_f = 2$ flavors of Wilson fermions. Taking $\mathcal{L}_a^2 + \mathcal{L}_4^a$, Eqs. (3.27), (3.28), as a starting point, the effective potential up to second order in the quark mass parameter can be written as

$$V(\Sigma) \;=\; -c_1\, u_0 \;+\; c_2\, u_0^2. \tag{3.35}$$

Here we used a parametrization for the field Σ

$$\Sigma \;\equiv\; u_0 \mathbb{1} \;+\; i \sum_{j=1}^{3} u_j \tau_j, \quad u_\mu \in \mathbb{R}. \tag{3.36}$$

Collecting the u_μ into a 4-vector

$$u \;=\; (u_0, \boldsymbol{u}) \;=\; (u_0, u_1, u_2, u_3), \tag{3.37}$$

this vector has to be of unit length: $u \cdot u = 1$. Since we are only interested in finding Σ_0, which minimizes the potential V and around which the expansion has to be performed, terms containing derivatives in $\mathcal{L}_2^a$, $\mathcal{L}_4^a$ do not have to be considered.

Before we turn to this determination of the minimum, we first will have to examine the origin and (relative) size of the constants c_1, c_2. Clearly both the quark mass and the lattice term contribute to c_1 in first order:

$$c_1 \;\sim\; \epsilon + \delta, \tag{3.38}$$

while

$$c_2 \;\sim\; \epsilon^2 + \epsilon\delta + \delta^2. \tag{3.39}$$

(ϵ, δ are defined in Eqs. (3.29), (3.30).) Here, we are continuing the discussion of organizing the power counting in lattice χPT, that we had postponed in Sec. 3.2.1. At *physical masses*, i.e., small and fixed ϵ, in the continuum limit ($\delta \to 0$) c_1 is given entirely by the quark masses and c_2 may be neglected in the discussion of the phase structure. Hence the symmetry breaking is exactly the same as in the continuum. The case $\epsilon \sim \delta$, sometimes referred to as *generic small masses*, leads to a shift in the critical mass, and c_2 is still suppressed by one order of magnitude compared to c_1. The situation changes, if we are dealing with quark masses of the order $m_q \sim a^2\Lambda^3$, i.e., $\epsilon \sim \delta^2$, resulting in $c_1 \sim c_2$. Now a competition between the two terms in the potential sets in, which may lead to a non-trivial phase structure. In all three cases, c_1 depends on the (shifted) bare quark mass. In the last case, c_2 is a function of the bare gauge coupling.

In the first two cases the potential clearly has its minimum at $\Sigma_0 = \pm\mathbb{1}$, i.e., $u_{\min} = (\pm 1, \mathbf{0})$, depending on the sign of c_1. The latter is completely given by the sign of the quark mass. (Remember that negative quark masses correspond to situations below the critical mass parameter $\mu_\kappa < \mu_{\kappa\text{crit}}$.) Passing from negative to positive c_1 induces a jump in Σ_0. Assuming now $c_1 \sim c_2$, the extremum occurs at

$$u_{0\text{ext}} \;=\; \frac{c_1}{2c_2} \;\sim\; \mathcal{O}(1). \tag{3.40}$$

First we will discuss the case $c_2 > 0$, leading to the *Aoki phase scenario*. The extremum at $u_{0\text{ext}}$ is a (global) minimum, which will lie outside the allowed range, if $|c_1/(2c_2)| > 1$, resulting again in $\Sigma_0 = \pm\mathbb{1}$, depending on whether c_1 is positive or negative (as before). Given now $|c_1/(2c_2)| < 1$, the vacuum state has to develop non-zero components $\boldsymbol{u}_{\min}$, which can be assumed to be $u_{1\min} = u_{2\min} = 0$, $u_{3\min} \neq 0$:

$$\Sigma_0 \;=\; \frac{c_1}{2|c_2|}\,\mathbb{1} \;\pm\; i\sqrt{1 - \frac{c_1^2}{4c_2^2}}\,\tau_3. \tag{3.41}$$

This state is no longer invariant under a vector SU(2) transformation ($L = R$) leading to a spontaneous symmetry breakdown $\mathrm{SU}_V(2) \to \mathrm{U}(1)$. Considering the scalar and pseudoscalar vacuum densities,

$$\begin{aligned} \langle\bar\psi\psi\rangle \;&\propto\; \mathrm{Tr}[\Sigma_0 + \Sigma_0^\dagger] \;\propto\; u_{0\min}, \\ \langle\bar\psi i\gamma_5\tau_3\psi\rangle \;&\propto\; i\mathrm{Tr}\Big[\tau_3(\Sigma_0 - \Sigma_0^\dagger)\Big] \;\propto\; u_{3\min}, \end{aligned}$$

respectively, it becomes obvious that if $u_{3\min} \neq 0$, not only flavor is broken spontaneously but also parity: $\langle \bar{\psi} i\gamma_5 \tau_3 \psi \rangle \neq 0$. Aoki proposed the existence of such a phase [68], where flavor and parity are spontaneously broken, to have a structure in the μ_κ-β plane as sketched in Fig. 3.1, left panel, where this phase is labeled "B". According to Goldstone's theorem inside this phase one expects to find two massless Goldstone bosons and one massive meson, which is indeed the case, cf. [66] and Fig. 3.1, upper right panel. To read off the pion masses from the potential, Eq. (3.35), one has to expand Σ around the vacuum $\Sigma = \Sigma_0 \, \Sigma'$, where for Σ' one inserts the usual form:

$$\Sigma' \;=\; \exp\left[\frac{i \sum_{a=1}^{3} \phi_a(x) \tau_a}{f_0}\right]. \tag{3.42}$$

In this way u_0' (from the parametrization of Σ' according to Eq. (3.36)) is obtained as a function of the pion fields $\phi_a(x)$, the terms quadratic in the latter in the potential allow to determine the masses. $\phi_{1,2}$ are related to the charged pions, while ϕ_3 represents the neutral one.

The width of the Aoki phase is given by $\Delta(am) \sim (a\Lambda)^3$ as a consequence of the assumptions initially made. Varying c_1 from large negative to large positive values smoothly varies Σ_0 from $-\mathbb{1}$ to $+\mathbb{1}$, passing through the Aoki phase. In the continuum limit the width of the phase tends towards zero, resulting in a single second order phase transition point where again a jump in Σ_0 occurs. Exactly the same situation is realized in the continuum.

In contrast to the Aoki scenario the *normal scenario* takes place for $c_2 < 0$. The potential now possesses a (global) maximum at $u_{0\text{ext}}$ and depending on the sign of c_1 we recover the situation $\Sigma_0 = \pm\mathbb{1}$, with a jump occurring if c_1 flips sign. No spontaneous breaking of flavor symmetry takes place and all three mesons have the same mass, cf. [66] and Fig. 3.1, lower right panel.

3.3.2 Phase structure of QCD$^{\text{TM}}$

The addition of a twisted mass term gives rise to a third term proportional to u_3 in the potential. Eq. (3.35) now becomes

$$V(\Sigma) \;=\; -c_1 \, u_0 \;+\; c_2 \, u_0^2 \;+\; c_3 \, u_3. \tag{3.43}$$

Note that this parametrization corresponds to the twisted basis, as is appropriate for discussing the phase structure present in numerical simulations. c_3 is proportional to the twisted mass parameter μ. The implications of this term are discussed in [69, 70, 71, 72], which we will follow now. In general, a non-zero c_3 leads to an explicit flavor symmetry breaking. As a consequence, only the two charged pions are still degenerate in mass. The statements concerning the relative size of the lattice artifacts compared to the mass terms (twisted and untwisted) remain valid: for physical quark masses one recovers the continuum situation with Σ_0 oriented in the $\mathbb{1}$-τ_3 plane according to the relative size of m_q and μ. This situation also applies, if just one of the two is of physical size. For generic small masses one just encounters the usual shift in the critical mass. Different scenarios for the phase structure appear as before, when both m_q and μ are of the order $a^2\Lambda^3$. The extremum of the potential now gets shifted in the τ_3 direction.

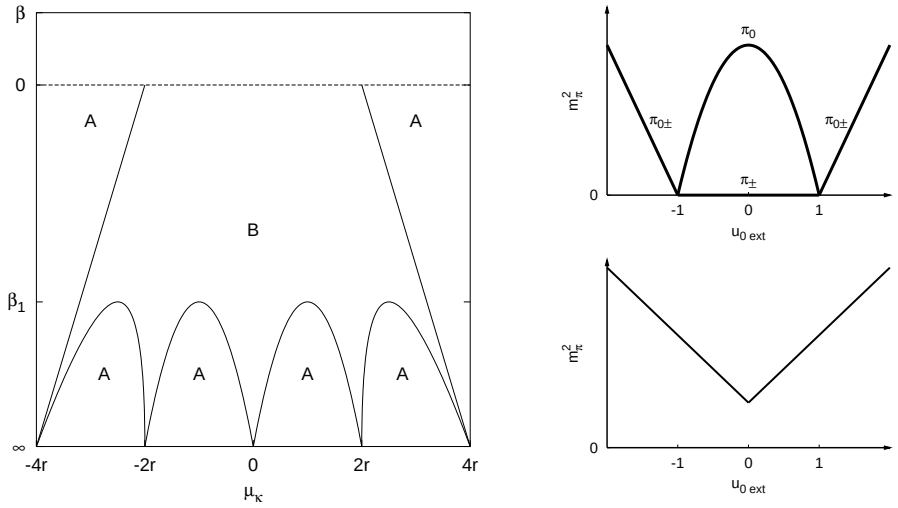

Figure 3.1: Left panel: *Aoki phase scenario [68] in the μ_κ-β plane.* A *labels the phase with parity and flavor unbroken and three massive pions, while* B *is the Aoki-phase with $\langle\bar{\psi}i\gamma_5\tau_3\psi\rangle \neq 0$. There are five "fingers" of the Aoki-phase, separating the phases* A*, which start to emerge at a coupling β_1, associated with different continuum limits. The continuum limit of interest is the one near $\mu_\kappa = 4r$.* Right panels: *Pion masses squared in the two different scenarios as functions of $u_{0ext} = c_1/(2c_2)$, according to [66].* Upper right panel: *m_π^2 in the Aoki-phase scenario ($c_2 > 0$): in the Aoki-phase ($-1 < u_{0ext} < 1$) two pions are massless ($\pi_\pm$), while π_0 remains massive. Outside all three pions become degenerate, with zero mass at the boundaries and non-zero outside.* Lower right panel: *m_π^2 in the normal-phase scenario ($c_2 < 0$): all three pions are degenerate with non-vanishing mass; the minimal pion mass appears at $u_{0ext} = 0$, where Σ_0 flips sign.*

To find the extremum, one has to solve the quartic equation (the relation $u_3^2 = 1 - u_0^2$ with the restriction $u_0 \in [-1, 1]$ has been used):

$$0 \;=\; u_0^4 - \frac{c_1}{c_2}u_0^3 + \frac{c_1^2 - 4c_2^2 + c_3^2}{4c_2^2}u_0^2 + \frac{c_1}{c_2}u_0 - \frac{c_1^2}{4c_2^2}, \tag{3.44}$$

and identify the solution $u_{0\min}$ belonging to the minimum in the allowed parameter space. The sign of $u_{3\min}$ is determined by the sign of c_3:

$$u_{3\min} \;=\; -\mathrm{sign}(c_3)\sqrt{1 - u_{0\min}^2}. \tag{3.45}$$

The solution for u_3 has been given to first order in c_3 by [69] depending on the sign of c_2.

$$u_{3\min} \;=\; \begin{cases} -\frac{c_3}{|c_1|-2c_2} + \mathcal{O}(c_3^2), & c_2 > 0, \;\; \alpha > 1 \\ -\mathrm{sign}(c_3)\sqrt{1-\alpha^2} - \frac{\alpha^2}{1-\alpha^2}\frac{c_3}{4c_2} + \mathcal{O}(c_3^2), & c_2 > 0, \;\; \alpha < 1 \\ -\frac{c_3}{|c_1|+2|c_2|} + \mathcal{O}(c_3^2), & c_2 < 0 \end{cases}, \tag{3.46}$$

where $\alpha = \frac{|c_1|}{2|c_2|}$. The authors of [71, 72] give the values for the charged pion masses squared and their mass-splitting compared to the neutral one in terms of $u_{0\min}$ and $u_{3\min}$

$$m_{\pi^\pm}^2 \;=\; c_1 u_{0\min} - c_3 u_{3\min} - 2c_2 u_{0\min}^2, \quad \Delta m_\pi^2 \;=\; m_{\pi_0}^2 - m_{\pi^\pm}^2 \;\propto\; 2c_2 u_{3\min}^2. \tag{3.47}$$

Remarkably, if enlarging the parameter space by the twisted mass parameter, the two different scenarios are related by a rotation of $\pi/2$ in the μ_κ-μ plane [71, 72]. To see this, consider writing $u = (\cos\vartheta, 0, 0, -\sin\vartheta)$ and shifting the variables according to $c_1 = c_3'$, $c_3 = -c_1'$, $c_2 = -c_2'$, $\vartheta = \vartheta' - \pi/2$. Before and after the shift the potential now reads:

$$\begin{aligned} V(\Sigma) &= -c_1\cos\vartheta + c_2\cos^2\vartheta - c_3\sin\vartheta, \\ V'(\Sigma') &= -c_3'\sin\vartheta' + c_2'\cos^2\vartheta' - c_1'\cos\vartheta' - c_2'. \end{aligned}$$

Both are of the same form (neglecting the constant shift), with the rôles of the twisted and untwisted quark mass component interchanged and the sign of c_2 changed. Therefore, in the normal scenario the analogue of the Aoki phase extends in the μ-direction rather than in the μ_κ direction.

We first concentrate on $c_2 > 0$, which for vanishing μ led to the Aoki-phase scenario. For non-vanishing μ the vacuum Σ_0 changes continously from $-\mathbb{1}$ to $+\mathbb{1}$, if $\mu \neq 0$ is kept fixed and μ_κ is varied from large negative to large positive values. As a consequence the Aoki-phase disappears for non-zero twisted mass. On the contrary, the u_3 component of Σ_0 flips sign discontinuously for $|c_1/(2c_2)| < 1$, if μ changes from positive to negative values. The latter can be seen from the term proportional to $\sqrt{1-\alpha^2}$ in Eq. (3.46). Summarizing the findings for positive c_2, we conclude the following phase-structure in the μ_κ-μ plane (see Fig. 3.2, upper panel): there is an Aoki phase for $\mu = 0$, which coincides with the first order phase transition line when varying μ.

Considering now the normal scenario ($c_2 < 0$) or, according to the discussion of the consequences of a sign flip in c_2, the rotated Aoki scenario. At zero untwisted quark mass ($c_1 = 0$), there persists a jump in $u_{0\min} = \pm\sqrt{1 - {u_{3\min}}^2}$ for values of $|c_3| < 2|c_2|$, if c_1 is varied from positive to negative values. This discontinuity gets weaker with increasing c_3 and disappears completely for $|c_3| > 2|c_2|$ [69, 71]. This is exactly the rotated first order phase transition line from the Aoki scenario. The resulting phase structure is depicted in Fig. 3.2, lower panel. The pion masses for the charged pions are non-vanishing. They take their minimum at the phase transition line at which they are constant. This is easily seen, if one takes into account that at the phase transition line ($c_1 = 0$) the quartic equation (3.44) reduces to a quadratic equation in u_0^2, with solutions $u_{0\text{ext}}^2 = 0$ and $u_{0\text{ext}}^2 = 1 - c_3^2/(4c_2^2)$. Identifying the last one as the minimum of the potential at the phase transition line, from Eq. (3.47) one gets $m_{\pi_\pm}^2 \propto 2|c_2|$. From the shift of the neutral pion mass, one sees that at $c_3 = c_1 = 0$ ($u_{0\min} = 1$, $u_{3\min} = 0$) all three pions are mass degenerate, while at $|c_3| = 2|c_2|$ ($u_{0\min} = 0$, $u_{3\min} = \pm 1$) the neutral pion mass vanishes because of $\Delta m_\pi^2 = -2|c_2|$. This is the second order endpoint of the first order phase transition line.

We discussed the different possible phase structure scenarios for the QCD$^{\text{TM}}$ action. At small quark masses the sign of the coefficient c_2 representing the lattice artifacts decides which scenario actually applies. The whole discussion is build upon the assumption of quark masses being comparable to the lattice artifacts squared, i.e., lattice artifacts already dominating the situation. In [73] a detailed discussion on the pion mass splitting and phase structure for QCD$^{\text{TM}}$ has been presented: there, only the ratio of the quark mass term to the lattice artifacts has to be fixed in the beginning with no further constraints. A remarkable result of that work is a relation between the pion mass splitting and the coefficient c_2 and therefore the realized phase structure scenario. In particular it followed that $m_{\pi^\pm}^2 > m_{\pi^0}^2$ corresponds to negative c_2.

At the end of this chapter we present the phase structure picture (Fig. 3.3), which we

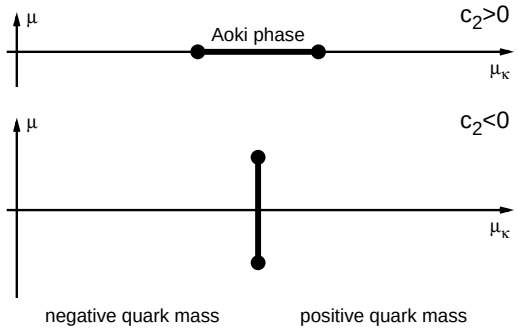

Figure 3.2: *Phase structure in the μ_κ-μ plane near zero quark mass, if $m_q \propto a^2\Lambda^3$. Both scenarios are related by rotation of $\pi/2$.* Upper panel: *Aoki phase scenario in the μ_κ-μ plane. The first order phase transition line coincides with the Aoki phase.* Lower panel: *Normal phase scenario, first order phase transition line orthogonal to the μ_κ-axis, separating the positive and negative quark mass phase.*

deduced from our numerical results in consistency with the afore mentioned results from other groups. We plot the space spanned by β, κ, and μ. (The β-axis does not continue until zero.) Below a certain coupling β_1 an Aoki phase is present indicated by the critical lines in the β-μ_κ plane. (Note that only one "finger" is depicted in the figure.) Above β_1 we find a situation with a critical line in the β-μ plane in agreement with the normal scenario where no Aoki phase is present. We will present our numerical studies, which led us to this picture, in Sec. 5.3.

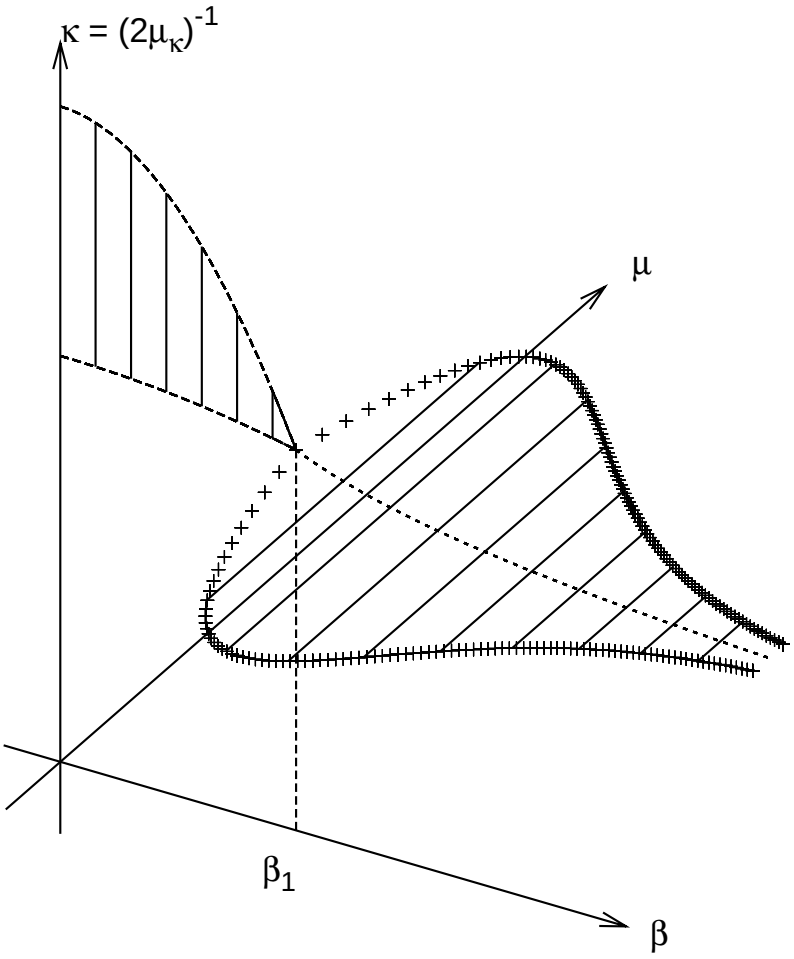

Figure 3.3: *The QCD^{TM} phase diagram as observed for Wilson plaquette and DBW2 gauge action (cf. Sec. 5.3). Depicted is the (β, κ, μ) space (bare quantities). The crosses mark the boundary of the first order phase transition surface. At strong gauge coupling there is the surface containing the Aoki phase (ending at $\beta = \beta_1$). Only one "finger" of this phase is shown, since the plot does not extend down to $\beta = 0$.*

Chapter 4

Partially quenched QCD

Partially quenched QCD, in contrast to fully quenched or unquenched QCD, is dealing with two sorts of quarks: those simulated dynamically and appearing in the virtual quark loops as well as in the external states are referred to as *sea quarks*; while those only appearing as external states are called *valence quarks*. The latter are "quenched" in the language of the lattice-QCD. Consequently at full quenching one only deals with valence quarks, and in unquenched QCD only sea quarks are present. From the numerical point of view, partial quenching is relatively easy to realize: while the dynamical quarks are just the ones included during the simulation with hopping-parameter(s) κ_{sea}, one may calculate quark propagators on the gauge configurations produced in that way with different values for the hopping-parameter $\kappa_{\text{val}} \neq \kappa_{\text{sea}}$. This is numerically cheaper than producing configurations at this mass. Of course, one has to relate these results in some way to the ones from χPT based on ordinary QCD, if one wants to use them for, e.g., the extraction of LECs.

Partial quenching can be introduced to the usual QCD-Lagrangian by the following procedure [74, 75, 76]: the valence and sea quarks are described by normal fermion fields $q_{v_1}, \ldots, q_{v_{N_v}}$, $q_{s_1}, \ldots, q_{s_{N_s}}$ with masses m_{v_i}, m_{s_i}. To cancel the virtual contributions from the valence quarks, one adds bosonic spin $1/2$ fields $\tilde{q}_{v_1}, \ldots, \tilde{q}_{v_{N_v}}$ (*ghost fields*) with identical masses m_{v_i}. Because of

$$\int \mathcal{D}[\bar{q}\ , q]\ \exp[-\bar{q}\ (\not{D} + m_q)q] \quad = \quad \det(\not{D} + m_q), \tag{4.1}$$

$$\int \mathcal{D}[\tilde{q}^\dagger, \tilde{q}]\ \exp[-\tilde{q}^\dagger(\not{D} + m_q)\tilde{q}] \quad = \quad \det(\not{D} + m_q)^{-1} \tag{4.2}$$

the needed cancellation in the partition function occurs. Now one can translate this construction to the application of χPT aiming for a *Partially Quenched Chiral Perturbation Theory* (PQχPT) by observing that in the massless case the Lagrangian respects a graded $\mathrm{SU}(N_s + N_v|N_v) \otimes \mathrm{SU}(N_s + N_v|N_v)$ symmetry, which is dynamically broken down to $\mathrm{SU}(N_s + N_v|N_v)$. The pseudo-Goldstone fields are parametrized in a graded matrix

$$\Sigma \ = \ \begin{pmatrix} A & B \\ C & D \end{pmatrix}.$$

A and D contain the pseudo-Goldstone bosons, made from constituents of equal statistics, and are therefore $(N_s + N_v)^2$ and N_v^2 quadratic matrices of commuting numbers,

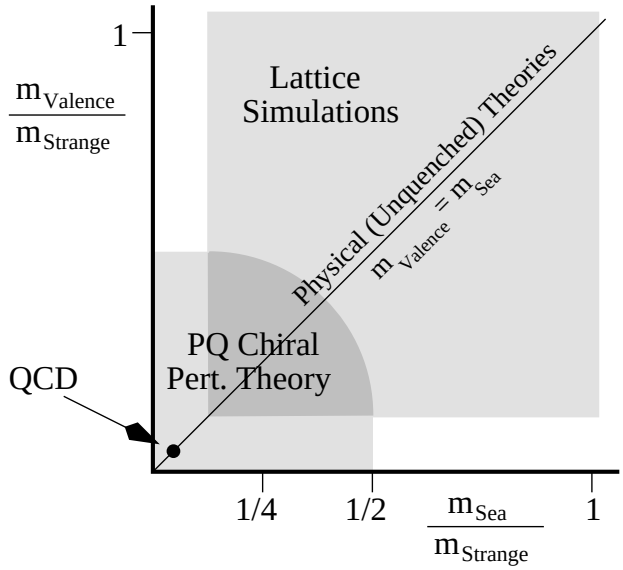

Figure 4.1: *Illustrating the utility of PQχPT: in the m_{sea}-m_{val} plane the range of current lattice simulations using PQχPT and the (assumed) convergence radius are shown. The diagonal line refers to fully unquenched simulations, with the "real world" QCD-point indicated. Plot taken from [79], courtesy of S.R. Sharpe and R.S. van de Water.*

respectively. The matrices B and C contain anti-commuting elements, because their constituents are bosonic and fermionic quarks. One may represent the element of the graded supergroup like before as

$$\Sigma \;=\; \exp\left(\frac{2i}{f_0}\Phi\right), \tag{4.3}$$

where now the supertrace[1] of the field Φ has to vanish:

$$\mathrm{sTr}\Phi \;=\; 0. \tag{4.4}$$

Instead of constructing a basis of supertraceless generators, one can also follow [77, 78] to introduce a singlet field $\Phi_0 \propto \mathrm{sTr}\Phi$ with a mass term, which is sent to infinity in the end. The chiral Lagrangian for the partially quenched case is obtained from the normal (unquenched) one by replacing the normal traces by supertraces and enlarging the mass matrices and lattice terms χ and ρ, respectively. By construction the unquenched (sea) sector now describes the same physics with the universal LECs [76, 77].

This situation is illustrated by Fig. 4.1 (taken from [79]), showing the m_{sea}-m_{val} plane. The expected convergence radius of χPT (assumed to be $\frac{m_{\mathrm{strange}}}{2}$) is indicated as well as the region where present lattice simulation are done. The diagonal line ($m_{\mathrm{sea}} = m_{\mathrm{val}}$) represents unquenched simulations. Of course, "real" QCD lies on this line. This plot nicely illustrates the advantage of using PQχPT: one enlarges the parameter space to extract additional information from the simulations at relatively low cost.

[1] The supertrace is defined as

$$\mathrm{sTr}\begin{pmatrix} A & B \\ C & D \end{pmatrix} \;=\; \mathrm{Tr}A - \mathrm{Tr}D.$$

In practical calculations done for the mesonic sector one uses a number of N_s sea quarks and $N_v = 2$ valence quarks to construct the different pseudo-Goldstone bosons. In the literature, results for mesonic masses and coupling constants in PQχPT are available: [80, 81, 77, 54, 79, 82, 83].

4.1 Pion masses and decay constants from PQχPT

The pion decay constants and squared masses have been calculated for $N_s = 3$ mass non-degenerate dynamical sea quarks up to NLO in [53]. We generalized these formulae to the case of N_s sea quarks of equal mass [84], as needed for the analysis of our numerical data (Sec. 5.2). In the following the label A and B will denote generic quark indices, where S will be the label for a sea-quark, V for a valence quark. Note that for the cases $A \to B$, and $A, B \to S$, the limit has to be taken with some care. Also it is convenient to redefine χ and ρ, Eqs. (3.17), (3.26), to be dimensionless:

$$\chi = \frac{2B_0}{f_0^2}\, m, \tag{4.5}$$

$$\rho = \frac{2W_0\, c_{\mathrm{SW}}}{f_0^2}\, a. \tag{4.6}$$

The pion decay constant then reads

$$\begin{aligned}
\frac{f_{AB}}{f_0} &= 1 - \frac{N_s}{128\pi^2}\Bigg[(\chi_A+\chi_S+\rho_A+\rho_S)\log\Big(\frac{\chi_A+\chi_S+\rho_A+\rho_S}{2}\Big) \\
&\quad + (\chi_B+\chi_S+\rho_B+\rho_S)\log\Big(\frac{\chi_B+\chi_S+\rho_B+\rho_S}{2}\Big)\Bigg] \\
&\quad + \frac{1}{64N_s\pi^2}\Bigg[\chi_A+\chi_B+\rho_A+\rho_B-2\chi_S-2\rho_S \\
&\quad + \frac{2(\chi_A+\rho_A)(\chi_B+\rho_B)-(\chi_S+\rho_S)(\chi_A+\chi_B+\rho_A+\rho_B)}{\chi_B-\chi_A+\rho_B-\rho_A}\log\Big(\frac{\chi_A+\rho_A}{\chi_B+\rho_B}\Big)\Bigg] \\
&\quad + 2L_5(\chi_A+\chi_B) + 2W_5(\rho_A+\rho_B) + 4N_sL_4\chi_S + 4N_sW_4\rho_S,
\end{aligned} \tag{4.7}$$

and the pion mass squared

$$\begin{aligned}
\frac{m_{AB}^2}{f_0^2} &= \frac{\chi_A+\chi_B+\rho_A+\rho_B}{2} \\
&\quad + \frac{\chi_A+\chi_B+\rho_A+\rho_B}{32N_s\pi^2(\chi_B-\chi_A+\rho_B-\rho_A)}\Bigg[(\chi_A+\rho_A)(\chi_S-\chi_A+\rho_S-\rho_A)\log(\chi_A+\rho_A) \\
&\quad - (\chi_B+\rho_B)(\chi_S-\chi_B+\rho_S-\rho_B)\log(\chi_B+\rho_B)\Bigg] \\
&\quad + 4N_s(2L_6-L_4)\chi_S(\chi_A+\chi_B) + 2(2L_8-L_5)(\chi_A+\chi_B)^2 \\
&\quad + 4N_s(W_6-L_4)\chi_S(\rho_A+\rho_B) + 4N_s(W_6-W_4)\rho_S(\chi_A+\chi_B) \\
&\quad + 2(2W_8-W_5-L_5)(\chi_A+\chi_B)(\rho_A+\rho_B).
\end{aligned} \tag{4.8}$$

Effects up to $\mathcal{O}(a)$ are included, assuming a power counting scheme like Eq. (3.31).

The LECs L_k and $\mathcal{O}(a)$-constants W_k are defined at a scale $\mu = f_0$. For later purpose we already define

$$L_{Sk} \equiv L_k - c_k \log \chi_S, \tag{4.9}$$
$$W_{Sk} \equiv W_k - d_k \log \chi_S \tag{4.10}$$

to be these coefficients at a reference scale of a (fixed) sea quark mass χ_S: $\mu_S = f_0\sqrt{\chi_S}$. The translation coefficients are evaluated to be

$$c_4 = \frac{1}{256\pi^2},\ c_5 = \frac{N_s}{256\pi^2},\ c_6 = \frac{N_s^2+2}{512N_s^2\pi^2},\ c_8 = \frac{N_s^2-4}{512N_s\pi^2}, \tag{4.11}$$
$$d_4 = \frac{1}{256\pi^2},\ d_5 = \frac{N_s}{256\pi^2},\ d_6 = \frac{N_s^2+2}{256N_s^2\pi^2},\ d_8 = \frac{N_s^2-4}{256N_s\pi^2}. \tag{4.12}$$

Another common parametrization of these NLO-constants is

$$\alpha_k = 128\pi^2 L_k' = 128\pi^2 \left(L_{Sk} + c_k \log \frac{\chi_S}{16\pi^2} \right), \tag{4.13}$$
$$\omega_k = 128\pi^2 W_k' = 128\pi^2 \left(W_{Sk} + d_k \log \frac{\chi_S}{16\pi^2} \right), \tag{4.14}$$

with the primed quantities defined at a reference scale $\mu = 4\pi f_0$.

In the following we will give the deduced expressions for ratios of pion masses squared and decay constants as functions of quark mass ratios. The advantage of using these ratios lies in the fact that one gets rid of the unknown renormalization factors, as long as one stays at a fixed value for the gauge coupling. Also some volume and finite size dependence may cancel.

4.1.1 Sea quark mass dependence

For the sea quark mass dependence of the quantities in question we define a reference sea quark mass χ_R and express the formulae in terms of the ratios

$$\sigma = \frac{\chi_S}{\chi_R},\ \eta_S = \frac{\rho_S}{\chi_S},\ \eta_R = \frac{\rho_R}{\chi_R}. \tag{4.15}$$

The following two ratios will be considered in the analysis of our numerical data:

$$\begin{aligned} Rf_{SS} &\equiv \frac{f_{SS}}{f_{RR}} = \\ &= 1 + 4(\sigma-1)\chi_R(N_s L_{R4} + L_{R5}) + 4(\eta_S\sigma - \eta_R)\chi_R(N_s W_{R4} + W_{R5}) \\ &\quad - \frac{N_s\chi_R}{32\pi^2}\Big\{\sigma(1+\eta_S)\log[\sigma(1+\eta_S)] - (1+\eta_R)\log(1+\eta_R)\Big\} \\ &\quad + \mathcal{O}(\chi_R^2), \end{aligned} \tag{4.16}$$

and

$$\begin{aligned} Rn_{SS} &\equiv \frac{m_{SS}^2}{\sigma m_{RR}^2} = \\ &= 1 + \eta_S - \eta_R + 8(\sigma-1)\chi_R(2N_sL_{R6} + 2L_{R8} - N_sL_{R4} - L_{R5}) \\ &\quad + 8(\eta_S\sigma - \eta_R)\chi_R(2N_sW_{R6} + 2W_{R8} - N_sW_{R4} - W_{R5} - N_sL_{R4} - L_{R5}) \\ &\quad + \frac{\chi_R}{16\pi^2 N_s}\Big\{\sigma(1+2\eta_S)\log[\sigma(1+\eta_S)] - (1+2\eta_R)\log(1+\eta_R)\Big\} \\ &\quad + \mathcal{O}(\chi_R^2). \end{aligned} \tag{4.17}$$

In the latter we divided by the tree-level dependence, otherwise we could consider

$$Rm_{SS} \equiv \frac{m_{SS}^2}{m_{RR}^2} = \dots . \tag{4.18}$$

Instead of the scale-dependent combinations of L_R, also the *universal low-energy scales* $\Lambda_{3,4}$ [85] can be used:

$$\Lambda_3 = 4\pi f_0 \exp(-\alpha_{6845}), \tag{4.19}$$

$$\Lambda_4 = 4\pi f_0 \exp(\alpha_{45}/4), \tag{4.20}$$

where, in case of $N_s = 2$, we define:

$$\alpha_{6845} = 4\alpha_6 + 2\alpha_8 - 2\alpha_4 - \alpha_5, \tag{4.21}$$

$$\alpha_{45} = 2\alpha_4 + \alpha_5. \tag{4.22}$$

4.1.2 Valence quark mass dependence

For the valence quark mass dependence we introduce

$$\xi = \frac{\chi_V}{\chi_S}, \quad \eta_S = \frac{\rho_S}{\chi_S}, \tag{4.23}$$

if the simulation is done at a sea quark mass parameter χ_S and different values for the valence quark mass parameter χ_V are used. We consider the ratios

$$\begin{aligned} Rf_{VV} &\equiv \frac{f_{VV}}{f_{SS}} = \\ &= 1 + 4(\xi-1)\chi_S L_{S5} \\ &\quad - \frac{N_s\chi_S}{64\pi^2}\left[(1+\xi+2\eta_S)\log\left(\frac{1+\xi+2\eta_S}{2}\right) - 2(1+\eta_S)\log(1+\eta_S)\right] \\ &\quad + \mathcal{O}(\chi_S^2), \end{aligned} \tag{4.24}$$

$$\begin{aligned} Rf_{VS} &\equiv \frac{f_{VS}}{f_{SS}} = \\ &= 1 + 2(\xi-1)\chi_S L_{S5} + \frac{\chi_S}{64N_s\pi^2}\left[\xi - 1 - (1+\eta_S)\log\left(\frac{\xi+\eta_S}{1+\eta_S}\right)\right] \\ &\quad - \frac{N_s\chi_S}{128\pi^2}\left[(1+\xi+2\eta_S)\log\left(\frac{1+\xi+2\eta_S}{2}\right) - 2(1+\eta_S)\log(1+\eta_S)\right] \\ &\quad + \mathcal{O}(\chi_S^2), \end{aligned} \tag{4.25}$$

$$
\begin{aligned}
Rn_{VV} &\equiv \frac{m_{VV}^2}{\xi m_{SS}^2} = \\
&= 1 - \eta_S\frac{\xi-1}{\xi} + 8(\xi-1)\chi_S(2L_{S8}-L_{S5}) + 8N_s\frac{\xi-1}{\xi}\eta_S\chi_S(L_{S4}-W_{S6}) \\
&\quad + \frac{\chi_S}{16N_s\pi^2}\left[\frac{\xi-1}{\xi}(\xi+\eta_S) - (1+2\eta_S)\log(1+\eta_S)\right. \\
&\quad \left. + \frac{2\xi^2-\xi-\eta_S+3\eta_S\xi}{\xi}\log(\xi+\eta_S)\right] + \mathcal{O}(\chi_S^2),
\end{aligned} \tag{4.26}
$$

and

$$
\begin{aligned}
Rn_{VS} &\equiv \frac{2m_{VS}^2}{(\xi+1)m_{SS}^2} = \\
&= 1 - \eta_S\frac{\xi-1}{\xi+1} + 4(\xi-1)\chi_S(2L_{S8}-L_{S5}) + 8N_s\frac{\xi-1}{\xi+1}\eta_S\chi_S(L_{S4}-W_{S6}) \\
&\quad - \frac{\chi_S}{16N_s\pi^2}\left[(1+2\eta_S)\log(1+\eta_S) - \frac{\xi^2+\xi+\eta_S+3\eta_S\xi}{\xi+1}\log(\xi+\eta_S)\right] \\
&\quad + \mathcal{O}(\chi_S^2),
\end{aligned} \tag{4.27}
$$

where in the mass ratios the tree-level dependence has been divided out again. One could also define

$$Rm_{VV} \equiv \frac{m_{VV}^2}{m_{SS}^2} = \dots , \tag{4.28}$$

$$Rm_{VS} \equiv \frac{m_{VS}^2}{m_{SS}^2} = \dots . \tag{4.29}$$

Additional useful quantities are the double ratios, defined as

$$
\begin{aligned}
RRf &\equiv \frac{f_{VS}^2}{f_{VV}f_{SS}} = \\
&= 1 + \frac{\chi_S}{32N_s\pi^2}\left[\xi - 1 - (1+\eta_S)\log\left(\frac{\xi+\eta_S}{1+\eta_S}\right)\right] \\
&\quad + \mathcal{O}(\chi_S^2),
\end{aligned} \tag{4.30}
$$

and

$$
\begin{aligned}
RRn &\equiv \frac{4\xi m_{VS}^4}{(\xi+1)^2 m_{VV}^2 m_{SS}^2} = \\
&= 1 - \frac{\eta_S(\xi-1)^2}{\xi(\xi+1)} + 8N_s\chi_S\eta_S\frac{(\xi-1)^2}{\xi(\xi+1)}(L_{S4}-W_{S6}) \\
&\quad + \frac{\chi_S}{16N_s\pi^2}\left[\frac{\xi^2+\xi+\eta_S+3\eta_S\xi^2}{\xi(\xi+1)}\log(\xi+\eta_S) - (2\eta_S+1)\log(1+\eta_S)\right. \\
&\quad \left. - \frac{\xi-1}{\xi}(\xi+\eta_S)\right] + \mathcal{O}(\chi_S^2).
\end{aligned} \tag{4.31}
$$

4.1.3 $\mathcal{O}(a^2)$ corrections

The formulae in the preceding paragraph still neglect contributions of the order of a^2. For the pion masses the effects of including these terms have been calculated [54, 86]. For the afore defined ratios, Eqs. (4.26), (4.27) and double ratio, Eq. (4.31) this results in the following replacement of existing terms:

$$\eta_S(L_{S4} - W_{S6}) \;\rightarrow\; \eta_S(L_{S4} - W_{S6}) \;+\; \frac{\eta_S^2}{N_s}(N_s W_{S4} + W_{S5} - 2N_s W'_{S6} - 2W'_{S8}). \quad (4.32)$$

In other words, fitting the valence quark mass dependence of these ratios even without taking the $\mathcal{O}(a^2)$ terms into account explicitly, effectively also describes these corrections.

In case of the pion decay constant, the situation is expected to be similar. In any case, the analysis of our numerical data will exhibit that next-to-next-to-leading order (NNLO) contributions (as discussed in the remainder of this section) are much more important than these $\mathcal{O}(a^2)$ corrections.

4.1.4 NNLO-corrections

Although the complete NNLO formulae are not known in lattice PQχPT, the general pattern of such terms can be given [87, 79]:

$$\frac{\delta m_{AB}^2}{m_{AB}^2} \;=\; \alpha_1 \chi_S^2 \;+\; \alpha_2 \chi_S(\chi_A + \chi_B) \;+\; \alpha_3(\chi_A + \chi_B)^2 \;+\; \alpha_4(\chi_A^2 + \chi_B^2), \quad (4.33)$$

and similarly for the decay constant. Neglecting again lattice artifacts of $\mathcal{O}(a^2)$, we can assume that these corrections show a quadratic behavior in ξ and can be taken into account in our fits to numerical data by adding terms

$$D_X \chi_S^2(\xi - 1) \;+\; Q_X \chi_S^2(\xi - 1)^2 \quad (4.34)$$

to the considered valence quark mass dependence ratios. Here X denotes the ratio or double ratio in question, i.e., $X = fVV, \ldots, nVS$, for the single and $X = fd, nd$ for the double ratios. Because the single ratios already contain a term proportional to $(\xi - 1)$, one should introduce effective LECs L_X which include the D_X part:

$$L_X^{\text{eff}} \;=\; L_X \;+\; D_X \chi_S, \quad (4.35)$$

$$L_{fVV} \;=\; 4L_5, \quad (4.36)$$

$$L_{nVV} \;=\; 8(2L_8 - L_5). \quad (4.37)$$

The higher order terms are now only removed in the limit of vanishing quark masses $\chi_S \rightarrow 0$. In the double ratios the coefficients D_{nd} and D_{fd} are equal to zero, because the general structure of NNLO tree-graph contributions implies

$$D_{fVS} = \frac{1}{2} D_{fVV}, \quad D_{nVS} = \frac{1}{2} D_{nVV}. \quad (4.38)$$

Furthermore, one finds the relations:

$$Q_{fd} \;=\; 2Q_{fVS} \;-\; Q_{fVV} \;+\; \frac{1}{4} L_{fVV}^2, \quad (4.39)$$

$$Q_{nd} \;=\; 2Q_{nVS} \;-\; Q_{nVV} \;+\; \frac{1}{4} L_{nVV}^2. \quad (4.40)$$

4.2 PQχPT$^{\mathrm{TM}}$

We also extended the PQχPT to the case of two mass-degenerate twisted quarks[2] [88] (PQχPT$^{\mathrm{TM}}$). Here the additional complication arises that the twist angle in the sea-sector may in general be different from the one in the valence sector, because both κ_{val} and μ_{val} are free parameters. Taking this into account, the lattice term in the basis of a diagonal mass term reads

$$\rho(\omega_{\mathrm{sea}},\omega_{\mathrm{val}}) \;=\; \frac{2W_0 a c_{\mathrm{SW}}}{f_0^2}\exp[i\omega_{\mathrm{sea}}\tau_3^S]\exp[i\omega_{\mathrm{val}}\tau_3^V]\exp[i\omega_{\mathrm{val}}\tau_3^G], \tag{4.41}$$

where the Pauli matrices τ_i^X act in the sea- ($X=S$), valence- ($X=V$) or ghost-sector ($X=G$). Of course, $\omega_{\mathrm{ghost}}=\omega_{\mathrm{val}}$ is required to achieve quenching.

This shows once more the need for a local definition of the twist angle as has been given in Sec. 2.4.1. Naïvely one could propose one of the following strategies: (1) After determining the critical value of the hopping parameter (at a fixed value of μ_{sea}) one generates a set of configurations at that point and in the subsequent valence quark analysis just varies μ_{val}. With the assumption that κ_{crit} does not vary too much with μ being changed, one may argue that still $\omega_{\mathrm{val}}=\pi/2$ is valid. But a non-trivial critical line, corresponding to maximal twist, in the κ-μ plane is not the only caveat ruining this ansatz. Already from untwisted partially quenched simulations it is known that κ_{crit} need not necessary be the same in the sea- and the valence sector. We observed already in our analysis using PQχPT without twisted mass, that κ_{crit} defined as the extrapolation to vanishing pion mass differs in the two sectors and in the valence sector is dependent on κ_{sea}, e.g., Fig. 2 of [89] suggests such a dependence, too.[3] The latter argument also ruins the other (naïve) strategy (2): One may want to define the tangent of the twist angle just by the ratio of the (renormalized) twisted and untwisted masses (Eq. (2.4) using renormalized masses):

$$\tan\omega \;=\; \frac{Z_\mu\mu}{Z_m(\mu_\kappa-\mu_{\kappa,\mathrm{crit}})}.$$

Fixing μ circumvents the first problem not to know the function $\kappa_{\mathrm{crit}}(\mu)$. This strategy causes an inconsistency since $\kappa_{\mathrm{sea,\ crit}}\neq\kappa_{\mathrm{val,\ crit}}$ results in $\omega_{\mathrm{sea}}\neq\omega_{\mathrm{val}}$ even at $\kappa_{\mathrm{val}}=\kappa_{\mathrm{sea}}$. Using the PCAC-quark mass am_χ^{PCAC} to measure the untwisted component instead of $(\mu_\kappa-\mu_{\kappa,\mathrm{crit}})$ cures this caveat, but still the ratio of the renormalization factors has to be determined. To conclude the only viable ansatz is to use a local definition for the twist angle in the sea- and valence-sectors. This does not lead to inconsistencies like the afore mentioned one and also ensures the validity of automatic $\mathcal{O}(a)$-improvement at maximal twist, if a definition like Eqs. (2.78) or (2.80), (2.81) is applied.

We obtained the following expressions for the squared pion masses and pion decay constants up to terms of order a in a set-up of two twisted valence and two twisted sea quarks. The ratios and double ratios defined in the previous section can be easily deduced from these formulae.

[2] See also the discussion of lattice-χPT with a twisted mass term in Sec. 3.2.2.

[3] At least one expects the following to be true: $\lim_{\kappa_{\mathrm{sea}}\to\kappa_{\mathrm{sea,crit}}}\kappa_{\mathrm{val,crit}}(\kappa_{\mathrm{sea}}) = \kappa_{\mathrm{sea,crit}}$ and similar for the twist angles.

$$\begin{aligned}\frac{f_{SS}}{f_0} &= 1 - \frac{\chi_S + \rho\cos\omega_S}{16\pi^2}\log[\chi_S + \rho\cos\omega_S] \\ &\quad +4L_5\chi_S + 8L_4\chi_S + 4W_5\rho\cos\omega_S + 8W_4\rho\cos\omega_S, \qquad (4.42)\end{aligned}$$

$$\begin{aligned}\frac{f_{VV}}{f_0} &= 1 - \frac{1}{32\pi^2}(\chi_V + \chi_S + \rho\cos\omega_V + \rho\cos\omega_S)\log\left[\frac{\chi_V + \chi_S + \rho\cos\omega_V + \rho\cos\omega_S}{2}\right] \\ &\quad +4L_5\chi_V + 8L_4\chi_S + 4W_5\rho\cos\omega_V + 8W_4\rho\cos\omega_S, \qquad (4.43)\end{aligned}$$

$$\begin{aligned}\frac{f_{VS}}{f_0} &= 1 - \frac{1}{64\pi^2}\Bigg\{2(\chi_S + \rho\cos\omega_S)\log[\chi_S + \rho\cos\omega_S] \\ &\quad +(\chi_V + \chi_S + \rho\cos\omega_V + \rho\cos\omega_S)\log\left[\frac{\chi_V + \chi_S + \rho\cos\omega_V + \rho\cos\omega_S}{2}\right]\Bigg\} \\ &\quad +\frac{1}{128\pi^2}\Bigg\{\chi_V - \chi_S + \rho\cos\omega_V - \rho\cos\omega_S - (\chi_S + \rho\cos\omega_S)\log\left[\frac{\chi_V + \rho\cos\omega_V}{\chi_S + \rho\cos\omega_S}\right]\Bigg\} \\ &\quad +2L_5(\chi_V + \chi_S) + 8L_4\chi_S + 2W_5(\rho\cos\omega_V + \rho\cos\omega_S) + 8W_4\rho\cos\omega_S, \qquad (4.44)\end{aligned}$$

$$\begin{aligned}\frac{m_{SS}^2}{f_0^2} &= \chi_S + \rho\cos\omega_S + \frac{(\chi_S + \rho\cos\omega_S)^2}{32\pi^2}\log[\chi_S + \rho\cos\omega_S] \\ &\quad +16(2L_6 - L_4)\chi_S^2 + 8(2L_8 - L_5)\chi_S^2 + 16(W_6 - L_4)\chi_S\rho\cos\omega_S \\ &\quad +16(W_6 - W_4)\chi_S\rho\cos\omega_S + 8(2W_8 - W_5 - L_5)\chi_S\rho\cos\omega_S, \qquad (4.45)\end{aligned}$$

$$\begin{aligned}\frac{m_{VV}^2}{f_0^2} &= \chi_V + \rho\cos\omega_V + \frac{\chi_V + \rho\cos\omega_V}{32\pi^2}\Bigg\{\chi_V - \chi_S + \rho\cos\omega_V - \rho\cos\omega_S \\ &\quad +(2\chi_V - \chi_S + 2\rho\cos\omega_V - \rho\cos\omega_S)\log[\chi_V + \rho\cos\omega_V]\Bigg\} \\ &\quad +16(2L_6 - L_4)\chi_S\chi_V + 8(2L_8 - L_5)\chi_V^2 + 16(W_6 - L_4)\chi_S\rho\cos\omega_V \\ &\quad +16(W_6 - W_4)\chi_V\rho\cos\omega_S + 8(2W_8 - W_5 - L_5)\chi_V\rho\cos\omega_V, \qquad (4.46)\end{aligned}$$

$$\begin{aligned}\frac{m_{VS}^2}{f_0^2} &= \frac{1}{2}(\chi_V + \chi_S + \rho\cos\omega_V + \rho\cos\omega_S) \\ &\quad \frac{1}{64\pi^2}(\chi_V + \chi_S + \rho\cos\omega_V + \rho\cos\omega_S)(\chi_V + \rho\cos\omega_V)\log[\chi_V + \rho\cos\omega_V] \\ &\quad +8(2L_6 - L_4)\chi_S(\chi_V + \chi_S) + 2(2L_8 - L_5)(\chi_V + \chi_S)^2 \\ &\quad +8(W_6 - L_4)\chi_S(\rho\cos\omega_V + \rho\cos\omega_S) + 8(W_6 - W_4)(\chi_V + \chi_S)\rho\cos\omega_S \\ &\quad +2(2W_8 - W_5 - L_5)(\chi_V + \chi_S)(\rho\cos\omega_V + \rho\cos\omega_S). \qquad (4.47)\end{aligned}$$

(Conventions like fixed in the previous section.)

These expressions also show up the $\mathcal{O}(a)$ improvement for $\omega_V = \omega_S = \frac{\pi}{2}$, since every lattice artifact term ($\propto \rho$) contains a factor of $\cos\omega_V$ or $\cos\omega_S$. We remark that this implies a non-trivial tuning problem if in a partially quenched analysis one aims for full $\mathcal{O}(a)$ improvement in all the valence- and sea-quantities. The reason is that one will have to adjust both parameters $\kappa_{\rm val}$, $\mu_{\rm val}$ to values resulting in maximal twist. Of course, even if this tuning is not exact, already in the vicinity of maximal twist the lattice artifacts are suppressed.

Chapter 5

Numerical simulations

After we shortly discussed the general ingredients for putting quantum fields and especially QCD on a lattice in the first chapter and presented in detail (Chapter 2) the interesting properties of the twisted lattice action ($\mathrm{QCD}^{\mathrm{TM}}$), we will now turn to the application of these. Results obtained from numerical simulations will have to be interpreted by chiral effective theories (χPT and its lattice versions, Chapters 3 and 4). The question about the phase structure of lattice QCD near zero quark mass will also be elaborated, as was already announced (Sec. 3.3).

First we want to give some general remarks, how the configurations for the measurements are generated, i.e., how the configuration space is sampled by the *updating algorithms*. Details on the implementation of those algorithms and the measurements into computer code will be postponed to the appendix (App. C). Here we will present our results from a set of simulations with untwisted Wilson-quarks. We successfully tested the applicability of PQχPT and extracted some linear combination of LECs therefrom. The last part describes extensive studies of the $\mathrm{QCD}^{\mathrm{TM}}$ action with our main objectives on the possibility to use it for simulating light quark flavors and determine the phase structure of lattice QCD.

5.1 Updating algorithms

Measuring an observable in (lattice) field theory always follows the prescription Eq. (1.11). In principle one could consider every possible configuration. Since this is impractical, the aim of updating algorithms is to generate a set of configurations which sample this distribution stochastically. This is done by interpreting e^{-S} as the Boltzmann factor like in statistical mechanics. It is clear that only a small number of configurations, which possess a large Boltzmann factor, will substantially contribute.

The updating algorithms should fulfill the following two conditions:

- **Detailed balance:**

$$P([\phi] \leftarrow [\phi'])e^{-S[\phi']} \;=\; P([\phi'] \leftarrow [\phi])e^{-S[\phi]}, \tag{5.1}$$

  where the probability for going from a configuration $[\phi]$ to $[\phi']$ is given by $P([\phi'] \leftarrow [\phi])$. This condition is not necessary but sufficient to show that if one starts from a reasonable configuration, after a number of updating steps one samples the canonical distribution corresponding to the Boltzmann factor e^{-S}.

- **(Strong) Ergodicity:** This is the requirement, that from a given configuration any other configuration can be reached,

$$\forall [\phi], [\phi'] : \; P([\phi'] \leftarrow [\phi]) \; > \; 0. \tag{5.2}$$

  If every part of the updating algorithm respects this condition, one speaks of strong ergodicity. But in the case that different algorithms are combined, it is enough if this combination fulfills Eq. (5.2). This is called just ergodicity.

In the remainder of this section, we will focus on different commonly used update algorithms and concentrate on how to apply these to the fermion part of the action.

5.1.1 Metropolis, Heatbath, Overrelaxation

In case of the Metropolis algorithm [90, 91] the probability for going from one configuration $[\phi]$ to $[\phi']$ is given by

$$P([\phi'] \leftarrow [\phi]) \; \propto \; F\left(\frac{e^{-S[\phi']}}{e^{-S[\phi]}}\right). \tag{5.3}$$

Usually for F one chooses

$$F_1(x) \; = \; \min(1, x) \tag{5.4}$$

or

$$F_2(x) \; = \; \frac{x}{1+x}. \tag{5.5}$$

In general any function that maps $[0, \infty]$ to $[0, 1]$ and fulfills

$$F(x) \; = \; x \, F\left(\frac{1}{x}\right) \tag{5.6}$$

is a legitimate choice for this algorithm. If F_1 is taken into account, every new configuration which has a higher Boltzmann factor (lower action) is accepted, while otherwise just with the probability $e^{-(S[\phi']-S[\phi])}$. In case of F_2 every new generated configuration might be rejected. The advantage of the choice F_1 therefore is a higher acceptance rate.

Practically this algorithm is implemented as follows: first a randomly chosen configuration is generated and afterwards accepted or rejected according to the above procedure. While in principle one could really generate an independent configuration in every step, most times just a part of the field variables, e.g., the gauge link at one particular lattice site, is changed randomly and the rest is kept fixed. By combining many such steps, ergodicity can be achieved.

In [92] a generalization of this algorithm has been introduced, which allows for using any probability distribution P_C and corrects the acceptance via

$$P_A([\phi'] \leftarrow [\phi]) \; \propto \; \min\left(1, \frac{P_C([\phi] \leftarrow [\phi'])e^{-S[\phi']}}{P_C([\phi'] \leftarrow [\phi])e^{-S[\phi]}}\right). \tag{5.7}$$

The total transition probability is then given by $P = P_A P_C$.

A special variant of the Metropolis algorithm is the overrelaxation algorithm [93, 94, 95, 96]: the configurations are changed in a way, which leaves the action invariant and ensures

$$[\phi] \overset{\text{update}}{\longrightarrow} [\phi'] \overset{\text{update}}{\longrightarrow} [\phi] \tag{5.8}$$

in each single update step. Consequently one always has $P_A = 1$, but because the action is left unchanged this algorithm is not ergodic. But still it can be combined with other algorithms to reach ergodicity.

The heatbath algorithm [15, 97] is another variant of the Metropolis algorithm. Here, one tries locally, i.e., for one given lattice site, to sample as best as possible the required equilibrium distribution.

For applying the mentioned algorithms to the gauge links we refer to [98]. For the (pseudo-) fermion fields details will be discussed in the remainder of this section.

5.1.2 Boson algorithm: TSMB

After performing the Grassmann-integration over the fermion fields the lattice action reads

$$S_{\text{eff}}[U] \;=\; S_g[U] \;-\; \log\det \boldsymbol{Q}[U]. \tag{5.9}$$

The so called *quenched approximation* neglects the fermionic contribution in the update-procedure by setting $\det \boldsymbol{Q} = 1$ and includes this part only in the measurements. In the language of the previously discussed PQχPT (Chapter 4) that means one only considers valence quarks without any sea quark contribution. This approach is affected by uncontrollable systematic errors but, on the other hand, is computationally very cheap.

Multi-Boson algorithms

Here we want to focus on the Multi-Boson approach to include dynamical fermions. Another method would be, e.g., the Hybrid Monte Carlo (HMC)-algorithm [99]. First we will concentrate on untwisted QCD and postpone QCD$^{\text{TM}}$. If one deals with N_f flavors of mass-degenerate quarks, the fermion determinant is block diagonal, which allows one to write

$$|\det \boldsymbol{Q}| \;=\; |\det Q|^{N_f}, \tag{5.10}$$

where Q is the matrix for $N_f = 1$. Now this determinant can be represented by bosonic fields $\phi^\dagger, \phi$, often referred to as pseudo-fermion fields, via a bosonization of this matrix:

$$\det(Q^\dagger Q) \;=\; \int \mathcal{D}[\phi^\dagger, \phi]\, \exp\left(-\sum_{xy} \phi_y^\dagger \left[Q^\dagger Q\right]^{-1}_{yx} \phi_x \right). \tag{5.11}$$

Because of $Q^\dagger = \gamma_5 Q \gamma_5$ one can also use the Hermitian version of the fermion matrix $\tilde{Q} \equiv \gamma_5 Q = \tilde{Q}^\dagger$ instead of $Q^\dagger Q$:

$$\tilde{Q}^2 \;=\; \gamma_5 Q \gamma_5 Q \;=\; Q^\dagger Q. \tag{5.12}$$

But still the numerical effort to compute the inverse of the squared Hermitian fermion matrix as needed is too costly. As a solution Lüscher [100] proposed to approximate the matrix inversion by a polynomial $P^{(1)}_{n_1}$ of degree n_1. Requiring that this polynomial fulfills

$$\lim_{n_1 \to \infty} P^{(1)}_{n_1}(x) \;=\; x^{-\frac{N_f}{2}}, \quad \forall x \in [\epsilon, \lambda] \tag{5.13}$$

in the range of eigenvalues $[\epsilon, \lambda]$ of the considered matrix, one can finally write

$$|\det Q|^{N_f} = \frac{1}{\det(\tilde{Q}^2)^{-\frac{N_f}{2}}} \simeq \frac{1}{\det P_{n_1}^{(1)}(\tilde{Q}^2)} \tag{5.14}$$

$$= \int \mathcal{D}[\phi^\dagger, \phi] \exp\left(-\sum_{xy} \phi_y^\dagger P_{n_1}^{(1)}(\tilde{Q}^2)_{yx} \phi_x\right) \tag{5.15}$$

$$= \int \mathcal{D}[\phi^\dagger, \phi] \exp\left(-\sum_{xy} \sum_{i=1}^{n_1} {\phi_y^{(i)}}^\dagger \left[(\tilde{Q} - \rho_i^*)(\tilde{Q} - \rho_i)\right] \phi_x^{(i)}\right). \tag{5.16}$$

In the last step it is assumed that the roots z_i always appear in complex conjugate pairs:

$$P_{n_1}^{(1)}(x^2) = c_0 \prod_{i=1}^{n_1}(x^2 - z_i) = r_0 \prod_{i=1}^{n_1}(x - \rho_i^*)(x - \rho_i). \tag{5.17}$$

In principle with this formulation at hand, one is able to run dynamical simulations [101]. The order n_1 of the polynomial approximation mainly determines the cost and memory requirements of such a simulation, because one has to deal with a pseudo-fermion field for each order of the polynom. Since we are interested in simulating light quark masses, as near to the physical up- and down-quark masses as possible, this approach will not be sufficient because of the following: the condition number λ/ϵ, i.e., the ratio of the highest (λ) to the lowest (ϵ) eigenvalue of the fermion matrix, is related to the pion mass in lattice units via

$$\sqrt{\frac{\lambda}{\epsilon}} \propto (am_\pi)^{-1}, \tag{5.18}$$

and the quadratically averaged error of the polynomial approximation $P_{n_1}^{(1)}$ is estimated by

$$\delta_{n_1} \simeq \exp\left(-Cn_1\sqrt{\frac{\epsilon}{\lambda}}\right). \tag{5.19}$$

Therefore, if δ_{n_1} is kept fixed: $n_1 \propto (am_\pi)^{-1}$. One has to find a way to reduce n_1 in dynamical simulations, in order to make them feasible. Apart from the computational limitations, like memory usage and precision of calculated coefficients and roots, also long autocorrelations induced by large n_1 are an argument against the simple use of this multi-boson formulation.

Nevertheless, it provides the fundamental building block for the TSMB-algorithm. So we will now show how to use it for QCD$^{\mathrm{TM}}$, too. All the following considerations are then valid for either QCD or QCD$^{\mathrm{TM}}$. A straightforward implementation of the fermion action with a twisted mass term (mass-degenerate or mass-non-degenerate) would be to double the bosonic fields, i.e., adding explicitly a flavor index, and apply the multiplication due to the changed fermion matrix. Another ansatz follows from the combination of Eq. (2.11) with the polynomial approximation for the inverse of Q^2, which allows one to stay with an (already existing) untwisted update code and just redefine the polynomials:

$$\begin{aligned} |\det Q_\chi^{\mathrm{TM}}| &= |\det(D^\dagger D + \mu^2)| \\ &\simeq \frac{1}{\det P_{n_1}^{(1)\mathrm{TM}}(D^\dagger D)}, \\ \lim_{n_1\to\infty} P_{n_1}^{(1)\mathrm{TM}}(x) &= (x + \mu^2)^{-1}, \quad \forall x \in [\epsilon, \lambda]. \end{aligned}$$

We did not follow this line but used the straightforward one, since this will also allow for using even-odd preconditioning to speed up the algorithm (see below). One should keep in mind that in this case the fermion matrix always describes a doublet of quark fields, for that reason N_f as defined upwards now means the number of doublets or half the number of fermions. For simulating one doublet, one will have to use a polynomial $P^{(\frac{1}{2})}_{(n_1)}(x)$ approximating

$$\lim_{n_1\to\infty} P^{(\frac{1}{2})}_{(n_1)}(x) \;\simeq\; x^{-\frac{1}{2}}, \quad \forall x \in [\epsilon, \lambda]. \tag{5.20}$$

Considering the numerical costs, one application of the fermion matrix is twice as costly compared to the untwisted case. On the other hand, the exponent for the function to be approximated by the polynomial gets divided by two, allowing for lower polynomial degrees. In total the numerical costs will stay roughly constant (cf. Sec. 5.3.2, Tab. 5.11).

Two-Step Multi-Boson algorithm

As argued in the preceding section, one has to try to keep n_1 as low as possible, but still the error of the approximation should be small and under control. This can be achieved by using the Two-Step Multi-Boson (TSMB) algorithm [102]. Here one follows the multi-boson approach with a reduced n_1 and corrects for this poor approximation by a global correction step. The price one has to pay is a lower acceptance rate, but it is still possible to aim for a rate of 40%–60%. It is important to note that this correction ensures the quality of the final result. The global correction can be realized by introducing a second polynomial $P^{(2)}_{n_2}$ of degree $n_2 > n_1$ so that the inverse is now approximated in two steps:

$$\lim_{n_2\to\infty} P^{(1)}_{n_1}(x) P^{(2)}_{n_2}(x) \;=\; x^{-\frac{N_f}{2}}, \quad \forall x \in [\epsilon, \lambda]. \tag{5.21}$$

While n_1 can be fixed at some low value, it is possible to achieve the desired quality of the approximation by increasing n_2. The multi-boson representation is only used for $P^{(1)}_{n_1}$. The pseudo-fermion fields are updated by local algorithms, e.g., heatbath or overrelaxation, independently from the gauge fields. After some local gauge field updates, a global correction step is performed taking $P^{(2)}_{n_2}$ into account: one ensures via an accept-reject decision, that the distribution of the gauge fields still corresponds to

$$|\det(Q[U])|^{N_f} \;\simeq\; \frac{1}{\det P^{(1)}_{n_1}(\tilde{Q}^2[U]) \det P^{(2)}_{n_2}(\tilde{Q}^2[U])}. \tag{5.22}$$

Using a noisy correction, first one has to generate a random vector η according to the normalized Gaussian distribution

$$d\rho(\eta) \;=\; \frac{\exp(-\eta^\dagger P^{(2)}_{n_2}(\tilde{Q}^2)\eta)}{\int \mathcal{D}[\eta^\dagger, \eta] \exp(-\eta^\dagger P^{(2)}_{n_2}(\tilde{Q}^2)\eta)} \tag{5.23}$$

and then accept the (global) change of the gauge fields $[U] \to [U']$ with the probability

$$P_{NC} \;=\; \min\left(1, \exp\left[-\eta^\dagger \left(P^{(2)}_{n_2}(\tilde{Q}[U']^2) - P^{(2)}_{n_2}(\tilde{Q}[U]^2)\right)\eta\right]\right). \tag{5.24}$$

The needed noisy estimator η is easily obtained from a simple Gaussian distributed vector η'

$$d\rho(\eta') \;=\; \frac{\exp(-\eta'^{\dagger}\eta')}{\int \mathcal{D}[\eta'^{\dagger},\eta']\exp(-\eta'^{\dagger}\eta')} \tag{5.25}$$

via

$$\eta \;=\; P^{(2)}_{n_2}(\tilde{Q}^2)^{-\frac{1}{2}}\,\eta'. \tag{5.26}$$

In practice one gets the needed inverse square-root through a third polynomial

$$\lim_{n_3\to\infty} P^{(3)}_{n_3}(x) \;=\; P^{(2)}_{n_2}(x)^{-\frac{1}{2}}, \quad \forall x\in[\epsilon',\lambda],\ \epsilon'\le\epsilon. \tag{5.27}$$

The reason for choosing a smaller lower bound is not to introduce additional uncertainties due to this last approximation.

The polynomials are chosen to be least-square optimized and are conveniently determined in a recurrence scheme, cf. [103] for details, and also [104] for a recent numerical faster approach.

In order to test the quality of the approximation, in principle, one has to perform the limit $n_2\to\infty$. Another possibility is to calculate a reweighting factor R to check, if n_2 was chosen properly. One can use the exact eigenvalues λ_i of $\tilde{Q}^2$:

$$R[U] \;=\; \prod_i P^{(1)}_{n_1}(\lambda_i)P^{(2)}_{n_2}(\lambda_i)\lambda_i^{\frac{N_f}{2}}, \tag{5.28}$$

or introduce a fourth polynom $P^{(4)}_{n_4}(x), n_4>n_2$:

$$\lim_{n_4\to\infty} P^{(1)}_{n_1}(x)P^{(2)}_{n_2}(x)P^{(4)}_{n_4}(x) \;=\; x^{-\frac{N_f}{2}}, \quad \forall x\in[\epsilon,\lambda] \tag{5.29}$$

and perform a stochastically determination of the reweighting factor

$$R[U] \;=\; \frac{1}{\det P^{(4)}_{n_4}(\tilde{Q}^2)} \;=\; \frac{\int \mathcal{D}[\eta^{\dagger},\eta]\exp(-\eta^{\dagger}P^{(4)}_{n_4}(\tilde{Q}^2)\eta)}{\int \mathcal{D}[\eta^{\dagger},\eta]\exp(-\eta^{\dagger}\eta)}. \tag{5.30}$$

In practice a mixture of both is used: a given number of smallest eigenvalues is calculated exactly and the sub-space of these is projected out for the following stochastic calculation. In the case that these $R[U]$ deviate substantially from one, they should be included in the following analysis of the configurations by defining an expectation value of some quantity $\mathcal{O}$ as

$$\langle\mathcal{O}\rangle \;=\; \frac{\langle R[U]\mathcal{O}\rangle}{\langle R[U]\rangle}. \tag{5.31}$$

The remainder of this section is devoted to the discussion of some improvements to speed up the algorithms: determinant breakup, preconditioning, and the Multi-Step Multi-Boson algorithm. This is followed by a brief discussion on the different boson update procedures and a remark on how to simulate different (mass non-degenerate) quark flavors.

Determinant breakup

The basic simple idea is to use the factorization of the fermionic determinant in several factors, also allowing for some "fractional" number of flavors:

$$\left|\det(\tilde{Q})\right|^{N_f} \;=\; \left[\left|\det(\tilde{Q}^2)\right|^{\frac{N_f}{2n_b}}\right]^{n_b}, \tag{5.32}$$

where n_b is called the breakup factor. This factorization is assumed to lower the autocorrelation, because more noisy estimators in the correction step are used and in this way the inverse of $\det P_{n_2}^{(2)}$ is taken into account more precisely. Another benefit is, because now the polynomial approximation will be split into n_b pieces, one can use smaller polynomial orders in the single polynoms, which is advantageous as long as the production of the recurrence coefficients takes a substantial amount of CPU-time. Of course, the numerical cost (neglecting autocorrelations) in the update should be roughly constant, because now n_b copies of a polynomial of smaller degree are used. In our simulations we used n_b up to a value of four.

Preconditioning of the fermion matrix

The computational costs are determined by the condition number of the fermion matrix. A decrease is achieved, if one uses a fermion matrix which results in the same determinant but having a smaller condition number. One may use the *even-odd preconditioned* fermion matrix $\bar{Q}$ in the untwisted case:

$$\bar{Q} \;=\; \mathbb{1} \;-\; \kappa^2 \begin{pmatrix} 0 & 0 \\ 0 & D_{oe}D_{eo} \end{pmatrix}. \tag{5.33}$$

The matrix is written in the subspaces of even and odd lattice sites. The operators D are defined by the representation of the fermion matrix:

$$Q \;=\; \mathbb{1} \;-\; \kappa \begin{pmatrix} 0 & D_{oe} \\ D_{eo} & 0 \end{pmatrix}. \tag{5.34}$$

The eigenvalues $\bar{\lambda}$ of $\bar{Q}$ are either 1 (even subspace) or related to the eigenvalues λ of Q [19]:

$$\bar{\lambda} \;=\; \lambda(2-\lambda), \tag{5.35}$$

which results in a factor of approximately two larger eigenvalues for $\lambda \ll 1$.

Even-odd preconditioning can also be used in conjunction with QCD$^{\mathrm{TM}}$, if implemented with independent boson fields for each flavor. We will demonstrate the procedure for the mass degenerate case ($\mu_\Delta = 0$), the generalization to $\mu_\Delta \neq 0$ is straightforward and modified formulae will be presented in App. C. Decomposing the Hermitian fermion matrix in the even and odd subspaces of the lattice sites

$$\tilde{Q}_\chi \;=\; \gamma_5\tau_1 Q_\chi \;=\; \begin{pmatrix} \mu_\kappa\gamma_5\tau_1 + \mu\tau_2 & -\frac{1}{2}\gamma_5\tau_1 D_{eo} \\ -\frac{1}{2}\gamma_5\tau_1 D_{oe} & \mu_\kappa\gamma_5\tau_1 + \mu\tau_2 \end{pmatrix}, \tag{5.36}$$

we can rewrite it as the following product:

$$\begin{aligned}\tilde{Q}_\chi &= \begin{pmatrix} \mu_\kappa\gamma_5\tau_1+\mu\tau_2 & 0 \\ 0 & \mu_\kappa\gamma_5\tau_1+\mu\tau_2 \end{pmatrix} \times \\ &\times \begin{pmatrix} 1 & 0 \\ -\frac{1}{2}t_5 D_{oe} & 1 \end{pmatrix} \begin{pmatrix} 1 & 0 \\ 0 & 1-\frac{1}{4}t_5 D_{oe} t_5 D_{eo} \end{pmatrix} \begin{pmatrix} 1 & -\frac{1}{2}t_5 D_{eo} \\ 0 & 1 \end{pmatrix}, \end{aligned} \tag{5.37}$$

with

$$t_5 \equiv \frac{1}{\mu_\kappa\gamma_5\tau_1+\mu\tau_2}\gamma_5\tau_1 = \frac{\mu_\kappa - i\mu\gamma_5\tau_3}{\mu_\kappa^2+\mu^2}. \tag{5.38}$$

The inverse of all these factors is trivial, besides the third factor, which is expected[1] to have a smaller condition number compared to $\tilde{Q}_\chi$. We end up with

$$\begin{aligned}\det(\tilde{Q}_\chi) &= \det \begin{pmatrix} \mu_\kappa\gamma_5\tau_1+\mu\tau_2 & 0 \\ 0 & \mu_\kappa\gamma_5\tau_1+\mu\tau_2-\frac{1}{4}\gamma_5\tau_1 D_{oe} t_5 D_{eo} \end{pmatrix} \\ &= \det_e(\mu_\kappa\gamma_5\tau_1+\mu\tau_2)\ \det_o(\mu_\kappa\gamma_5\tau_1+\mu\tau_2-\frac{1}{4}\gamma_5\tau_1 D_{oe} t_5 D_{eo}), \end{aligned} \tag{5.39}$$

for the fermion determinant, since the determinant of the above triangular matrices is equal to one. Here $\det_e$ and $\det_o$ denote the determinant in the even and odd subspaces, respectively. The first factor does not depend on the gauge fields at all, and for that reason can be omitted in the update-procedure. The second factor now defines the Hermitian preconditioned fermion matrix (on odd sites only):

$$\bar{Q}_\chi \equiv \mu_\kappa\gamma_5\tau_1+\mu\tau_2-\frac{1}{4}\gamma_5\tau_1 D_{oe} t_5 D_{eo} = \bar{Q}_\chi^\dagger. \tag{5.40}$$

Not only the update code benefits from preconditioning the fermion matrix but also the measurement of the correlators requiring the inverse fermion matrix. We refer to the appendix for details (App. C.1).

Multi-Step Multi-Boson algorithm

The idea of the TSMB-algorithm can be extended to Multi-Step Multi-Boson algorithms (MSMB) by introducing further correction steps [105]. This has the advantage that again the first global correction, done with polynomials $P^{(2)}_{n_2}, P^{(3)}_{n_3}$, can be less precise than before. For each step $m = 2, 3, \ldots$ one introduces a polynomial $P^{(2m)}_{n_{2m}}$

$$\lim_{n_{2m}\to\infty} P^{(1)}_{n_1}(x)\left(\prod_{i=1}^{m} P^{(2i)}_{n_{2i}}(x)\right) = x^{-\frac{N_f}{2}}, \quad \forall x \in [\epsilon, \lambda] \tag{5.41}$$

and the roots

$$\lim_{n_{2m+1}\to\infty} P^{(2m+1)}_{n_{2m+1}}(x) = P^{(2m)}_{n_{2m}}(x)^{-\frac{1}{2}}, \quad \forall x \in [\epsilon', \lambda],\ \epsilon' \le \epsilon, \tag{5.42}$$

with $n_1 < n_2 < \ldots < n_{2m} < n_{2m+1}$.

Now one performs nested sweeps of length N_m after which a global correction with the polynomial $P^{(2m)}_{n_{2m}}$ is done. In case of non-acceptance by the correction with $P^{(2m)}_{n_{2m}}$ the

[1] A relation like Eq. (5.35) could not be found until now, but we checked this numerically.

fields have to be replaced with the stored last accepted configuration[2]. Here last accepted means accepted by a correction done with the same polynomial. This procedure requires to keep m different old field configurations. We illustrate the case of $m = 2$:

$$\text{start} \underbrace{\underbrace{\rightarrow \ldots \rightarrow}_{N_1\text{steps}} P_{(2)} \longrightarrow \ldots \longrightarrow \underbrace{\rightarrow \ldots \rightarrow}_{N_1\text{steps}} P^{(2)}}_{N_2\text{steps}} \longrightarrow P^{(4)}$$

Still a final reweighting with a polynom $P^{(2m+2)}_{n_{2m+2}}$ can be done.

Update procedure

By decomposing the roots in Eq. (5.17) further in their real and imaginary parts μ_i and ν_i, respectively, one arrives at a representation of the polynomials ($z_j = (\mu_j + i\nu_j)^2$, $\rho_j = \mu_j + i\nu_j$)

$$P^{(1)}_{n_1}(x^2) \;=\; r_0 \prod_{i=1}^{n_1} \Big((x \pm \mu_i)^2 + \nu_i^2 \Big). \tag{5.43}$$

This is better suited when local boson updates are performed. The bosonic part of the action should be written as (P_o projects on the subspace of odd lattice sites)

$$\begin{aligned} S^{(n_1)}[U, \phi, \phi^\dagger] &= \sum_{i=1}^{n_1} \phi^{(i)\dagger} \Big(\tilde{Q} - P_o \rho_i^* \Big) \Big(\tilde{Q} - P_o \rho_i \Big) \phi^{(i)} && (5.44) \\ &= \sum_{i=1}^{n_1} \phi^{(i)\dagger} \Big(\tilde{Q}^2 - \rho_i^* P_o \tilde{Q} - \rho_i \tilde{Q} P_o - P_o |\rho_i|^2 \Big) \phi^{(i)} && (5.45) \\ &= \sum_x \sum_{i=1}^{n_1} \Big(\phi_x^{(i)\dagger} A^{(i)} \phi_x^{(i)} \;+\; [\phi_x^{(i)\dagger} b_x^{(i)} + h.c.] \Big) && (5.46) \end{aligned}$$

if the even-odd preconditioned fermion matrix is used [106]. In the last step the action is decomposed into a local part A and a part b, which contains next-to-nearest-neighbor interactions. Here A depends on the site parity and can be given in terms of μ_i, ν_i plus κ or μ_κ, μ, and μ_Δ. Also b is site-depended, but also depends on the gauge-field and the boson fields at the neighboring sites, cf. [98] for details on the untwisted case. In the twisted case, the expressions become also flavor depended, we provide them in App. C.1.

With these expressions at hand a local bosonic overrelaxation update consists of replacing the boson fields according to

$$\phi_x^{(i)} \;\leftarrow\; -\phi_x^{(i)} \;-\; 2 {A^{(i)}}^{-1} b_x^{(i)}, \tag{5.47}$$

while for a local bosonic heatbath with a Gaussian random spinor χ one has to follow the prescription

$$\phi_x^{(i)} \;\leftarrow\; {A^{(i)}}^{-\frac{1}{2}} \chi \;-\; {A^{(i)}}^{-1} b_x^{(i)}. \tag{5.48}$$

Because these updates are done "order by order" in n_1, one is allowed to organize the update-sequence of local boson updates in a memory efficient way. If the lattice sizes

[2] One may also update the boson fields between two applications of $P^{(2m)}_{n_{2m}}$ and therefore will have to store an old configuration of these, too.

and/or n_1 are getting too large, so that it is not possible to keep the whole boson fields simultaneously in the memory, it is possible to keep only an active fraction (i.e., the fraction corresponding to polynomial orders $n_s \leq n_1 \leq n_e$) of it. The rest is stored in an auxiliary file on hard-disk. To reduce read-write access of these files, one can do a sequence of local boson overrelaxation and heatbath updates on one of these sets before continuing on the next set.

Writing the bosonic action in the form of Eq. (5.44) further allows to create new boson fields in a global step starting from a set of Gaussian random spinors $\chi^{(i)}$:

$$\phi_x^{(i)} \leftarrow \sum_y (\tilde{Q} - P_o \rho_i)^{-1}_{xy} \chi_y^{(i)}. \tag{5.49}$$

This is called a *global heatbath* step.

Different flavors, odd number of flavors

If one wants to simulate N_f untwisted[3] quarks of flavor $f = 1, \ldots, F$, the fermion determinant can be written as

$$|\det \boldsymbol{Q}| = \prod_{f=1}^{F} |\det \tilde{Q}_f^2|^{\frac{N_f}{2}}. \tag{5.50}$$

The multi-boson and TSMB or MSMB procedure is applicable to the different fermion matrices as before.

In the case of an odd number of untwisted fermions of one flavor, one has to remark that the possibly negative sign of the determinant is not included. One way to correct for the sign is via the reweighting factor. The proper sign can be calculated from the zero-level crossings of the spectral flow of the smallest eigenvalues. Since in this work we will only deal with an even number of fermions, for details we refer to the literature [98, 107, 19]. In the twisted case, single flavors are not possible by construction. One may either combine twisted doublets with single untwisted flavors, or use the mass non-degenerate formulation and choose the mass splitting in such a way, that one field gets a mass of the order of the cut-off and therefore becomes irrelevant.

5.2 LECs from untwisted $N_f = 2$ simulations

The possibility of extracting LECs from partially quenched lattice simulations has been presented in Chapter 4. We also discussed both the need of χPT for guiding the extrapolation to realistic quark masses as well as lattice QCD allowing for a first principle approach to test this theory and to determine the LECs in this way directly from the QCD-Lagrangian.

We performed a series of simulations with $N_f = 2$ flavors of mass-degenerate quarks. These results were published by the qq+q Collaboration in [84, 108, 109, 110, 111]. We used the Wilson plaquette gauge action with untwisted dynamical Wilson fermions ($r = 1$). The lattice sizes were $L^3 \times T = 16^4$ and $16^3 \times 32$. Details on the parameters for the different runs can be found in Tab. 5.1. These runs were performed using the TSMB-algorithm

[3] The same holds for N_f different doublets in case of QCD$^{\text{TM}}$.

run	I	II	III
$L^3 \times T$	$16^3 \times 16$	$16^3 \times 16$	$16^3 \times 32$
β	4.68	5.10	5.10
κ	0.195	0.1760, 0.1765, 0.1770	0.1760, 0.1765, 0.1768, 0.1770
a/fm	≈ 0.28	0.189(5)	0.195(4)
aL/fm	≈ 4.5	≈ 3.0	≈ 3.0

Table 5.1: *Parameters for the simulations done by the qq+q Collaboration. Also the lattice spacing determined from the Sommer scale is quoted here.*

described in Sec. 5.1.2, Tab. 5.2 reports details on its implementation. We also include a study applying the DBW2 action for the gauge part of the action, Sec. 5.2.3. Originally, this was done to examine the scaling properties of this particular gauge action, which we used extensively in Sec. 5.3.2. But we decided to put it in this context, since the method is similar to the sea quark analysis presented in this part.

The first run (I) was an exploratory study at a rather coarse lattice with only one value for the dynamical quark mass. See also Tab. 5.1 for the values of the lattice spacing determined from the Sommer scale parameter r_0/a. The runs at $\beta = 5.10$, which resulted in a finer lattice spacing of $a \approx 0.19$ fm, were done at $T = 16$ and 32. The larger time-extent in run III was chosen in order to have a better determination of masses and decay constants, since the range of fitting the asymptotic behavior of the correlators is larger. We observed this effect in the measured quantities (Tab. 5.3): while for r_0/a it was only 2%–5%, for the pion mass a change of 3% at the lowest κ-value (highest pion mass) and up to 16% at the highest κ-value (lowest pion mass) occurred. The quark mass extracted via the PCAC-relation shows the same qualitative behavior with a change in the range from 5% to 28%.

The lightest pion mass in MeV can be calculated using $r_0 \approx 0.49$ fm: one gets roughly 370 MeV in runs I and III, 460 MeV in run II. If one uses M_{r_0} to estimate the quark mass, Eq.(1.46), the lightest quark mass is $\approx \frac{1}{4} m_{\text{strange}}$ in run I and III, and $\approx \frac{1}{3} m_{\text{strange}}$ in run II. Finite volume effects are expected to be small (cf. the discussion in Sec. 3.2): taking the results from [57] or [60, 61], we read off, e.g., from Fig. 2 in [61] for our lightest pion mass of 370 MeV, with $aL \approx 3.0$ fm a relative mass shift for the pion of less than 1%. For that reason we will not concentrate much more on this.

5.2.1 Numerical cost

When one asks for the numerical cost to obtain a certain quantity on the lattice, what counts is the amount of floating-point operations (FLOP), which are needed to produce a statistically independent configuration. In case of the TSMB-algorithm as implemented in our routines, one gets the number of matrix-vector multiplications (MVMs) N_{MVM}, needed for an update sequence consisting of N_ϕ local boson updates, N_U local gauge updates, N_C global correction steps, and a global heatbath done with frequency F_G using an average number of I_G MVMs, from

$$N_{\text{MVM}}/\text{cycle} \;\approx\; 6(n_b n_1 N_\phi \;+\; N_U) \;+\; 2n_b(n_2 + n_3)N_C \;+\; F_G I_G. \tag{5.51}$$

run	κ	N_f	n_1	n_2	n_3	$[\epsilon, \lambda]$
I	0.1950	1×2	104	860	1100	$[3.60 \cdot 10^{-4}, 3.6]$
II	0.1760	2×1	40	210	220	$[4.50 \cdot 10^{-4}, 3.0]$
	0.1765	2×1	40–44	280	260–340	$[2.50 \cdot 10^{-4}, 3.0]$
	0.1770	2×1	54	690	840	$[3.75 \cdot 10^{-5}, 3.0]$
III	0.1760	$4 \times 1/2$	30	220	280	$[5.25 \cdot 10^{-4}, 3.0]$
	0.1765	2×1	46	320	400	$[2.25 \cdot 10^{-4}, 3.0]$
		$4 \times 1/2$	32	280	380	$[2.25 \cdot 10^{-4}, 3.0]$
	0.1768	$4 \times 1/2$	38	450	550	$[2.25 \cdot 10^{-5}, 3.0]$
	0.1770	2×1	62	920	1100	$[1.50 \cdot 10^{-5}, 3.0]$
		$4 \times 1/2$	42	1400	1560	$[1.50 \cdot 10^{-5}, 3.0]$

Table 5.2: *Algorithmic parameters for the simulations done by the qq+q Collaboration. N_f indicates the used determinant-breakup in the polynomial approximation: $N_f = n_b \times N_f^{sim}$. The n_i are the polynomial orders, ϵ and λ are the lower and upper bound, respectively, for the approximation.*

run	κ	r_0/a	am_π	$Z_q am_q^{\mathrm{PCAC}}$	$M_{r_0}/M_{r_0}^{\mathrm{strange}}$	N_{conf}
I	0.1950	1.76(6)	0.519(1)	≈ 0.034	0.268(19)	≈ 1100
II	0.1760	2.149(15)	0.6747(14)	0.07472(32)	0.678(08)	≈ 1800
	0.1765	2.171(88)	0.6211(22)	0.06247(51)	0.588(13)	≈ 750
	0.1770	2.395(52)	0.4354(68)	0.03087(36)	0.351(15)	≈ 1000
III	0.1760	2.229(63)	0.6542(10)	0.07092(27)	0.687(39)	≈ 1000
	0.1765	2.212(44)	0.5793(17)	0.05571(30)	0.530(23)	≈ 1000
	0.1768	2.621(46)	0.3919(46)	0.02566(27)	0.340(12)	≈ 1000
	0.1770	2.528(51)	0.3657(24)	0.02208(31)	0.276(11)	≈ 1000

Table 5.3: *Measured Sommer scale parameter r_0/a, pion masses am_π, and quark masses $Z_q am_q^{PCAC}$ and $M_{r_0}/M_{r_0}^{strange}$. Also the number N_{conf} of analyzed configurations in each point is given.*

The n_i denote the polynomial orders used and n_b is the breakup factor of the determinant (cf. Tab. 5.2). A typical update-sequence, which we refer to as an "update-cycle", consists of two local bosonic heatbath sweeps and one local bosonic overrelaxation sweep, twelve local gauge heatbath sweeps followed by a global correction step, again the two plus one local bosonic sweeps, and twelve local gauge overrelaxation sweeps again followed by a global correction step. We always aim for an acceptance rate of 40%–60% in the correction-steps. After ten of such cycles a global heatbath was done, replacing the boson fields by new ones. Therefore, a typical set of parameters is: $N_\phi = 6$, $N_U = 24$, $N_C = 2$, $F_G = 1/10$. I_G strongly depends on the smallest eigenvalues, i.e., on the simulated quark mass. Usually a configuration was stored for later analysis after 5 or 10 update-cycles.

Finally, the number of FLOP can be calculated from the number of MVMs by noting that[4]

$$1\,\mathrm{MVM} \;=\; 1344 \cdot \Omega\,\mathrm{FLOP}, \quad \Omega = L^3T. \tag{5.52}$$

To get the cost for producing one independent configuration, where independent means with respect to the quantity in question, the measured autocorrelation has to be taken into account. As discussed in [19] the cost can be parametrized as

$$C \;=\; F\,(r_0 m_\pi)^{-z_\pi}\, L^{z_L} \left(\frac{r_0}{a}\right)^{z_a}. \tag{5.53}$$

There $z_\pi \approx 4$ was found. Assuming $z_a = 2$ [112] and the naïve volume dependence $z_L = 4$, one can use $M_{r_0} = (r_0 m_\pi)^2$ as an estimate for the quark mass in the region of small quark masses to rewrite the formula as [98]

$$C_{\tau_{\mathrm{int}}} \;=\; F\,(a m_q)^{-z}\,\Omega. \tag{5.54}$$

Here $z \approx 2$ and the index τ_{int} indicates that the autocorrelation length is used for estimating the cost of an independent configuration. For the quark mass (am_q) one could either use the value obtained from M_{r_0} or am_q^{PCAC}, neglecting the factor $z_A \simeq 1$. In most cases the latter was our preferred choice. The constant F depends on the quantity in question. In our runs we found the values for the average plaquette, pion mass and pion decay constant to be [110]

$$F_{\mathrm{plaq}} \simeq 7 \cdot 10^6, \qquad F_{m_\pi} \simeq 1 \cdot 10^6, \qquad F_{f_\pi} < 4 \cdot 10^5, \tag{5.55}$$

giving the costs in FLOP. For f_π only an upper bound could be estimated, because the stored configurations did not show any autocorrelation. Also these numbers justify the assumption that the plaquette autocorrelation can serve as a worst-case estimate for the autocorrelation of the physical interesting quantities.

5.2.2 Partially quenched analysis

In all our three runs, we performed a PQχPT analysis with five (run I) and twelve (runs II and III) additional valence quark masses, see Tab. 5.4. Calculating the correlators also with this valence quark masses plus the mixed sea-valence correlators enabled us to extract also valence quark masses and pion masses and decay constants for the valence-valence and valence-sea mesons. Besides run I, where we only simulated one dynamical quark mass, we were able to examine the sea quark mass dependence, too.

[4] This formula only applies for the untwisted case. If QCD$^{\mathrm{TM}}$ is used, there is an additional factor of two, because two fermion fields are present.

With the data at hand one can try to fit it with the formulae for the ratios and double ratios presented in the preceding chapter (Sec. 4.1). The values for the valence quark mass ratios ξ and the sea quark mass ratios σ are taken from the ratios of the PCAC-quark mass. In runs II and III we always choose $\kappa_{\rm sea} = 0.1760$ (the highest quark mass) as a reference point (χ_R) for determining σ. The so obtained σ-values are summarized in Tab. 5.5. With this input, it is now possible to perform global fits to the valence quark mass dependence in runs II and III, too. Here "global fit" means to obtain one set of parameters from the valence quark mass dependence of all the simulations at different sea quark masses together. Since we now fixed the reference scale at which the LECs are defined to be χ_R at our highest quark mass, one has to take this into account by the following substitutions in Eqs. (4.24)–(4.31), cf. also Eqs. (4.9), (4.10)

$$\begin{aligned}
\chi_S &\rightarrow \sigma\chi_R, \\
L_{Sk} &\rightarrow L_{Rk}, \\
W_{Sk} &\rightarrow W_{Rk}, \\
\log(1+\eta_S) &\rightarrow \log[\sigma(1+\eta_S)], \\
\log(\xi+\eta_S) &\rightarrow \log[\sigma(\xi+\eta_S)], \\
\log(1+\xi+2\eta_S) &\rightarrow \log[\sigma(1+\xi+2\eta_S)].
\end{aligned}$$

Except for the η-dependence, which is non-linear, one can perform linear fits by using the four parameters

$$\begin{aligned}
\chi_R, \quad & \chi_R L_{R5}, \\
\chi_R L_{R4W6} \equiv\ & \chi_R(L_{R4} - W_{R6}), \\
\chi_R L_{R85} \equiv\ & \chi_R(2L_{R8} - L_{R5}).
\end{aligned} \tag{5.56}$$

Including also the NNLO-tree contributions, Eq. (4.34), eight more parameters are to be included:

$$\chi_R^2 D_{fVV},\ \chi_R^2 D_{nVV},\ \chi_R^2 Q_{fVV},\ \chi_R^2 Q_{fVS},\ \chi_R^2 Q_{fd},\ \chi_R^2 Q_{nVV},\ \chi_R^2 Q_{nVS},\ \chi_R^2 Q_{nd}. \tag{5.57}$$

Here we made use of Eq. (4.38) but not of Eqs. (4.39), (4.40) since the latter would imply a non-linear behavior. But still it can be used as a check of quality for the fitted values. A possible dependence of the $D_{...}$ and $Q_{...}$ on σ has been neglected.

For including the η-dependence one can follow different strategies: one could perform non-linear fits including η as a new parameter at each single value for the sea quark mass. This procedure gives a set η_i. A second step now would be, to take this set as starting values for a more sophisticated global fitting procedure: by varying the η_i and performing the linear, global fits as stated before, one now searches for a minimum of the global χ^2 as a function of the η_i. (Here χ^2 denotes the quadratic deviation from the linear fits, not to be confused with the χ-parameter of the chiral Lagrangian, which appears in the ratios and double ratios.)

At this point we want to stress the fact, that we are able to estimate the effects due to the finite lattice spacing even if we use data generated at just one gauge coupling β. This becomes possible because of the different functional dependence of the $\mathcal{O}(a)$- compared to the quark mass-terms in the (PQ)χPT formulae in the lattice formulation. To confirm the results from this approach, we are still able to do a scaling test between run I ($\beta = 4.68$)

$\kappa_{\rm sea}$	$\kappa_{\rm val}$
0.1950	0.1920, 0.1930, 0.1940, 0.1945, 0.1955
0.1760	0.1685, 0.1705, 0.1720, 0.1730, 0.1735, 0.1745, 0.1750, 0.1770, 0.1775, 0.1785, 0.1790, 0.1800
0.1765	0.1710, 0.1718, 0.1726, 0.1734, 0.1742, 0.1750, 0.1758, 0.1772, 0.1778, 0.1785, 0.1791, 0.1797
0.1768	0.1730, 0.1735, 0.1741, 0.1746, 0.1752, 0.1758, 0.1763, 0.1773, 0.1779, 0.1784, 0.1789, 0.1794
0.1770	0.1743, 0.1747, 0.1751, 0.1754, 0.1759, 0.1763, 0.1767, 0.1775, 0.1779, 0.1783, 0.1787, 0.1791

Table 5.4: *Values for the valence quark hopping parameter κ_{val} in run I (first row) and for the different κ_{sea} in runs II and III (last 4 rows).*

$\kappa_{\rm sea}$	0.1760	0.1765	0.1768	0.1770
σ, run II	1.0	0.8361(52)	–	0.4132(34)
σ, run III	1.0	0.7856(56)	0.3618(44)	0.3113(31)

Table 5.5: *Values for the PCAC-quark mass ratios σ with reference point $\kappa_{sea} = 0.1760$ in runs II and III.*

and runs II and III ($\beta = 5.10$) and, of course, compare our obtained values for the universal low energy constants to results from other lattice groups. The latter will be postponed to the last part of this section.

Valence quark analysis of run I

In the analysis of run I in principle one can do a multi-parameter fit to obtain the five quantities (the four listed in Eq. (5.56) plus η) from the six ratios and double ratios. The NNLO-tree contributions were neglected, since one expects the discretization errors to overwhelm these at our coarse lattice spacing and low quark mass. However, it turned out that fitting all these ratios in one step resulted in an unstable procedure. We believe that this situation could have been improved by a better choice of the valence quark masses, e.g., using more than one valence quark mass with $\xi < 1$. Also increasing the statistics and going to finer lattice spacings should improve that situation. We applied this in the following runs II and III. Here we chose to perform a sequence of double or single parameter fits of just one ratio at a time.

A good starting candidate is the double ratio RRf, Eq. (4.30), which in NLO just depends on χ_S and η. (Here no difference between χ_S and χ_R occurs, because only one sea quark mass is present.) The fit shown in the left panel of Fig. 5.1 (short-dashed line) resulted in

$$\chi_S \;=\; 9.2(2.5), \quad \eta \;=\; 0.14(30). \tag{5.58}$$

The value for χ_S is reasonable compared to the estimate from the tree-level χPT formula $\chi^{\rm est} \approx M_{r_0}/(r_0 f_0)^2 \simeq 15.7$. From Rf_{VV} we then extracted L_{S5} with a single parameter fit

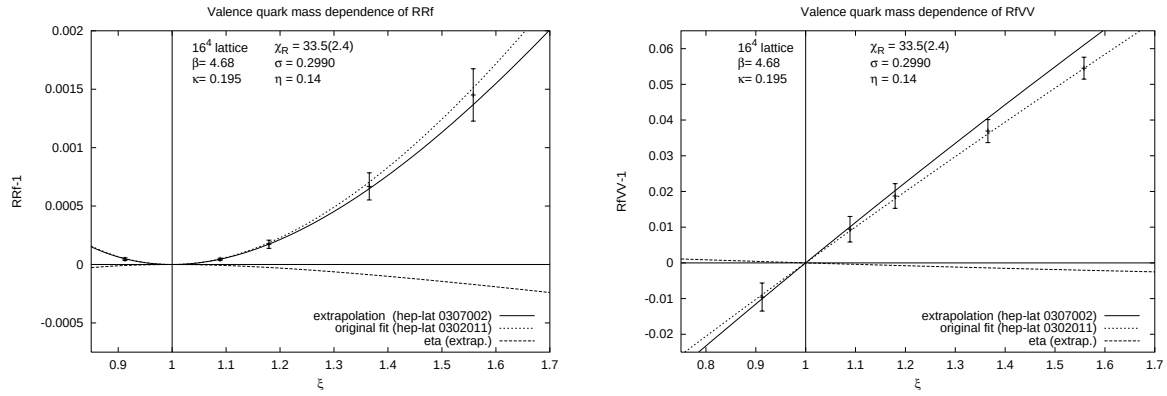

Figure 5.1: *Valence quark mass dependence of* $(RRf-1)$ (left panel) *and* $(Rf_{VV}-1)$ (right panel). *In both cases the original fit (short dashed line) and the extrapolation (solid line) from run II is shown. For the latter also the* η*-dependent piece is plotted separately (dashed line), which is* $(R|_{\eta\neq 0}-R|_{\eta=0})$*. For details on the fits and extrapolation: see text.*

(short-dashed line in the right panel of Fig. 5.1) by fixing $\chi_S = 10, \eta = 0.10$:

$$L_{S5} \;=\; 0.0034(1), \quad \alpha_5 \;=\; 1.55(24), \tag{5.59}$$

using Rf_{VS} instead gave similar values. The value of $(2L_{S8}-L_{S5})$ is obtained in a single parameter fit (χ and η fixed as before) by observing that the linear combination

$$LRm \;=\; 2Rm_{VS}-Rm_{VV} = (\xi+1)Rn_{VS}-\xi Rn_{VV} \tag{5.60}$$

cancels the term proportional to $(L_{S4}-W_{S6})$:

$$2L_{S8}-L_{S5} \;=\; -0.00177(3), \quad 2\alpha_8-\alpha_5 \;=\; 0.58(3). \tag{5.61}$$

Finally, we got $(L_{S4}-W_{S6})$ from $RRm = \frac{(\xi+1)^2}{4\xi} RRn$ to be:

$$L_{S4}-W_{S6} \;=\; 0.00358(6). \tag{5.62}$$

By anticipating the results from run II, we also may use this run at a lower β for a scaling test [109]. Extrapolating σ from run II to the value of the quark mass at this point gives $\sigma \approx 0.2990$, which now should be used together with $\chi_R = 33.5(2.4)$ from run II and $\eta = 0.14$ like before. The resulting curves from this set of values are also shown in the case of RRf and Rf_{VV} in Fig. 5.1 (solid line, the dashed line shows just the part depending on η). In case of Rf_{VV} also the value for L_{R5} from run II (cf. Tab. 5.6) had to be used. As one sees, the extrapolated curves show only small scale breaking effects.

Valence quark analysis of runs II and III

Before applying a global fit strategy to the points in run II, we first examined each κ_{sea} independently with a procedure similar to the one described in the last paragraph fitting η and the quantities in Eq. (5.56). But the NLO-PQχPT predictions did not agree very well with our data: from the independently fitted values of $\chi_S^{\kappa_i}$ one would get ratios $\sigma_i^{\chi} = \chi_S^{\kappa_i}/\chi_R^{\kappa_R}$ much closer to 1.0 than σ from the quark masses, reported in Tab. 5.5. Also the logarithmic scale dependence of the LECs, Eqs. (4.9), (4.10), could not be reproduced. Both of these are necessary for a reliable global fit, showing the importance of NNLO-corrections in this case. We included the relevant parameters, Eq. (5.57), in the fits and first determined the η_i by performing global linear fits as a function of η, trying to find a minimum of the quadratic deviation, like mentioned in the beginning of this section. The minimum is rather shallow, but definitely bounded by $0 \leq \eta \leq 0.10$, for a best-fit set, cf. Tab. 5.6. Also by just fitting a sub-set of functions (leaving out some ratios or double ratios) or varying the range of the fit (excluding some valence quark masses), these values remain stable in contrast to the situation for the crucial parameter χ_R. This parameter is crucial in the sense that all the other linearly fitted ones contain some power of it. Here we could obtain values in the range $13 \leq \chi_R \leq 40$, depending on the functions or range fitted. During this analysis RRn turned out to be the most stable function, so we first determined χ_R, $\chi_R L_{R4W6}$, and $\chi_R^2 Q_{nd}$ from it (with the η's fixed to the previously obtained values) and used it as an input for the rest. The resulting parameters are listed in Tab. 5.6 with the fits shown in Figs. 5.2, 5.3. The total quadratic deviation $\chi^2 \simeq 300$ is reasonable for a number of degrees of freedom = 204. The predicted relations for the NNLO-parameters, Eqs. (4.39), (4.40), show some small deviations: $-0.89(49) \cdot 10^{-5} \simeq 2.05(39) \cdot 10^{-5}$ and $5.2(9) \cdot 10^{-6} \simeq 9.2(8) \cdot 10^{-6}$, respectively. Summarizing, the interesting LECs obtained from this analysis are

$$\alpha_5 = 2.24(20), \tag{5.63}$$

$$2\alpha_8 - \alpha_5 = 0.762(49). \tag{5.64}$$

By observing the small values for η and respecting the fact that only including NNLO-contributions led us to reasonable fits, we tried to neglect the $\mathcal{O}(a)$-terms completely and also got reasonable fits, with not to much different values for χ_R and the LECs. Another gain of information we took from this, is the observation that the NNLO-terms are much more important at both higher sea quark masses (their importance decreases with κ_{sea} increasing from 0.1760 to 0.1770) and higher valence quark masses ($\xi > 1$). Also compare Fig. 5.5 from run III, where the NLO-part is plotted separately. It turned out that the double ratios are much less influenced by the NNLO-corrections than the single ratios.

With the experience we gained from the simulations at the 16^4-lattices (run II), we first examined the importance of $\mathcal{O}(a)$- compared to NNLO-terms in run III. Again varying η we found a minimum in χ^2 from the global linear-fits at values $|\eta| < 0.1$, see Fig. 5.4 (left panel). In other words ρ, parametrizing the lattice artifacts, is less than 10% of the value of the quark mass parameter. This already gives a hint, that again NNLO-corrections may be more important. A systematic way to proof this assumption with our data is to examine the combination $(RRn + 2RRf - 3)$ of double ratios, which can be expressed

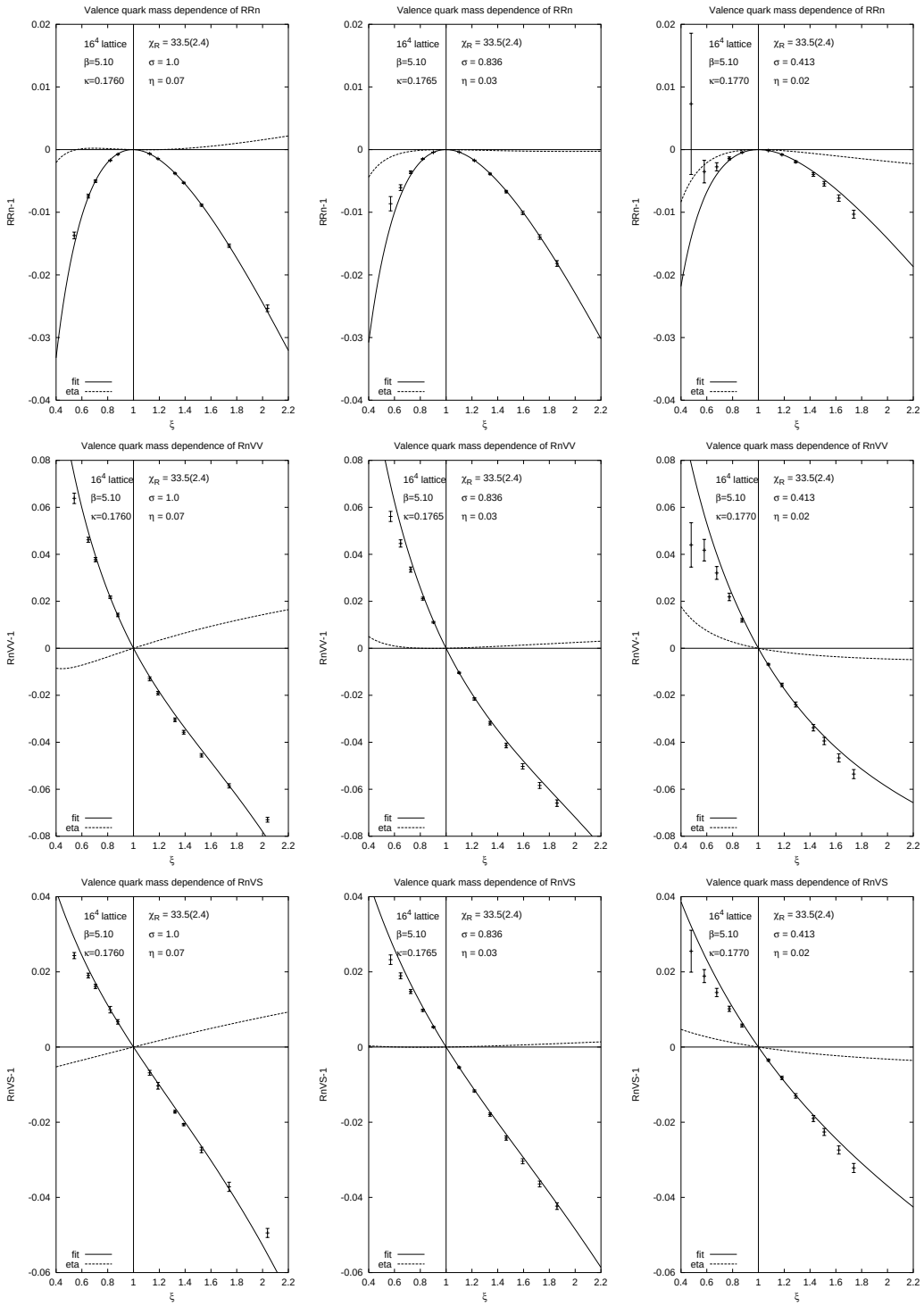

Figure 5.2: *The valence quark mass dependence of the double ratio* $(RRn-1)$ *and ratios* $(Rn_{VV}-1)$ *and* $(Rn_{VS}-1)$ *for the three different sea quark mass values of run II. Besides the best fit (solid line) with parameters from Tab. 5.6 the* η*-dependent part is shown separately (dashed line).*

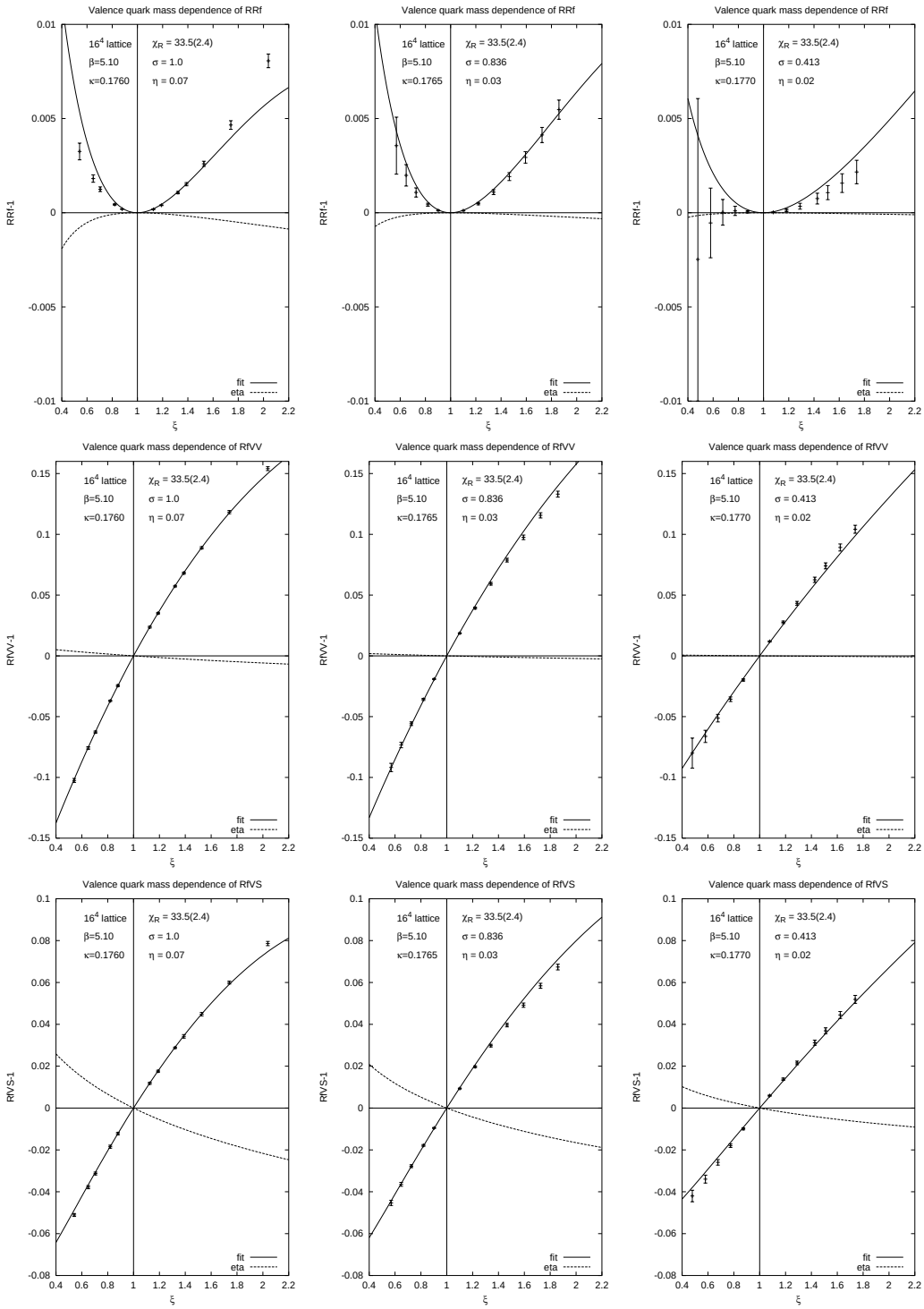

Figure 5.3: *The valence quark mass dependence of the double ratio* $(RRf - 1)$ *and ratios* $(Rf_{VV} - 1)$ *and* $(Rf_{VS} - 1)$ *for the three different sea quark mass values of run II. Besides the best fit (solid line) with parameters from Tab. 5.6 the* η*-dependent part is shown separately (dashed line).*

	run II	run III		run II	run III
χ_R	33.5(2.4)	35.8(3.3)			
$\chi_R L_{R5}$	0.1006(44)	0.1003(76)	L_{R5}	$3.00(19)\cdot 10^{-3}$	$2.80(39)\cdot 10^{-3}$
$\chi_R L_{R85}$	−0.0210(12)	−0.0256(12)	L_{R85}	$-6.25(52)\cdot 10^{-4}$	$-0.714(65)\cdot 10^{-3}$
$\chi_R^2 D_{fVV}$	−0.093(17)	−0.109(42)	D_{fVV}	$-8.3(1.9)\cdot 10^{-5}$	$-8.5(4.4)\cdot 10^{-5}$
$\chi_R^2 Q_{fVV}$	−0.0280(19)	−0.014(29)	Q_{fVV}	$-2.50(50)\cdot 10^{-5}$	$-1.1(2.3)\cdot 10^{-5}$
$\chi_R^2 Q_{fVS}$	−0.02197(45)	−0.0177(94)	Q_{fVS}	$-1.96(29)\cdot 10^{-5}$	$-1.39(81)\cdot 10^{-5}$
$\chi_R^2 Q_{fd}$	−0.0099(14)	−0.0180(31)	Q_{fd}	$-0.89(45)\cdot 10^{-5}$	$-1.41(13)\cdot 10^{-5}$
$\chi_R^2 D_{nVV}$	−0.167(20)	−0.134(21)	D_{nVV}	$-1.49(10)\cdot 10^{-4}$	$-1.046(93)\cdot 10^{-4}$
$\chi_R^2 Q_{nVV}$	−0.0844(67)	−0.087(13)	Q_{nVV}	$-7.53(48)\cdot 10^{-5}$	$-6.77(30)\cdot 10^{-5}$
$\chi_R^2 Q_{nVS}$	−0.0405(25)	−0.0394(44)	Q_{nVS}	$-3.61(29)\cdot 10^{-5}$	$-3.07(24)\cdot 10^{-5}$
$\chi_R^2 Q_{nd}$	0.0065(18)	0.0077(48)	Q_{nd}	$5.80(79)\cdot 10^{-6}$	$6.0(2.6)\cdot 10^{-6}$
η_i	$0.07, 0.03, 0.02$	–			
$\chi_R L_{R4W6}$	0.0524(38)	–	L_{R4W6}	$1.564(71)\cdot 10^{-3}$	–

Table 5.6: *Values of the best fit parameters (left major column) in runs II and III. The right major column shows the therefrom deduced values. In run II the highest η-value belongs to $\kappa = 0.1760$, the lowest to $\kappa = 0.1770$.*

either in terms due to the lattice artifacts or the NNLO-contributions:

$$\begin{aligned} RRn + 2RRf - 3 &= \\ \mathcal{O}(a): &= 16\rho L_{S4W6}\frac{(\xi-1)^2}{\xi(\xi+1)} - \rho\frac{(\xi-1)^2}{\chi_S\xi(\xi+1)} \\ &\quad +\rho\frac{[2(1-\xi^2)+\log\xi+3\xi^2\log\xi]}{32\pi^2\xi(\xi+1)} + \rho\frac{\xi-1-\xi\log\xi}{32\pi^2\xi} \\ &\quad +\mathcal{O}(\rho^2,\chi_S^2) \qquad (5.65) \\ \text{NNLO}: &= (Q_{nd}+2Q_{fd})\chi_S^2(\xi-1)^2 + \mathcal{O}(\chi_S^2\log\xi,\chi_S^3). \qquad (5.66) \end{aligned}$$

In the $\mathcal{O}(a)$-formula only the piece linear in $\eta = \rho/\chi_S$ was kept, because η is already known to be small. Fitting our data with these different ansätze, the NNLO-fit turned out to give a better χ^2. An example is shown in Fig. 5.4 (right panel), there the χ^2 turned out to be 1.3 (from NNLO) vs. 7.2 (from $\mathcal{O}(a)$).

The total fit program was now applied to our valence data, setting $\eta = 0$. This also reduces the number of parameters by one, because L_{R4W6} always comes with a factor η. The results are again displayed in Tab. 5.6, with some example fits shown in Fig. 5.5. These plots also illustrate the increasing importance of NNLO-terms with decreasing quark mass like stated before: the dashed lines correspond to the NLO-part alone. Unfortunately *exceptional configurations* appeared, i.e., configurations with extreme small eigenvalues which are not sufficiently suppressed by the fermion determinant. Therefore, we had to restrict the valence quark analysis in most of the cases to valence quarks with masses higher than the sea quark mass ($\xi > 1$). Again we give the obtained values for the LECs:

$$\begin{aligned} \alpha_5 &= 2.06(42), \qquad (5.67) \\ 2\alpha_8 - \alpha_5 &= 0.583(45). \qquad (5.68) \end{aligned}$$

These are in agreement with the previously found ones, Eqs. (5.63), (5.64): α_5 is practically the same, while $(2\alpha_8 - \alpha_5)$ went down a little. The same already holds, when one compares

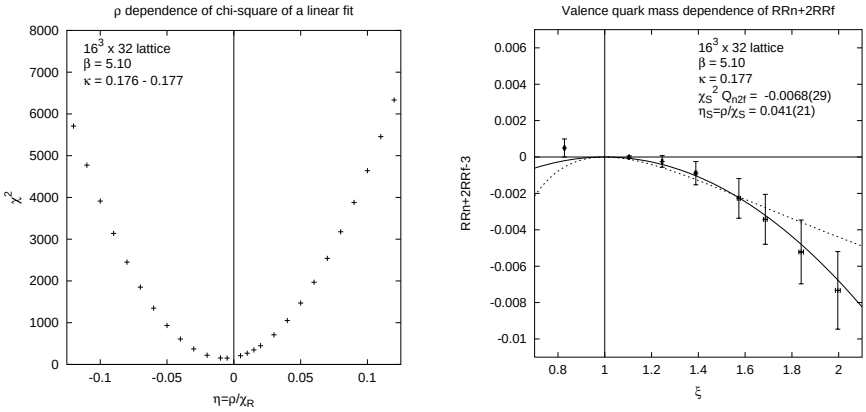

Figure 5.4: Left panel: χ^2 *from the global linear fits as a function of* η. Right panel: *Fitting* $(RRn + 2RRf - 3)$ *with the NNLO- (solid line) or* $\mathcal{O}(a)$*- (dashed line) prediction, Eqs. (5.66) or (5.65), respectively.*

directly the fitted parameters in Tab. 5.6, which shows the stability of our ratios. This feature is even more surprising, if one keeps in mind the shifts in the pion masses etc. found at the sea quark level, cf. the discussion at the beginning of this section. A nice illustration of the stability of the "ratios as functions of ratios" is provided by Fig. 5.6, where Rn_{VS} and RRn from runs II and III are plotted simultaneously for the lowest and highest sea quark mass value, respectively: the two simulations are resulting (within errors) in one curve. The reason for this to happen is the cancellation of unwanted renormalization factors in the ratios. Maybe to some extent also lattice artifacts might be reduced by this procedure.

Sea quark analysis of runs II and III

The sea quark analysis incorporates the two ratios Rf_{SS} and Rn_{SS}, Eqs. (4.16), (4.17). Each of these contain two new parameters (the following linear combinations are valid only for $N_s = 2$)

$$L_{R45} \equiv 2L_{R4} + L_{R5}, \tag{5.69}$$

$$W_{R45} \equiv 2W_{R4} + W_{R5}, \tag{5.70}$$

$$L_{R6845} \equiv 4L_{R6} + 2L_{R8} - 2L_{R4} - L_{R5}, \tag{5.71}$$

$$W_{R6845} \equiv 4W_{R6} + 2W_{R8} - 2W_{R4} - W_{R5}, \tag{5.72}$$

the rest, namely χ_R and the η_i, can be taken from the valence quark mass analysis. In run II with only three different sea quark mass values, one ends up with two independent points for each ratio, which means the equations are just solved for the four unknowns and not fitted. Results are reported in Tab. 5.7. Exactly because of this, we decided to add a further intermediate sea quark mass in run III. This opens the opportunity for two different approaches: the previously described one, where one takes χ_R from the valence quark mass analysis, or performing a linear fit with the parameters

$$\chi_R,\ \chi_R L_{R45},\ \chi_R L_{R6845}.$$

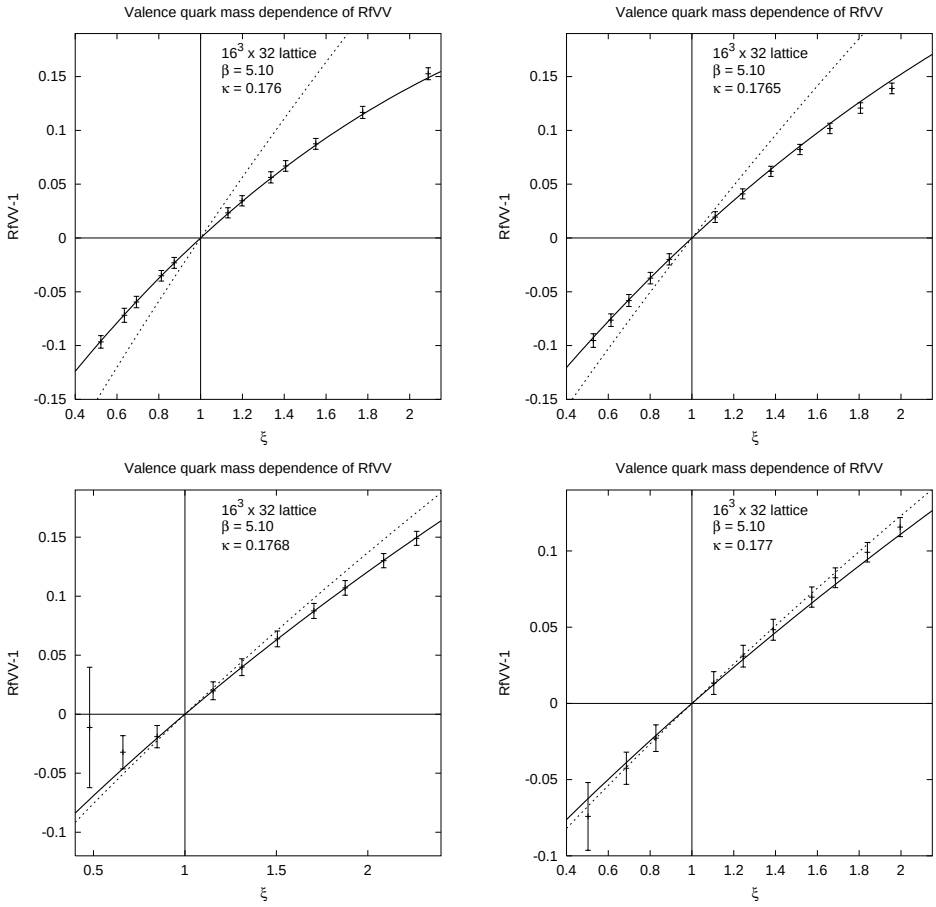

Figure 5.5: *The valence quark mass dependence of the ratio* $(Rf_{VV} - 1)$ *as an example for the fits in run III. The solid lines show the full fit, the dashed lines only the NLO-part* $(Q_{fVS} = D_{fVV} = 0)$.

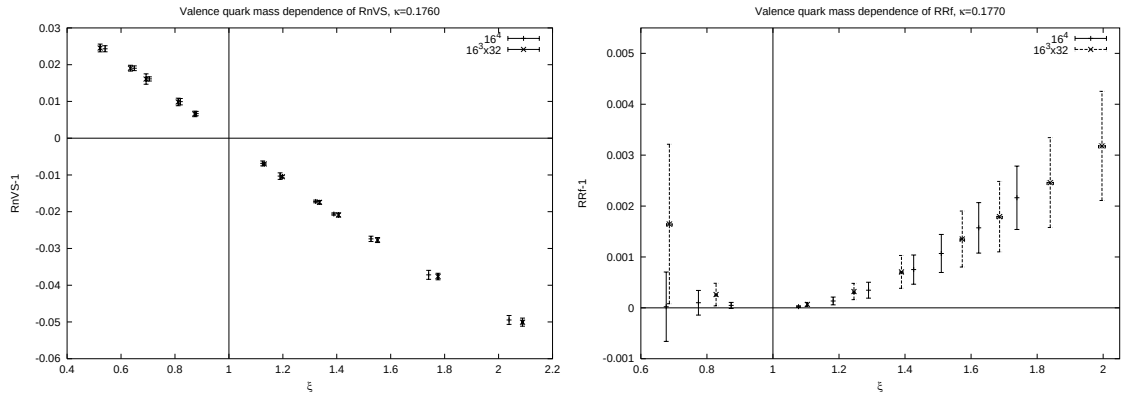

Figure 5.6: *Comparing the ratio* $(Rn_{VS} - 1)$ *at* $\kappa_{sea} = 0.1760$ *and double ratio* $(RRf - 1)$ *at* $\kappa_{sea} = 0.1770$ *as a function of the valence quark mass parameter* ξ *from run II (*16^4*-lattice) with the ones from run III (*$16^3 \times 32$*-lattice).*

run II, $\chi_R = 33.5(2.4), \eta = 0.07, 0.03, 0.02$ *fixed*

L_{R45}	$4.34(28) \cdot 10^{-3}$	Λ_4/f_0	22.9(1.5)
W_{R45}	$1.1(1.4) \cdot 10^{-3}$		
L_{R6845}	$-9.1(6.4) \cdot 10^{-5}$	Λ_3/f_0	6.51(57)
W_{R6845}	$-5.52(48) \cdot 10^{-3}$		

run III, χ_R *fitted,* $\eta = 0$

χ_R	30.8(9.4)				
$\chi_R L_{R45}$	0.1398(86)	L_{R45}	$4.5(1.1) \cdot 10^{-3}$	Λ_4/f_0	23.3(8.2)
$\chi_R L_{R6845}$	$-0.0078(22)$	L_{R6845}	$-2.54(21) \cdot 10^{-4}$	Λ_3/f_0	7.64(14)

run III, $\chi_R = 35.8(3.3)$ *fixed,* $\eta = 0$

$\chi_R L_{R45}$	0.1443(15)	L_{R45}	$4.03(37) \cdot 10^{-3}$	Λ_4/f_0	21.4(1.5)
$\chi_R L_{R6845}$	$-0.00896(86)$	L_{R6845}	$-2.50(34) \cdot 10^{-4}$	Λ_3/f_0	8.21(27)

Table 5.7: *Results from different fits of the sea quark dependence in runs II and III. For details see text.*

(Note that here we can set $\eta_i = 0$ as argued before, which removes terms containing W_{R45} and W_{R6845}.) It turned out that the fits with χ_R fixed gave smaller errors, but both are consistent, cf. Tab. 5.7. Fig. 5.7 shows the plots for the fits with χ_R fixed. While both the pion decay constant and the pion mass-squared dependence on the quark mass ratio can be fitted with the NLO χPT prediction, only the first one clearly displays the presence of the *chiral logarithm*. The latter is also consistent with such a functional form, but unfortunately the ratios are all consistent to 1.0 within error. One can now use χPT to extrapolate Rf and Rn to zero quark mass:

$$Rf_0 \;=\; 0.4228(60), \quad Rn_0 \;=\; 1.0717(69). \tag{5.73}$$

Taking Rf_0 together with the result for $Z_A^{-1} a f_\pi = 0.2819(15)$ at the reference point ($\kappa_{\rm sea} = 0.1760$) one estimates

$$Z_A^{-1} f_0 \;=\; 121(5)\text{MeV}, \tag{5.74}$$

which is consistent with $f_0 = 93$ MeV, if one assumes Z_A to be of $\mathcal{O}(1)$.

5.2.3 Chiral fits from runs using the DBW2 gauge action

As a byproduct of our studies using the DBW2 gauge action (Sec. 5.3.2) we also performed untwisted simulations with $N_f = 2$ at two lattice sizes, $L^3 \times T = 12^3 \times 24$ and $16^3 \times 32$ with β set to 0.67 and 0.74, respectively. The motivation was to examine the scaling properties, if this particular gauge action is applied. Since this can be done using the chiral predictions on the quark mass dependence of the pion masses squared and decay constants, we will present it in the context of determining the LECs from lattice simulations. The analysis will provide us with estimates for the universal low energy scales $\Lambda_{3,4}$, too.

The lattice spacings turned out to be $a \approx 0.19 \sim 0.22$ fm ($12^3 \times 24$, $\beta = 0.67$) and $a \approx 0.13 \sim 0.14$ fm ($16^3 \times 32$, $\beta = 0.74$). The gauge couplings were tuned to give roughly the same physical volume ($aL \approx 2.2$ fm) on both lattice sizes therefore allowing for a scaling test. κ was set to 0.1650, 0.1655, 0.1660, and 0.1665 at $\beta = 0.67$, resulting in

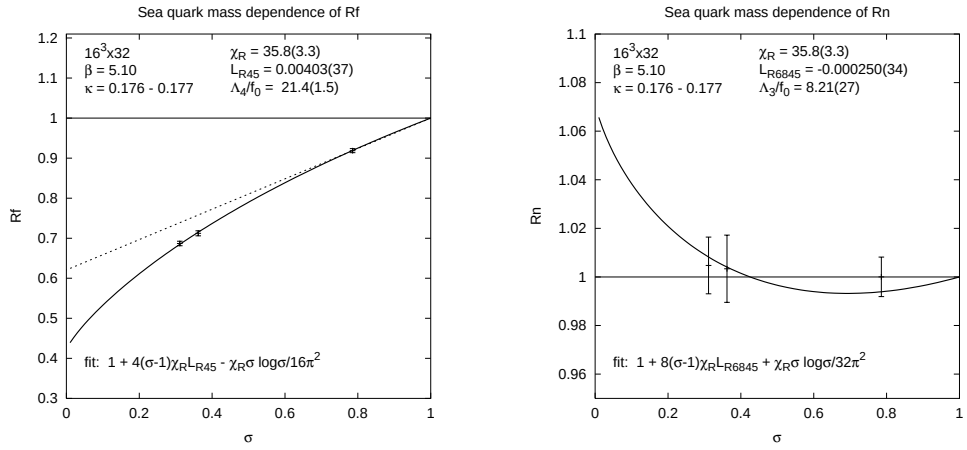

Figure 5.7: *Sea quark mass dependence of Rf_{SS}* (left panel) *and Rn_{SS}* (right panel) *in run III. The dashed line in the Rf-plot connects the first two points to illustrate the non-linearity, i.e., the presence of the chiral logarithm. Notice that the fourth point ($\sigma = 1$, Rf or $Rn = 1$) is used for defining the ratios.*

quark masses in the range $0.12 \cdot m_s$ to $0.36 \cdot m_s$ (using M_{r_0} for these estimates). At $\beta = 0.74$ two different masses were simulated: $\kappa = 0.1580$ and 0.1585, corresponding to $0.38 \cdot m_s$ and $0.23 \cdot m_s$, respectively.

To set a common reference point in the scaling analysis, we decided to fix the scale at $M_{r_0} = 1$. Actually, we tried to choose the mass parameters in such a way, to have two simulations in the vicinity of this point, allowing for a linear interpolation between them. We define $R_1 f$ to be the ratio of the pion decay constant at some quark mass with respect to the interpolated value of af_π at $M_{r_0} = 1$:

$$R_1 f \;\equiv\; \frac{[af_\pi](m_q)}{[af_\pi](m_q|_{M_{r_0}=1})} \tag{5.75}$$

and similar for the pion mass squared ratio (divided by its tree-level value)

$$R_1 n \;\equiv\; \frac{[(am_\pi)^2](m_q)}{\sigma_1[(am_\pi)^2](m_q|_{M_{r_0}=1})}. \tag{5.76}$$

Both are considered as functions of the quark mass ratio

$$\sigma_1 \;\equiv\; \frac{am_\chi^{\mathrm{PCAC}}}{am_\chi^{\mathrm{PCAC}}|_{M_{r_0}=1}}, \tag{5.77}$$

which already entered the definition of $R_1 n$. With this definition $R_1 f$ and $R_1 n$ should show a dependence like Rf_{SS}, Eq. (4.16), and Rn_{SS}, Eq. (4.17), respectively:

$$R_1 f \;=\; 1 \,+\, 4(\sigma_1 - 1)\chi_R L_{R45} \,-\, \frac{\chi_R}{16\pi^2}\,\sigma_1 \log \sigma_1, \tag{5.78}$$

$$R_1 n \;=\; 1 \,+\, 8(\sigma_1 - 1)\chi_R L_{R6845} \,+\, \frac{\chi_R}{32\pi^2}\,\sigma_1 \log \sigma_1, \tag{5.79}$$

where $\mathcal{O}(a)$ and NNLO effects have been neglected. Trying to fit with this formulae, single two parameter fits (i.e., fitting the ratios independently with free parameters χ_R and $L_{...}$)

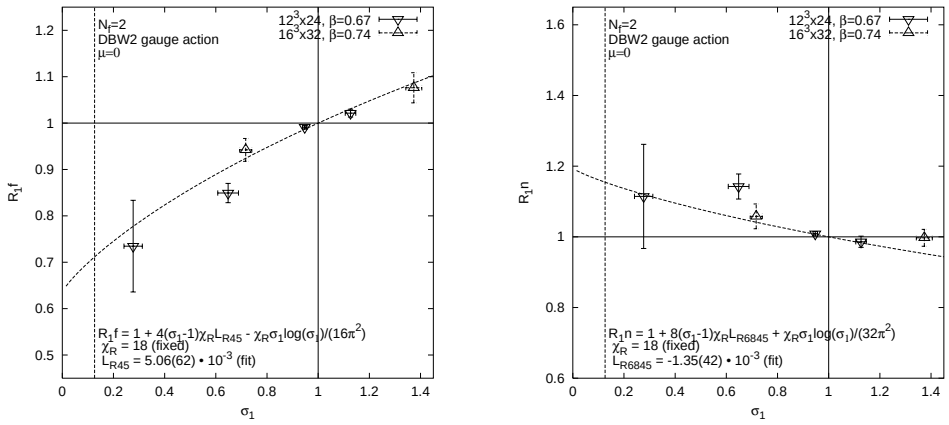

Figure 5.8: *Scaling tests for two lattice sizes using the DBW2 gauge action. In both plots the value of the quark mass ratio at the physical pion mass is indicated by a vertical dashed line.* Left panel: *Pion decay constant ratio $R_1 f$ as a function of the quark mass ratio σ_1. Shown is a one parameter fit to obtain L_{R45}.* Right panel: *Pion mass squared ratio $R_1 n$ as a function of the quark mass ratio σ_1. Shown is a one parameter fit to obtain L_{R6845}.*

turned out to be very unstable, resulting in a large range for χ_R. Such a behavior is expected from the previous PQχPT-analysis, where a reliable value for χ_R was obtained with the help of the double ratio RRn. Again this demonstrates the advantages of the partially quenched ansatz to extract information in a stable way from numerical simulations. Since up to now we did not produce partially quenched data from these runs, we prefer to fix $\chi_R = 18$. To arrive at this estimate, one could either take the tree-level estimate $\chi^{\rm est} \approx M_{r_0}/(r_0 f_0)^2$, or extrapolate the results from runs II and III (previous section) to $M_{r_0} = 1$, both resulting in the above value. The fits are shown by Fig. 5.8, resulting in estimates for the universal low energy scales

$$\frac{\Lambda_4}{f_0} = 21(4) \quad (\text{from } R_1 f), \tag{5.80}$$

$$\frac{\Lambda_3}{f_0} = 23(12) \quad (\text{from } R_1 n). \tag{5.81}$$

While Λ_4/f_0 is extracted with a reasonable error and in good agreement with the previously found estimates, the determination of Λ_3/f_0 is uncertain. Compared to Fig. 5.7, right panel, it is remarkable that here the pion mass squared ratio is no longer consistent to 1.0 within errors. The chiral behavior can be observed.

Also no large scaling violations are visible from this data. Excluding in each of the fits the two points from the larger lattices, the resulting values for the so fitted parameters agree within errors, showing that the $16^3 \times 32$ lattice data having a finer lattice spacing can be described using the $12^3 \times 24$ lattice data only. For a reliable scaling test at least one or two more points at smaller quark mass on the finer lattice would be needed. But this first analysis did not give any hints on scaling violations down to quark masses of $\approx {}^1\!/_4 m_s$ for lattice spacings of $a \approx 0.14$ fm, if the DBW2 gauge action is applied.

	run I	run II	run III	DBW2
α_5	1.55(24)	2.24(20)	2.06(42)	–
$2\alpha_8 - \alpha_5$	0.58(3)	0.762(49)	0.583(45)	–
Λ_3/f_0	–	6.51(57)	8.21(27)	23(12)
Λ_4/f_0	–	22.9(1.5)	21.4(1.5)	21(4)

Table 5.8: *Summary of the results for the LECs* $\alpha_i = 128\pi^2 L_i', i = 5, 8$*, at a reference scale* $\mu = 4\pi f_0$ *and the universal low energy scales* $\Lambda_{3,4}$*.*

5.2.4 Summary

We obtained values for α_5 and $(2\alpha_8 - \alpha_5)$ from our simulations with $N_f = 2$ light quark flavors, summarized in Tab. 5.8. To make contact with experimentally obtained values, clearly one would need to simulate $N_f = 3$ or even more realistic $N_f = 2{+}1$. In [113] no big differences between $N_f = 0$ (quenched) and $N_f = 2$ lattice results have been found, which justifies the assumption that the same holds for $N_f = 2$ versus $N_f = 3$. Nevertheless, for sure we can compare with the $N_f = 2$ UKQCD-data from [113], giving:

$$\alpha_5 \;=\; 1.22(11), \quad (2\alpha_8 - \alpha_5) \;=\; 0.36(10).$$

Despite our value for α_5 is a bit higher, the agreement is reasonable. The MILC-collaboration found in their $N_f = 3$ simulations[5][114]

$$\alpha_5 \;=\; 0.13(76), \quad (2\alpha_8 - \alpha_5) \;=\; 0.76(36).$$

For a phenomenological value we quote[6][115]

$$\alpha_5 \;=\; 0.5(6), \quad \alpha_8 \;=\; 0.8(4),$$

which gives $(2\alpha_8 - \alpha_5) \approx 1.1(1.4)$. For the universal low energy scales the CP-PACS collaboration [116] found with $N_f = 2$ the value

$$\Lambda_4 \;=\; 2.44(13)\ \text{GeV} \;=\; 26.2(1.4) \cdot f_0,$$

which also agrees very well with our result. Phenomenological estimates have been given in [117]

$$\begin{aligned} 0.2\ \text{GeV} = 2.2 \cdot f_0 \;<\; \Lambda_3 \;&<\; 21.5 \cdot f_0 = 2\ \text{GeV} \\ \Lambda_4 \;&=\; 1.26(14)\ \text{GeV} = 13.5(1.5) \cdot f_0. \end{aligned}$$

Compared with both, the CP-PACS and our results, this still shows some disagreement for Λ_4 but the right order of magnitude. While with the error bounds for the phenomenological obtained Λ_3 no statement can be made.

Although these results look promising, one should keep in mind, that still all these chiral extrapolations are done at too high quark masses. More importantly, the numerical simulations have only been performed at a rather coarse lattice spacing $a \simeq 0.2$ fm. An

[5]Results were quoted there as L_i at a scale $\mu = m_\eta \approx 548$ MeV: $L_5 = 1.9(3)(3) \cdot 10^{-3}$, $(2L_8 - L_5) = -0.2(1)(2) \cdot 10^{-3}$.

[6]Results were quoted there as L_i at a scale $\mu = m_\rho \approx 776$ MeV: $L_5 = 1.4(5) \cdot 10^{-3}$, $L_8 = 0.9(3) \cdot 10^{-3}$.

extrapolation to the continuum limit has not yet been tried. As a consequence of this, the chiral logarithms are not very convincing in the case of the pion mass ratio (Rn), and maybe still questionable for the ratio of decay constants (Rf). While we were already plagued by the difficulties of simulating small quark masses with the Wilson-fermion action, like the occurrence of configurations with exceptional small eigenvalues and slowing down of the algorithmic performance, going even lighter and closer to the continuum limit would have been a hard business. For that reason in the remainder of this chapter we examine the twisted mass formulation, which helps to overcome these problems.

5.3 QCD$^{\mathrm{TM}}$ and phase structure studies

The twisted mass formulation (Chapter 2), besides its advantage of automatic $\mathcal{O}(a)$-improvement (Sec. 2.2), also allows to studying the phase structure of lattice QCD near zero quark mass (at zero temperature). Given a non-zero value of the twisted mass parameter μ, simulations with changing the untwisted mass parameter μ_κ in the vicinity of its critical value become easier or even are only possible in this way: the twisted mass term provides a lower bound to the eigenvalue spectrum of the fermion matrix, cf. Eq. (2.11). In Sec. 3.3 we discussed the two possible phase structure scenarios for $N_f = 2$ Wilson fermions near zero quark mass. With a numerical study using the QCD$^{\mathrm{TM}}$ action and varying the untwisted mass parameter in a region around its critical value, it should be possible to decide which of the two possible phase structure scenarios are realized for a given choice of the lattice action. To know the phase structure for the applied (combination of) lattice action(s) is crucial, since, e.g., a minimal pion mass can be imposed due to the phase structure.

We performed such studies in an ongoing project, collaborating with the Westfälische Wilhelms-Universität Münster, NIC/DESY Zeuthen, Freie Universität Berlin, and Humboldt Universität zu Berlin. Some results have already been published in [118, 119, 33]. The simulations were done with two different algorithms: the TSMB-algorithm for QCD$^{\mathrm{TM}}$, as presented in Sec. 5.1.2, and a HMC-algorithm based approach. The latter was developed by our collaborators from NIC/DESY Zeuthen, for details on its implementation cf. [118, 120, 121]. By using two completely different algorithms we were able to perform cross-checks for our results. Especially because our numerical studies are the first ones using *dynamical* twisted mass fermions, such checks were valuable. Also they exclude the possibility that our findings for the phase structure and the found metastabilities are algorithm-dependent. In all the cases we will discuss below, we compared results coming from both, the TSMB- and the HMC-algorithm, showing always an agreement.

In the first section, we describe our initial study, where the QCD$^{\mathrm{TM}}$ action was used together with the Wilson plaquette action for the gauge part. With this set-up strong metastabilities in the observed quantities were found. We will identify the different phases as regions of positive and negative quark mass, and discuss the results on the basis of the phase structure scenarios for lattice QCD. We will argue, that this combination of gauge and fermion actions leads to an unsatisfactory high value for the minimal pion mass. In the following section, after presenting our motivations for using improved gauge actions to weaken this restriction, we will apply the DBW2 action for the gauge part. In the remainder we will demonstrate how to obtain relevant observables from QCD$^{\mathrm{TM}}$-simulations.

5.3.1 Metastabilities and phase transitions

In a situation where no Aoki phase is present, according to the results presented in Sec. 3.3.2, one expects a first order phase transition line for some range of μ, $|\mu| \leq \mu_{\text{end-point}}$, as indicated in Fig. 3.2 (lower panel). According to [25] at $\beta = 5.2$ such a situation is realized. A hint on a first order phase transition is the occurrence of hysteresis signs in so-called thermal cycles. A thermal cycle in κ consists of a series of simulations at fixed β and μ, while first κ is increased stepwise starting from some initial value until a final value has been reached. Afterwards κ is decreased with the same step-size back to the initial value. At each single κ-value the same number of update-sweeps is performed without any thermalization-sweeps. One always starts from the last configuration produced with the previous κ-value. The average plaquette value ($\langle P \rangle = \langle \frac{1}{3} \text{ReTr} U_{\mu\nu} \rangle$) is measured during these sweeps. Fig. 5.9 (left panel) shows the results for a lattice size of $L^3 \times T = 8^3 \times 16$, $\beta = 5.2$ at three different values for the twisted mass parameter. At $\mu = 0$ and $\mu = 0.01$ one sees a hysteresis, which at $\mu = 0.1$ already might have disappeared.

Indeed, the metastabilities signaled by the thermal cycles could be found in longer runs. We decided to fix $\mu = 0.01$ and run simulations on $12^3 \times 24$-lattices ($\beta = 5.2$) starting either from an ordered or a disordered configuration. The history of the average plaquette value is shown for four different values of κ in Fig. 5.9 (right panel). We also performed a run with $\mu = 0$ and one at a larger lattice ($L^3 \times T = 16^3 \times 32$). In all these simulations the observed plaquette values signaled a strong metastability. The gap in the plaquette expectation value is of the order ≈ 0.02. Runs at sufficiently lower or higher κ thermalized in the end at a low or high plaquette value, respectively, independent from the starting condition (not shown). These metastabilities are in perfect agreement with the ones observed in [64]. When we will turn to the improved gauge actions (Sec. 5.3.2), a more detailed examination of the untwisted case ($\mu = 0$) will be presented.

The plaquette value is just one observable which signals different phases. To examine the properties of these, we also measured the pion mass and the quark mass on configurations with either high or low plaquette values separately. See Tab. 5.9 for the points we considered; a detailed description how to measure these quantities in the presence of a twisted mass term has been given in Sec. 2.4. The pion mass also shows the metastability: Fig. 5.10, left panel. A remarkable result is provided by the quark mass am_χ^{PCAC}, which measures the untwisted component of the mass parameter: the two phases correspond to positive (low plaquette phase) and negative (high plaquette phase) values of the quark mass: Fig. 5.10, middle panel. Without a metastable region, one would have expect $am_\chi^{\text{PCAC}} \propto \mu_\kappa$, vanishing at some unique critical value. The numerical data support such a behavior only for each of the two branches separately, leading to different critical values. Plotting the pion mass squared vs. the PCAC-quark mass, Fig. 5.10, right panel, the tree-level χPT assumption $am_\pi^2 \propto |am_\chi^{\text{PCAC}}|$ turns out to be valid.

From the Sommer-scale parameter the lattice spacing is evaluated to be $a \approx 0.20\,\text{fm}$ in the low plaquette phase (positive quark mass) and $a \approx 0.12\,\text{fm}$ in the phase with high plaquette values (negative quark mass). These values have to be taken with some care, especially the latter one. Our statistics in this exploratory runs was clearly not high enough to determine r_0/a for such fine lattice spacings, since one has to know the Wilson-loops up to an extension of 4 or even 5 with a good precision. But using these estimates the minimal pion mass becomes roughly 415 MeV (positive quark mass) and 685 MeV (negative quark mass). From the point of view to reach physical pion masses of the order

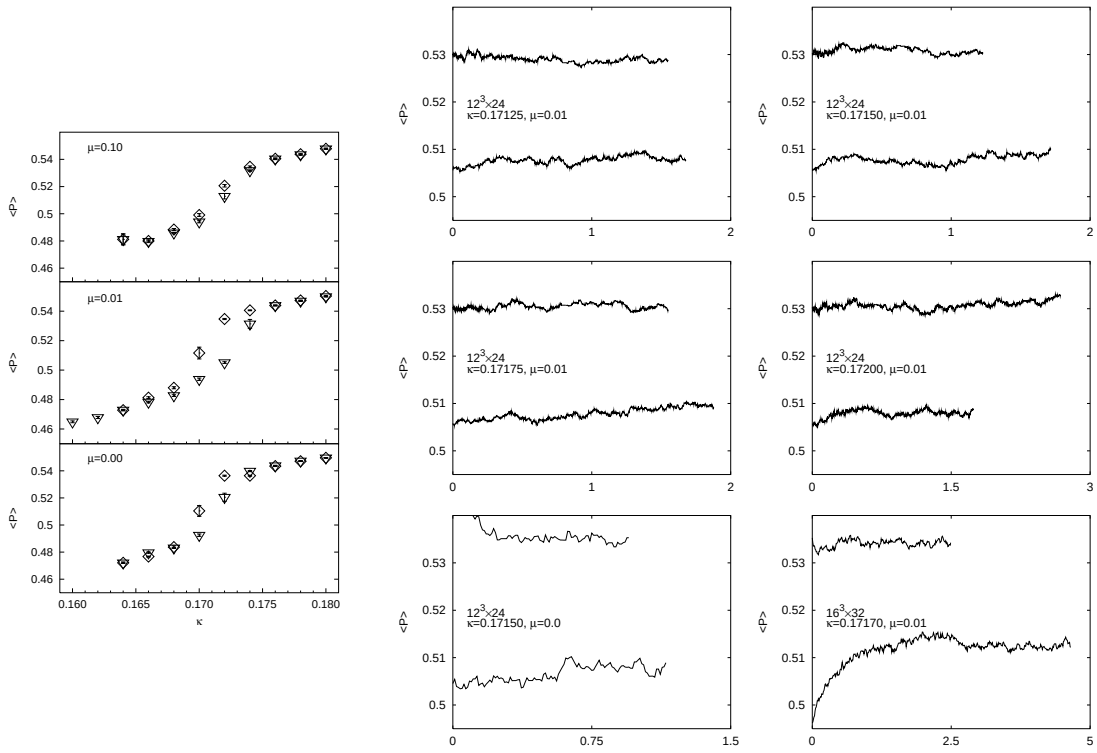

Figure 5.9: Left panel: *Thermal cycles in κ on $8^3 \times 16$-lattices at $\beta = 5.20$ with different values for μ. Shown is the expectation value of the average plaquette $\langle P \rangle$. The triangles (∇) refer to increasing, the diamonds ($\diamond$) to decreasing κ-values, respectively.* Right panel: *Plaquette history of different runs with $\beta = 5.2$, showing the metastabilities. The number of sweeps is given in thousands.*

of 140 MeV, this looks very disappointing. Of course, due to the presence of the twisted mass term, the pion mass never will reach zero. Given the situation that its mass would exclusively originate from $\mu = a\mu' = 0.01$, the lowest possible value should be of the order $m_\pi \approx 230\,\mathrm{MeV}$ (positive quark mass). This estimate comes from the tree-level χPT estimate $m_\pi^2 \approx 2B_0\mu'$, with $r_0 B_0 \approx 7.0$ [122]. The minimal values which could be reached in our simulations are by a factor of almost two larger. We will show later that improved gauge actions can help to lower the minimal pion masses. Going to finer lattice spacings and/or larger volume also may allow reaching lighter pions—at higher numerical cost. This point is still under numerical investigation by our collaboration.

The existence of a first order phase transition is predicted by the normal scenario, where for sufficiently small values of μ the condensate $\langle \bar{\chi}\chi \rangle$ changes sign discontinuously. Considering an operator expansion based on the lattice symmetries of the local plaquette [33]

$$U_{\mu\nu}(x) \;=\; [b_0 \mathbb{1} + b_{4g} a^4 F \cdot F] + b_3 a^3 \langle \bar{\chi}\chi \rangle + b_{4\mu} a^4 \mu \langle \bar{\chi} i\gamma_5 \tau_3 \chi \rangle + \mathcal{O}_{a^5} \tag{5.82}$$

(here $\mathcal{O}_{a^5}$ means operators of lattice dimension 5 and higher), one can relate the jump in the plaquette expectation value to the one in the condensate.

The occurrence of the metastable region can be explained on a microscopic level by the features of the eigenvalue spectrum. Let us first consider the case for the untwisted Wilson-

$L \times T$	phase	κ
$12^3 \times 24$	low	$0.17125, 0.17150, 0.17175$
	high	$0.17125, 0.17150, 0.17175, 0.17250$
$16^3 \times 32$	low	$0.1700, 0.1710, 0.1717$
	high	$0.1717, 0.1720$

Table 5.9: *κ-values for the runs performed at $\beta = 5.20$, $\mu = 0.01$, on two different lattice sizes. Both, the TSMB- and the HMC-algorithm were used. The column "phase" denotes if the runs thermalized in a low or high average plaquette expectation value (started from a disordered or ordered configuration).*

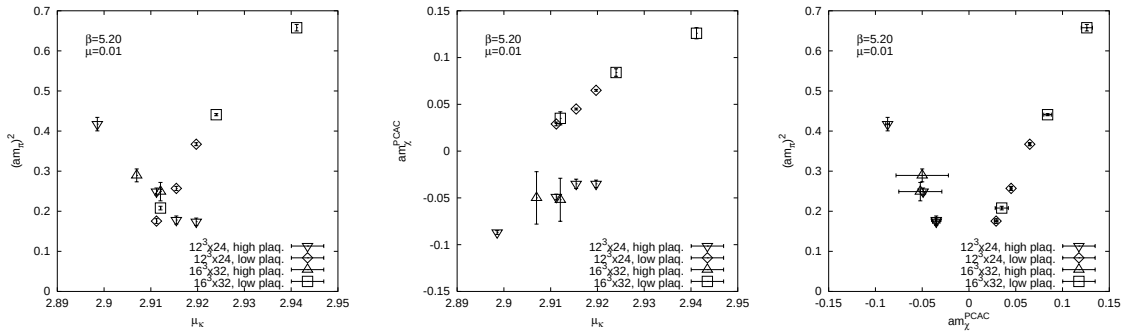

Figure 5.10: *Results from the runs specified in Tab. 5.9.* Left panel: *pion mass squared vs. μ_κ.* Middle panel: *PCAC quark mass vs. μ_κ.* Right panel: *pion mass squared vs. PCAC quark mass.*

Dirac operator. Its eigenvalue spectrum has been studied in [19]: for small positive quark masses there is a "cloud" of eigenvalues close to the origin near the positive real axis. When passing through the critical value of the quark mass parameter and therefore going to negative quark masses, this cloud has to move towards eigenvalues with negative real part. This transition has to take place near the origin, where the determinant of the fermion matrix is zero. The latter is the reason why this transition is highly suppressed by the fermionic part of the action. This *eigenvalue cloud crossing* and its suppression can be seen as a reason for the strong metastabilities. Adding the twisted mass term to the action forbids the strip $\mathrm{Im}\lambda \in [-\mu, \mu]$ to be filled with eigenvalues (λ). With increasing values of the twisted mass parameter μ the eigenvalue cloud crossing happens at larger distance from the origin and is less suppressed. At a sufficiently high value of μ the metastability therefore should disappear, as does the first order phase transition line in the normal scenario (Fig. 3.2, lower panel).

We looked at the eigenvalue spectra of several runs with and without the twisted mass term performed with the DBW2 gauge action (for details on the runs see next section). The eigenvalue spectrum of the Wilson-Dirac operator was obtained by using the Arnoldi-method on typically 10–30 independent gauge configurations, searching for 100–200 eigenvalues with smallest absolute values. Figs. 5.11.1–5.11.4 show the spectra on $L^3 \times T = 8^3 \times 16$ lattices without a twisted mass term. Here no metastability was found.

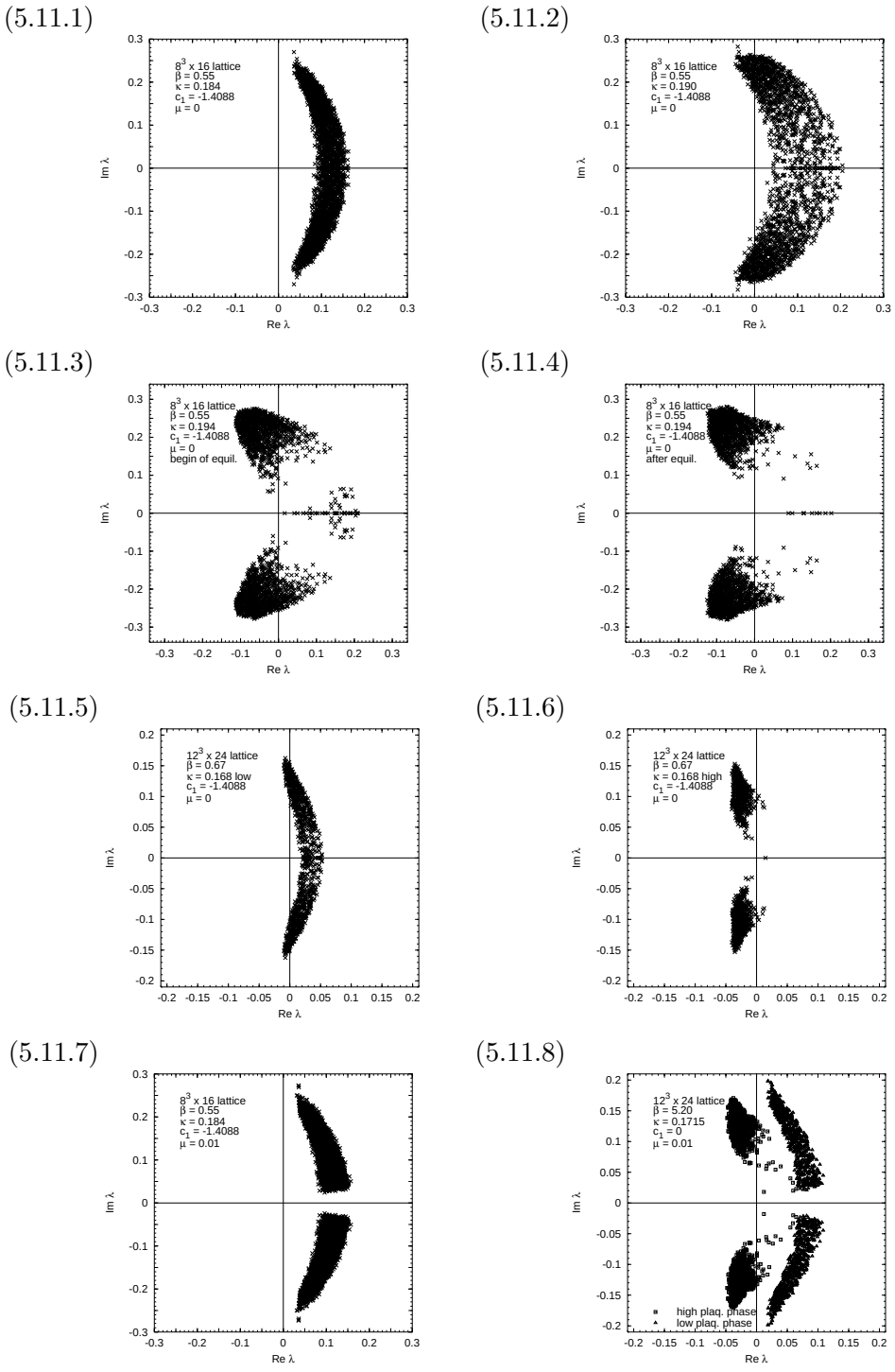

Figure 5.11: *Eigenvalue spectra of the Wilson-Dirac matrix at different parameter settings, with DBW2 gauge action (1-7) and Wilson plaquette gauge action (8).*

The change from positive (Figs. 5.11.1, 2) to negative quark masses (Figs. 5.11.3, 4) is nicely illustrated: the half moons at positive quark masses get emptied around the positive real axis, while the total spectrum moves towards values with negative real parts.

Fig. 5.11.3 is taken at the beginning of equilibration, which has been reached in Fig. 5.11.4. Figs. 5.11.5 and 6 show a situation on a $12^3 \times 24$-lattice, $\mu = 0$, where a metastability occurs. Both spectra are taken at the same κ-value, but differ in the (sign of the) quark mass: here the suppression of the eigenvalue cloud crossing results in the metastable branches. Figs. 5.11.7, 8 depict the situation with $\mu \neq 0$ (the latter was generated with Wilson plaquette gauge action, referring to the preceding discussion). The empty strip of width 2μ around the real-axis is visible. Fig. 5.11.8 shows both phases in a metastable region. The suppression by the twisted mass term of the suppression of the eigenvalue cloud crossing near the origin due to the fermionic determinant is not strong enough to avoid metastable branches.

5.3.2 Improved gauge actions

Changing the gauge part of the action influences the phase structure: as mentioned before, [65] reported on a bulk phase transition for $N_f = 3$ Clover-improved Wilson fermions with Wilson plaquette gauge action. This transition disappeared if an improved gauge action was used instead. Reducing the lattice discretization error by changing the gauge action leads to a different value for c_2 (Eq. (3.35)) in the Sharpe-Singleton ansatz to describe the phase structure scenarios.

We decided to use the DBW2 gauge action, which should be improved due to renormalization group arguments (cf. App. B). The phase transition should weaken with this set-up, which should also allow for reaching a lower minimal pion mass. We will examine both, the untwisted and twisted Wilson fermion action in conjunction with this gauge action. As a byproduct of the untwisted runs, we also obtained chiral fits for the pion mass squared and decay constant dependence on the quark mass, reported already in Sec. 5.2.3.

Two lattice sizes, $L^3 \times T = 8^3 \times 16$ and $12^3 \times 24$, have been used for examining the phase structure. The gauge couplings were tuned to $\beta = 0.55$ and $\beta = 0.67$, respectively. These values were chosen such, that the $12^3 \times 24$-lattices had roughly a lattice spacing of $a \simeq 0.18 - 0.21$fm in the positive quark mass phase ($a \simeq 0.16 - 0.18$fm at negative quark mass), which corresponds to the situation discussed in the previous section at $\beta = 5.2$ for Wilson plaquette gauge action. Therefore, a comparison with the previous data is justified. The $8^3 \times 16$-lattices are tuned to give the same (physical) volume but coarser lattice spacing. The κ-values we simulated are reported in Tab. 5.10, together with the measured results for the pion mass, rho mass, the ratio of the latter two, and the PCAC quark mass. The twisted mass parameter was set to zero in all the $8^3 \times 16$-runs, $(a) - (g)$, and the $12^3 \times 24$-runs $(A) - (G)$, while $\mu = 0.01$ in runs $(\mathcal{A}) - (\mathcal{E})$.

$L^3 \times T = 8^3 \times 16, \beta = 0.55$

On this coarse lattices no signs of metastability could be found. Plotting the pion mass squared vs. μ_κ (Fig. 5.12, left panel) indicates the possibility of a small region of an Aoki phase ($\mu_\kappa \in [2.62, 2.63] \Leftrightarrow \kappa \in [0.190, 0.191]$), where the (charged) pion mass should vanish. This is in accordance with the findings of [25] for such a strong gauge coupling, since this lattice spacing corresponds to values of $\beta \approx 4.6$ for Wilson plaquette gauge action (compare, e.g., with run I from Sec. 5.2). The quark mass dependence on μ_κ (Fig. 5.12, right panel) also suggests such a conclusion.

	κ	am_π	am_ρ	m_π/m_ρ	am_χ^{PCAC}
(a)	0.184	0.6962(69)	1.0015(75)	0.6952(37)	0.07086(85)
(b)	0.186	0.5325(60)	0.9013(75)	0.5908(57)	0.03890(75)
(c)	0.188	0.3652(49)	0.840(26)	0.435(13)	0.0154(10)
(d)	0.190	0.081(24)	0.62(38)	0.130(78)	0.0012(15)
(e)	0.192	0.594(51)	1.80(30)	0.355(42)	−0.0430(70)
(f)	0.193	0.888(19)	1.794(30)	0.495(13)	−0.0870(38)
(g)	0.194	0.997(23)	1.820(59)	0.548(17)	−0.0995(66)
(A_l)	0.165	0.454(04)	0.724(25)	0.627(18)	0.0414(05)
(C_l)	0.167	0.343(07)	0.735(32)	0.466(21)	0.0222(11)
(C_h)	0.167	0.313(22)	0.776(125)	0.403(67)	−0.0222(28)
(D_l)	0.168	0.153(12)	0.445(109)	0.344(91)	0.0053(17)
(D_h)	0.168	0.380(31)	1.144(88)	0.332(37)	−0.0335(54)
(E_h)	0.170	0.644(15)	1.324(75)	0.487(27)	−0.0834(38)
(F_h)	0.172	0.840(23)	1.468(52)	0.572(25)	−0.1295(77)
(G_h)	0.175	1.005(44)	1.801(81)	0.558(28)	−0.1585(103)
$(\mathcal{A}_\mathrm{l})$	0.165	0.4641(45)	0.7228(58)	0.6421(53)	0.03803(81)
$(\mathcal{B}_\mathrm{l})$	0.166	0.341(05)	0.634(55)	0.538(45)	0.0177(22)
$(\mathcal{C}_\mathrm{h})$	0.167	0.291(12)	0.607(232)	0.480(178)	−0.0149(22)
$(\mathcal{D}_\mathrm{h})$	0.168	0.472(07)	1.035(72)	0.456(32)	−0.0469(16)
$(\mathcal{E}_\mathrm{h})$	0.170	0.712(14)	1.136(65)	0.627(34)	−0.0946(72)

Table 5.10: *Runs performed with the DBW2 gauge action at $L^3\times T = 8^3\times 16$ (small letters, $\beta = 0.55$), and $12^3 \times 24$ lattices (capital letters, $\beta = 0.67$). For all the runs the twisted mass parameter was set to zero, except for those with a calligraphic letter, where $\mu = 0.01$. The suffix "l" and "h" denote phases with a low and high plaquette value, respectively. The TSMB-algorithm was used to generate the configurations (typical number of configurations at one point ≈ 100). The results for the pion mass, rho mass, m_π/m_ρ, and the PCAC quark mass are given, too.*

$L^3 \times T = 12^3 \times 24, \beta = 0.67$

At the finer lattices the situation changes: while for $\mu = 0.01$ still no metastability occurs, in the untwisted case the plaquette expectation values (Fig. 5.13) again show a behavior similar to the case with Wilson plaquette gauge action. Nevertheless, the magnitude of the gap is much smaller compared to that found with Wilson plaquette gauge action ($\beta = 5.2$). With DBW2 gauge action ($\beta = 0.67$) it is ≈ 0.008 at higher absolute values for $\langle P\rangle$. The plots for the pion masses and quark masses at $\mu = 0$ (Fig. 5.14) are comparable, too. The different branches are related to positive and negative quark masses. A value for the minimal pion mass in a stable situation can be estimated in the following way: fitting the low and high plaquette value points separately with the tree-level χPT-ansatz, the minimum is determined by the intersection of these two lines, as indicated in the plot (Fig. 5.14, left panel). The value of $(am_\pi)^2_{\mathrm{min}} = 0.0881$ corresponds to $m_\pi^{\mathrm{min}} \approx 251\,\mathrm{MeV}$ (positive quark mass phase) or $m_\pi^{\mathrm{min}} \approx 374\,\mathrm{MeV}$ (negative quark mass phase). The PCAC quark mass dependence on μ_κ allows for determining the critical value of the latter. Obviously the metastability near the first order phase transition results in different

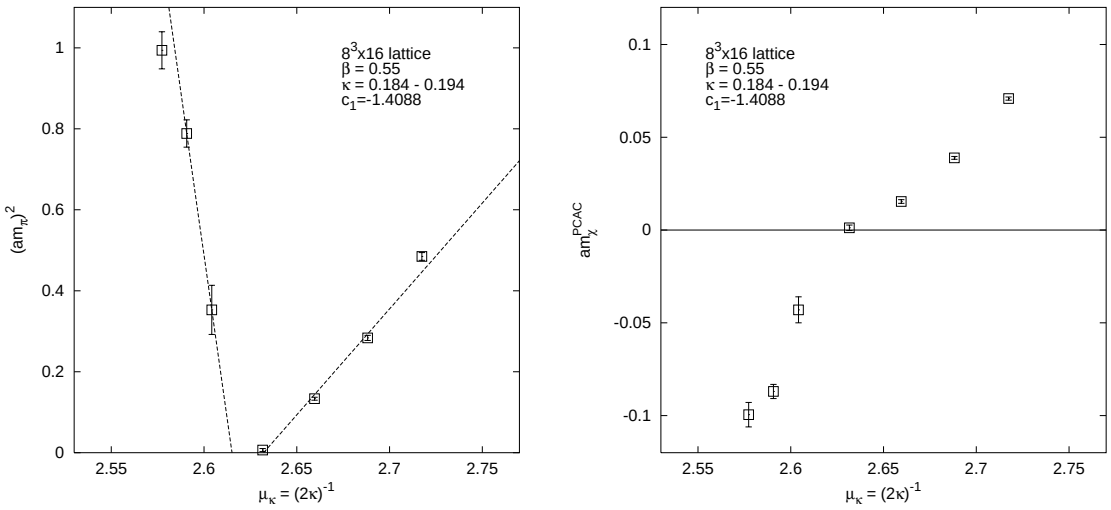

Figure 5.12: Left panel: *pion mass squared vs. μ_κ for runs $(a)-(g)$. The branches with positive and negative quark mass are fitted separately with a linear function.* Right panel: *PCAC quark mass vs. μ_κ for runs $(a)-(g)$.*

values for κ_{crit} from the two branches, as shown by the plot (Fig. 5.14, right panel).

With a non-zero value for the twisted mass parameter, the metastability disappeared, as has been seen already from the plaquette expectation value. Fig. 5.15 shows the pion mass squared and the PCAC quark mass vs. μ_κ. In the latter plot three different linear fits are included to estimate κ_{crit}: the solid line is fitting the whole range, while the other two fits (dashed lines) are restricted to points with either positive or negative quark mass. Although the latter fits differ, the overall fit describes the situation reasonably well. The interval of $\kappa_{\text{crit}} \in [0.1664, 0.1669]$ is substantially smaller compared to the untwisted case ($[0.1661, 0.1689]$), where, of course, a satisfactory overall fit could not be performed. Because no metastability occurred, it should be possible to reach the point, where the pion mass is totally given by the twisted component. We will turn to this in Sec. 5.3.3. Determining κ_{crit} from the twist angle as has been argued in Sec. 2.2 can be done by fitting ω_V to its expected dependence on μ_κ (Fig. 5.16). One finds consistently $\kappa_{\text{crit}} = 0.16651(2)$.

In both cases (untwisted and twisted fermion action) plotting the squared pion mass versus the untwisted bare quark mass parameter μ_κ, one encounters different slopes in the branches with positive and negative quark mass values. As has been pointed out by S.R. Sharpe [123] this can be understood on the basis of the lattice χPT formula for the pion mass squared dependence on the quark mass (cf. [34]) as an $\mathcal{O}(a)$ effect. Therefore, one may use the difference of the slopes to estimate the size of lattice artifacts. Plotting the pion mass squared in physical units versus the PCAC quark mass (Fig. 5.17), we determined the two slopes in the untwisted case. For the twisted case, one should keep in mind, that at $am_\chi^{\text{PCAC}} = 0$ the pion mass is still non-zero, because $\mu \neq 0$.

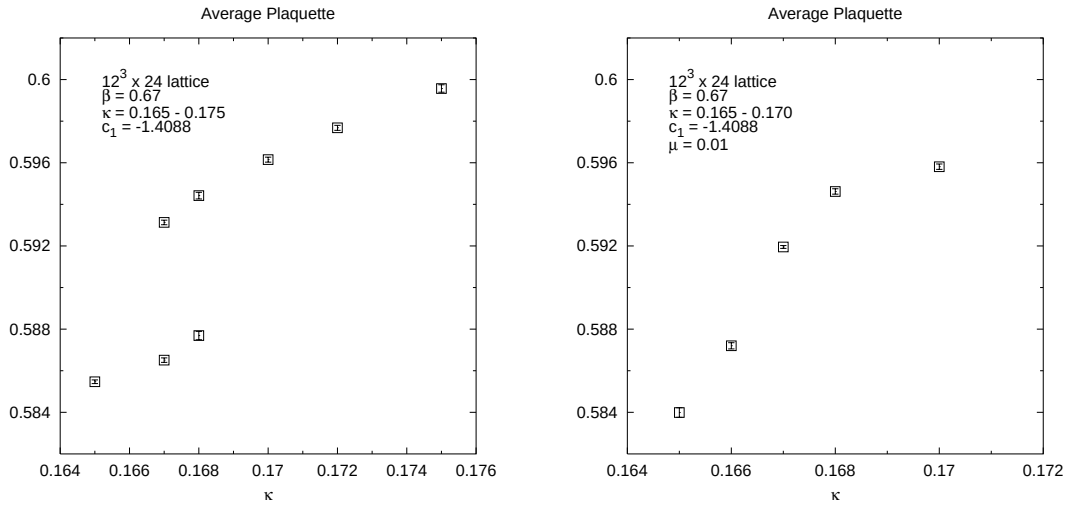

Figure 5.13: *Average plaquette expectation values for the* $L^3 \times T = 12^3 \times 24$ *runs.* Left panel: *without twisted mass, runs* $(A) - (G)$. Right panel: with $\mu = 0.01$, *runs* $(\mathcal{A}) - (\mathcal{E})$.

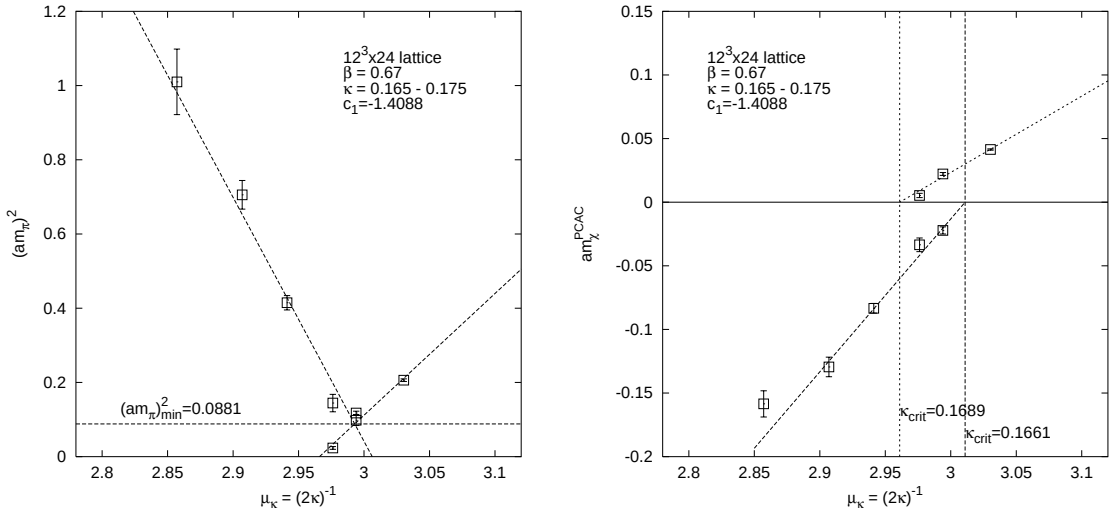

Figure 5.14: $L^3 \times T = 12^3 \times 24$ *lattices without twisted mass (runs* $(A) - (G)$*).* Left panel: *pion mass squared vs.* μ_κ*. Also shown are the separate linear fits leading to an estimate for the minimal pion mass (see text).* Right panel: *PCAC quark mass vs.* μ_κ*, with separate linear fits to determine* κ_{crit} *in the two phases.*

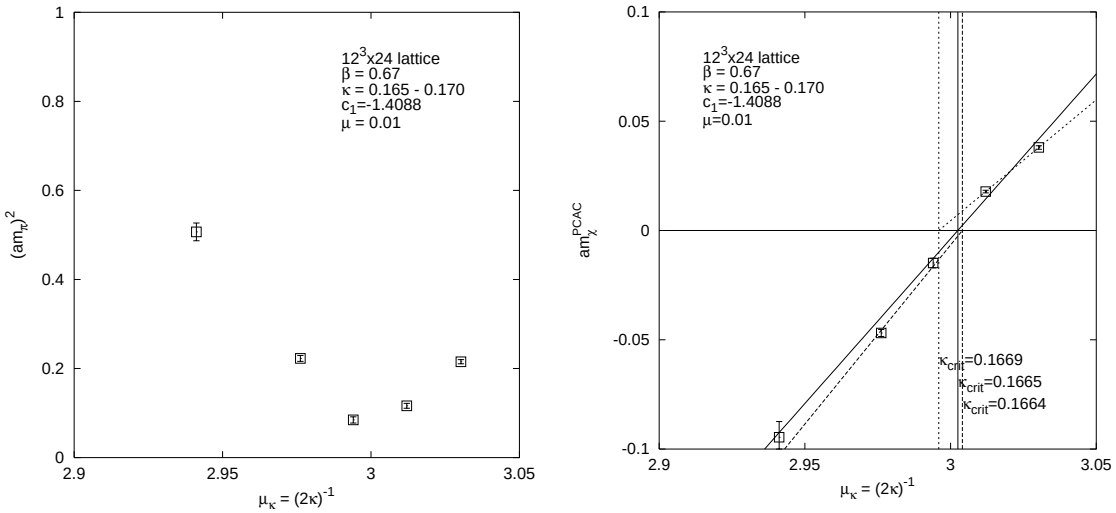

Figure 5.15: $L^3 \times T = 12^3 \times 24$ *lattices with* $\mu = 0.01$ *(runs* $(\mathcal{A}) - (\mathcal{E})$*).* Left panel: *pion mass squared vs.* μ_κ*.* Right panel: *PCAC quark mass vs.* μ_κ*, with three separate linear fits to determine* κ_{crit}*: The solid line is a fit to all points, while the dashed ones only include either the points with positive or negative quark masses.*

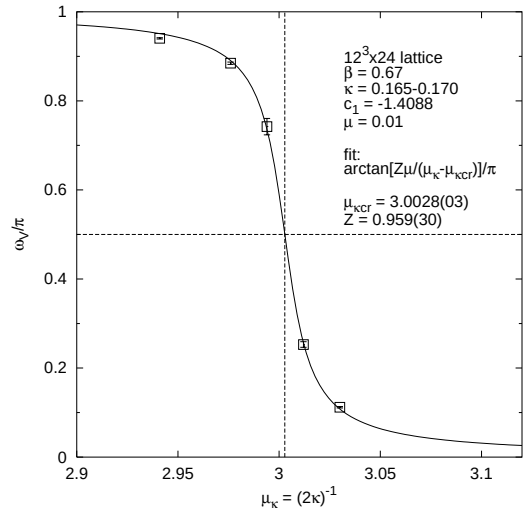

Figure 5.16: ω_V/π *as a function of the bare untwisted quark mass parameter* μ_κ *for runs* $(\mathcal{A}) - (\mathcal{E})$*. The fit to the expected* arctan*-dependence determines* $\kappa_{crit} = 0.16651(2)$*, where* $\omega_V = \pi/2$ *(maximal twist).*

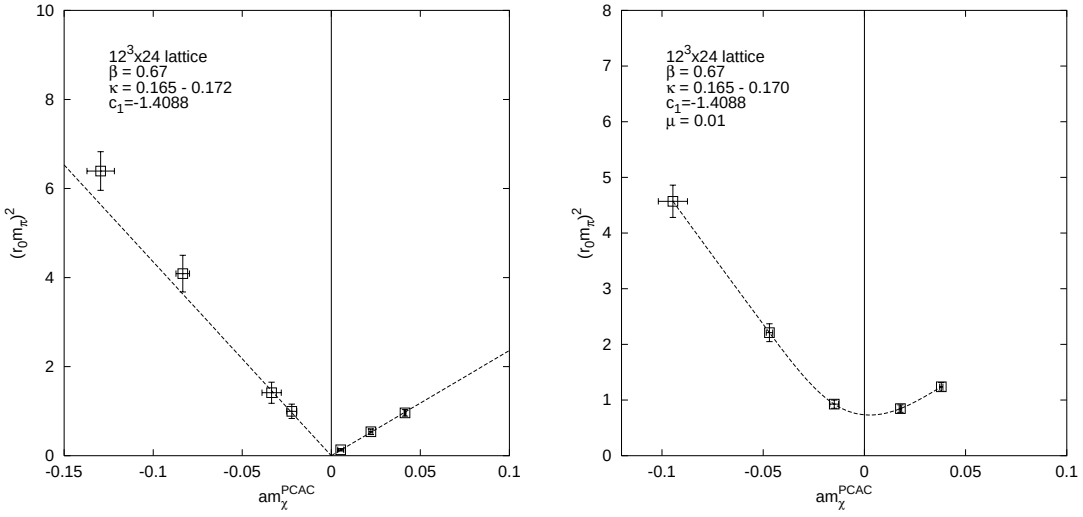

Figure 5.17: *Pion mass squared in physical units of r_0 vs. the PCAC quark mass for the $12^3 \times 24$-lattices.* Left panel: *without twisted mass. Each branch is fitted separately to $(r_0 m_\pi)^2 = C|am_\chi^{PCAC}|$, resulting in $C_+ = 23.6$, and $C_- = 43.5$, fits shown by dashed lines.* Right panel: $\mu = 0.01$. *The dashed line just connects the points by a spline interpolation to guide the eyes.*

Numerical cost for twisted and untwisted DBW2-simulations

To estimate the numerical cost dependence on the quark mass, we give in Tab. 5.11 the algorithmic parameters for the $L^3 \times T = 12^3 \times 24$ simulations with and without a twisted mass term, runs $(A)-(G)$ and $(\mathcal{A})-(\mathcal{E})$, respectively. Assuming a dependence like the one found in the case with Wilson plaquette gauge action, Eq. (5.54) with $z \approx 2$, the obtained values for $F_{\rm plaq}$ and F_{m_π} are quoted in the table, too, giving the cost in FLOP. Let us first concentrate on the untwisted simulations. It becomes clear, that runs performed in the negative quark mass phase (high plaquette value) are more expensive compared to positive quark mass runs. The values $F_{\rm plaq} \simeq (0.1 \sim 0.8) \cdot 10^6$ and $F_{m_\pi} \simeq (0.01 \sim 0.3) \cdot 10^6$ in the positive quark mass phase are roughly a factor of 10 smaller than with Wilson plaquette gauge action, Eq. (5.55). A better description of the situation is achieved assuming $z \approx 1$, since now the factors are much more stable: $F_{\rm plaq} \simeq 2 \cdot 10^7$ and $F_{\rm plaq} \simeq (2 \sim 3) \cdot 10^8$ for positive and negative quark mass phase, respectively.

Considering the twisted mass runs, $(\mathcal{A})-(\mathcal{E})$, we first remark that the polynomial degrees could be chosen smaller, because two fermion fields are included in the fermion matrix and therefore the exponent of the latter in Eq. (5.20) is just half the value compared to the untwisted case. On the contrary, one twisted MVM is twice as costly if compared to an untwisted MVM. The so obtained values for the cost-constants F are comparable to the previous ones from untwisted runs. But one still has to keep in mind that for the quark mass entering the cost formula $am_\chi^{\rm PCAC}$ has been taken, measuring the untwisted component only. Assuming like above $z \approx 1$, a better description is achieved, too. The obtained values for $F_{\rm plaq}$ are to lay between $1 \cdot 10^7$ and $2 \cdot 10^8$.

The above discussion of the numerical cost covers the case of the TSMB-algorithm only.

	n_1	n_2	n_3	$[\epsilon, \lambda]$	$\frac{N_{\mathrm{MVM}}}{10^3\,\mathrm{cycle}}$	$\tau_{\mathrm{int}}^{\mathrm{plaq}}$	$\tau_{\mathrm{int}}^{m_\pi}$	$\frac{F_{\mathrm{plaq}}}{10^6}$	$\frac{F_{m_\pi}}{10^6}$
(A_{l})	28	210	220	$[1.3 \cdot 10^{-3}, 26]$	19	21	< 5	0.8	< 0.2
(C_{l})	28	500	510	$[1.3 \cdot 10^{-4}, 25]$	29	18	15	0.3	0.3
(D_{l})	30	1100	1200	$[1.2 \cdot 10^{-5}, 25]$	51	77	< 5	0.1	< 0.01
(C_{h})	30	1100	1200	$[1.3 \cdot 10^{-5}, 25]$	50	53	33	1.5	0.9
(D_{h})	30	1100	1200	$[1.2 \cdot 10^{-5}, 25]$	51	113	7	7.8	0.5
(E_{h})	28	900	920	$[4.8 \cdot 10^{-5}, 24]$	43	61	11	22.0	3.9
(F_{h})	28	500	510	$[1.2 \cdot 10^{-4}, 24]$	30	56	< 5	33.4	< 3.0
(G_{h})	28	500	510	$[1.1 \cdot 10^{-4}, 23]$	31	52	6	48.4	5.6
$(\mathcal{A}_{\mathrm{l}})$	16	250	270	$[1.2 \cdot 10^{-3}, 24]$	12	143	13	5.9	0.5
$(\mathcal{B}_{\mathrm{l}})$	18	420	460	$[3.6 \cdot 10^{-4}, 24]$	21	41	9	0.6	0.1
$(\mathcal{C}_{\mathrm{h}})$	18	420	460	$[3.6 \cdot 10^{-4}, 24]$	21	22	6	0.2	0.1
$(\mathcal{D}_{\mathrm{h}})$	18	420	460	$[3.6 \cdot 10^{-4}, 24]$	21	72	8	7.8	0.9
$(\mathcal{E}_{\mathrm{h}})$	18	420	460	$[3.6 \cdot 10^{-4}, 24]$	21	29	7	12.8	3.1

Table 5.11: *Algorithmic parameters for the $L^3 \times T = 12^3 \times 24$ runs using the DBW2 gauge action. $n_{1,2,3}$ are the polynomial orders, for all runs a determinant breakup with $n_b = 4$ has been applied. The approximated interval is given by $[\epsilon, \lambda]$. N_{MVM} are the cost in MVM needed for one update cycle in this set-up. The τ_{int} give the integrated autocorrelation lengths for the plaquette and m_π in update cycles, in some cases only an upper bound could be given, because the stored configurations were independent. The cost factors F are explained in the text. Note that the positive quark masses (index "l") decrease with increasing letters, while for negative quark masses (index "h") they increase.*

During our comparison with the HMC-algorithm it turned out that the use of the latter is advantageous especially in the thermalization phase. The equilibrium is reached much faster. Also at intermediate small quark masses the HMC-algorithm is up to a factor of 10 less expensive (comparing directly the number of FLOP required for the production of one independent gauge configuration). One drawback of the HMC is that only an even number of fermions can be described. Simulating odd numbers of fermions requires modifications, as for instance using PHMC (polynomial HMC) algorithms [124, 125, 126]. The same consideration applies, if twisted mass fermions with mass-non-degenerate fermions are to be simulated ($\mu_\Delta \neq 0$), which is referred to as the *split-doublet* case.

Summary

Based on the total of our findings we propose the phase structure picture for $N_f = 2$ lattice QCD (at zero temperature) with Wilson fermions as announced in Sec. 3.3, shown by Fig. 3.3. At strong bare gauge coupling an Aoki phase situation is realized which ends at some coupling β_1. This means a shrinking of the Aoki phase to first order phase transition lines in the μ_κ-μ plane (i.e., a first order phase transition point in the β-μ_κ plane). Also this picture suggests that there should be a situation where there is just a first order phase transition point in the full three-parameter space, corresponding to $c_2 = \mathcal{O}(a^3)$ in the Sharpe-Singleton ansatz. Such a point could be found by tuning the free parameter in the improved gauge action to an almost ideal situation. Nevertheless, it is worth to consider other commonly used improved gauge actions, like the Iwasaki RG- or

the Symanzik tree-level improved gauge action. Before starting a large set of simulations with the aim of extracting physically relevant parameters near a realistic low pion mass, the gauge action should be tuned optimal. The results presented for the DBW2 gauge action already look promising, since pion masses of the order of ≈ 250 MeV already have been reached. But this gauge action has other disadvantages which have been discussed in the literature. One concern is about the sampling of the topological charge in the produced gauge configuration ensembles. The RG-improved gauge actions are known to slow down the transition between sectors with different topological charges. At least for the TSMB-algorithm it has been checked that the different sectors are sampled in a reasonable way, for details we refer to the discussion on this point in [33]. Another fact is that RG-improved gauge actions lead to a non-positive transfer matrix due to lattice artifacts. The latter afflicts the extraction of masses and matrix elements from the correlators. Using the described smearing techniques plus a randomly chosen source point for computing the correlators, we did not encounter any difficulties related to this problem. Another more serious doubt has been pointed out by [127]. There lattice perturbation theory was considered to determine renormalization factors perturbatively with the help of a tadpole improvement ansatz in the case different gauge being applied. For the RG-improved gauge actions a slow convergence of the perturbative series compared to tree-level improved gauge actions was suggested. Also it is known that DBW2 and Iwasaki-gauge actions are "over-corrected" at tree-level [14, 13] unless small enough values of a/r_0 are reached. Because of the afore mentioned reasons a study similar to the one we presented for the DBW2 gauge action now using the Symanzik tree-level improved gauge action would be helpful. If the metastabilities are weakened by that particular gauge action, too, allowing for comparable small pion masses as found with the DBW2 gauge action, one should prefer to use the Symanzik tree-level improved gauge action for future simulations. The main result remains valid, namely that the use of improved gauge actions is substantial if small quark masses are to be simulated.

The numerical cost for the TSMB-algorithm turned out to be comparable to previous findings without a twisted mass term. The HMC-algorithm showed a better performance but will require further modifications, if odd numbers of fermions or split-doublets are to be treated. These include the more realistic $N_f = 2 + 1$ case, i.e., two mass degenerate light fermions and a heavier one to simulate the up and down quarks as degenerate flavors plus the strange quark. Both odd number of fermions and the split-doublet are already implemented for the TSMB-algorithm (cf. Sec. 5.1.2 and App. C.1). The experience we gained in using the TSMB-algorithm with twisted fermions and different gauge actions will be useful for the interesting application to perform simulations with the twisted mass formulation and $N_f = 2 + (1 + 1)$. Here a degenerate doublet of twisted light fermions will represent the up and down quarks, while the second heavier doublet is split into the strange and charm quark. The inclusion of the charm quark is not necessary from the χPT point of view. Therefore, one may also choose the mass-splitting in such a way that the charm quark receives a mass of the order of the lattice cut-off to effectively remove it. In this case, however, no automatic $\mathcal{O}(a)$ improvement can be expected.

5.3.3 Z-factors and pion decay constant from QCD$^{\mathrm{TM}}$-simulations

In this section we will show how to extract information about the renormalization factors and the pion decay constant from simulations using QCD$^{\mathrm{TM}}$ (here together with the DBW2

κ	ω_V/π	ω_A/π	ω/π	Z_A/Z_V	Z_V
0.1650	0.1350(13)	0.0574(32)	0.0889(24)	1.575(46)	0.59096(42)
0.1655	0.1767(28)	0.0796(39)	0.1205(31)	1.560(40)	0.58165(37)
0.1660	0.241(6)	0.129(6)	0.1807(42)	1.484(38)	0.57616(35)
0.1665	0.411(12)	0.247(24)	0.342(18)	1.90(16)	0.56931(29)
0.1670	0.677(12)	0.626(41)	0.649(26)	0.83(15)	0.57037(48)
0.1675	0.805(9)	0.72(8)	0.77(5)	0.84(19)	0.5706(10)
0.1680	0.8711(43)	0.87(9)	0.87(6)	1.04(10)	0.5856(11)

Table 5.12: *Results for the different twist angles, Z_A/Z_V, and Z_V in the runs performed with the HMC-algorithm, $L^3 \times T = 12^3 \times 24$, $\beta = 0.67$ (DBW2), $\mu = 0.01$. In each point ≈ 500 configurations were produced and analyzed. For details on the extraction of the quantities, see text.*

gauge action). Again we performed runs at $L^3 \times T = 12^3 \times 24$, $\beta = 0.67$, and $\mu = 0.01$, i.e., similar to the runs $(\mathcal{A}) - (\mathcal{E})$ of the previous section, but this time using the HMC-algorithm and producing ≈ 500 configurations at each point. The hopping parameters were chosen to lay in the range $\kappa \in [0.1650, 0.1680]$, with a step-size $\Delta\kappa = 0.0005$. This resulted in four points with positive and three with negative quark mass. In Fig. 5.18 we show the average plaquette expectation value, the pion mass squared, and the PCAC-quark mass as functions of κ or μ_κ. Also shown is the dependence of $(r_0 m_\pi)^2$ on am_χ^{PCAC}. The values agree with the previously found ones, confirming therefore the TSMB-algorithm based results. From $M_{r_0} = (r_0 m_\pi)^2$ the range of quark masses is roughly $1/5 - 2/5\, m_s$ for positive quark masses (negative: $1/3 - 2/3\, m_s$). The minimal pion mass was reached at $\kappa = 0.1665$, there $r_0 m_\pi = 0.801(16)$ giving $m_\pi = 316(6)\,\mathrm{MeV}$. With the value of r_0/a measured at that point the estimate for the pion mass given exclusively by the twisted mass $\mu = 0.01$ is $m_\pi \approx 250\,\mathrm{MeV}$. Taking also $am_\chi^{\mathrm{PCAC}} = 0.00505(82) \approx \mu/2$ at $\kappa = 0.1665$ into account, one would have expect $m_\pi \approx \sqrt[4]{1 + (1/2)^2}\, 250\mathrm{MeV} \approx 264\mathrm{MeV}$. The roughly 16% difference shows both the influence of lattice artifacts as well as the uncertainty arising from neglecting the renormalization factors.

The twist angles ω_V and ω_A have been measured according to the parity-conservation based method described in Sec. 2.4.1, Eqs. (2.80), (2.81). Results are reported in Tab. 5.12. There also the values for ω are quoted, obtained from ω_V and ω_A according to Eq. (2.77), and the ratio of normalization factors Z_A/Z_V coming from Eq. (2.82). The value for Z_V is calculated with the help of the conserved vector current, Eq. (2.83).

First we fitted the twist angle dependence on the bare quark mass, Fig. 5.19, to a function

$$\omega_X \;=\; \arctan\left[Z_{\omega_X} \frac{\mu}{\mu_\kappa - \mu_{\kappa\mathrm{crit}}} \right], \tag{5.83}$$

where Z_{ω_X} and $\mu_{\kappa\mathrm{crit}}$ were treated as free parameters. Fitting the different angles independently resulted in slightly different values for the critical value of the bare untwisted quark mass parameter in the range of $\mu_{\kappa\mathrm{crit}} = 3.00108(95)$ (from ω_V, fit shown by Fig. 5.19, right panel) to $\mu_{\kappa\mathrm{crit}} = 2.99672(54)$ (from ω_A, fit not shown). By definition all the three angles have to assume maximal twist at the same $\mu_{\kappa\mathrm{crit}}$. Therefore, we decided to take $\mu_{\kappa\mathrm{crit}}$ and Z_ω from a two-parameter-fit using ω, and fixing $\mu_{\kappa\mathrm{crit}}$ in the remaining fits for ω_V, ω_A to obtain the other two Z-factors. The fits are shown by Fig. 5.19, left panel. As one

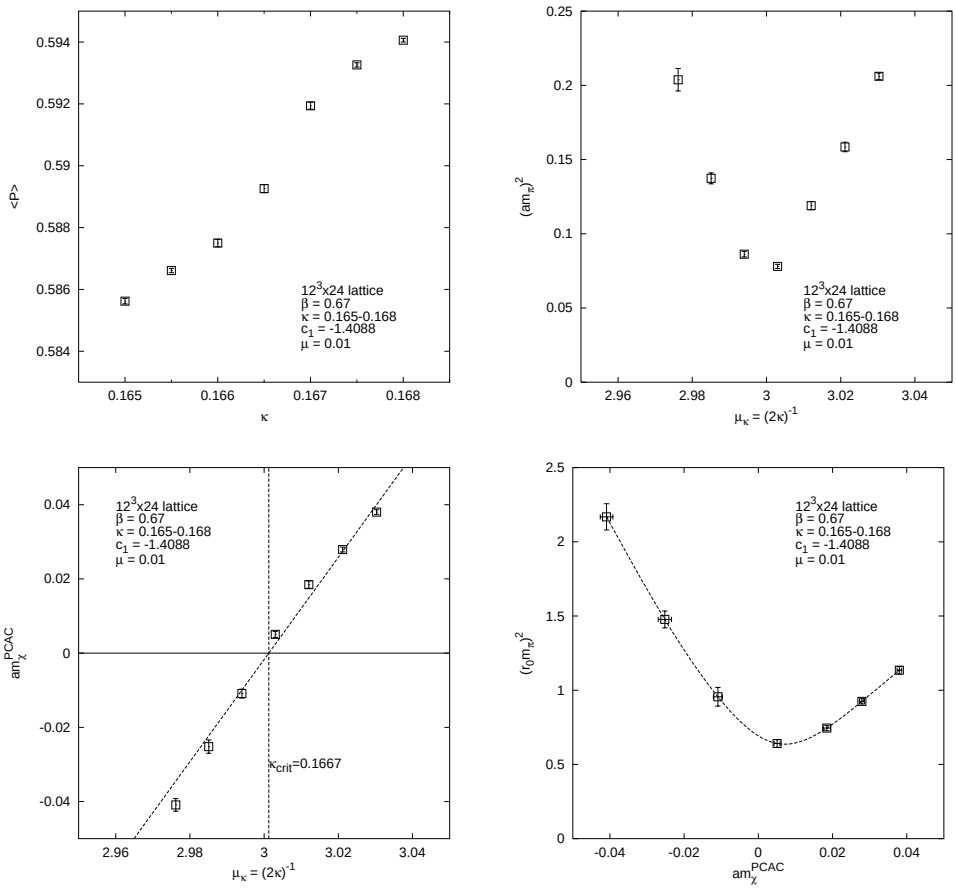

Figure 5.18: *Results produced with the HMC-algorithm code on* $12^3 \times 24$*-lattices,* $\beta = 0.67$ *(DBW2), and* $\mu = 0.01$*; to compare with Figs. 5.13, 5.15, and 5.17.* Upper left panel: *average plaquette expectation value vs.* κ*.* Upper right panel: *pion mass squared vs.* μ_κ*.* Lower left panel: *PCAC quark mass vs.* μ_κ*. Also a linear fit determining* $\kappa_{crit} = 0.1667$ *is shown; taking either just points with negative or positive quark mass resulted in 0.1666, or 0.1668, respectively (not shown).* Lower right panel: *pion mass squared in physical units as a function of the PCAC quark mass, points connected by a spline interpolation.*

sees from the different fits, while the positive quark mass points are well described, the ones with negative quark mass show larger deviations, especially for ω_V and ω_A. The fits resulted in

$$\mu_{\kappa\mathrm{crit}} = 2.99792(27), \qquad Z_\omega = 0.918(16),$$
$$Z_{\omega_V} = 1.378(85), \qquad Z_{\omega_A} = 0.597(19).$$

The different Z_{ω_X}-factors are related to the renormalization factors Z_m, Z_μ, Z_A, and Z_V:

$$Z_\omega = Z_\mu / Z_m, \tag{5.84}$$
$$Z_{\omega_V} = Z_\omega \frac{Z_A}{Z_V}, \tag{5.85}$$
$$Z_{\omega_A} = Z_\omega \frac{Z_V}{Z_A}, \tag{5.86}$$

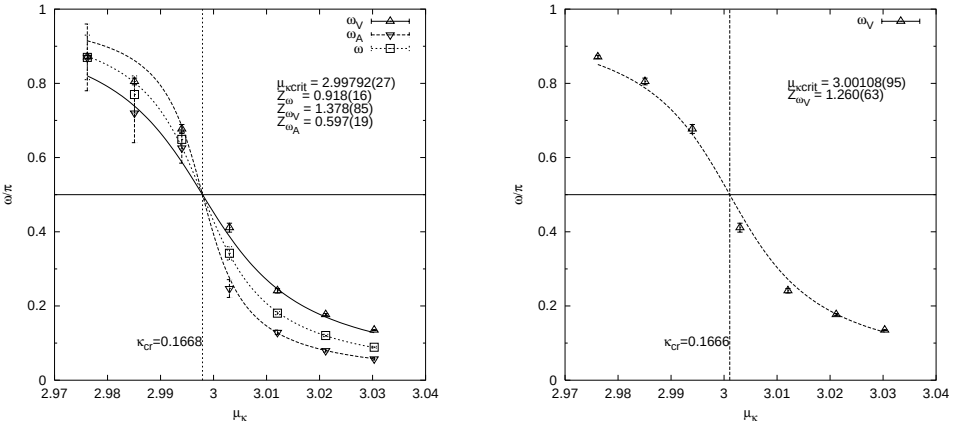

Figure 5.19: Left panel: *Dependence of ω, ω_V, and ω_A on the bare untwisted quark mass parameter. Shown are fits to the function Eq. (5.83) (ω: short dashed line, ω_V: solid line, ω_A: dashed line); first ω was used for a single two-parameter fit to determine Z_ω and $\mu_{\kappa crit}$, the latter was used in the subsequent one-parameter fits of ω_V, ω_A.* Right panel: *Single two-parameter fit of ω_V.*

as follows directly from their definition. This allows for instead using Z_ω directly from the fit, one can use $Z_\omega = \sqrt{Z_{\omega_V} Z_{\omega_A}}$ giving 0.907(31), which agrees within error with the direct result. Also Z_A/Z_V can be extracted either using Z_{ω_V} and Z_{ω_A}:

$$\frac{Z_A}{Z_V} \;=\; \sqrt{\frac{Z_{\omega_V}}{Z_{\omega_A}}} \;=\; 1.519(53),$$

or with the help of Z_ω:

$$\begin{aligned} \frac{Z_A}{Z_V} \;&=\; \frac{Z_{\omega_V}}{Z_\omega} \;=\; 1.50(10), \\ \frac{Z_A}{Z_V} \;&=\; \frac{Z_\omega}{Z_{\omega_A}} \;=\; 1.54(06). \end{aligned}$$

These results agree among each other. The values obtained for this ratio at the single points (Tab. 5.12) depend strongly on κ, especially on the sign of the quark mass. Since the values obtained from the fits are close to the direct measured ones for positive quark mass, this reflects the fact, that the negative quark mass points are not too well determined. This is not a big drawback, it just indicates that physical quantities are best extracted in the region with positive quark mass. Also the minimal quark or pion masses were always obtained in this region and there the simulations are less expensive compared to the negative quark mass region.

Extracting the pion decay constant is possible from either the V_4^+ or the A_4^+ matrix elements in the twisted basis. In Sec. 2.4.3 we argued, that the first should give the better signal near maximal twist. V_4^+ is advantageous, too, because the conserved (point-split) vector current can be used, giving $Z_V = 1$.

If the parameters μ_κ, μ for the untwisted and twisted mass are tuned in such a way, that one stays at the same physical situation (moving around the circle in Fig. 2.1), e.g.,

constant M_{r_0} while ω is varied, the measured matrix elements of the vector or axial-vector currents can be used to extract the physical decay constant. The latter is defined at full twist, if the vector current is used, or at no twist ($\omega = 0, \pi$) in case of the axial-vector current. We give the functional dependence on ω_V, since this angle can be extracted with less uncertainty than the other two.

$$-i\,\frac{\langle 0|V_4^{+\mathrm{cons}}|\pi\rangle}{m_\pi} \;=\; \frac{af_\pi}{\sqrt{1+(\frac{Z_A}{Z_V}\cot\omega_V)^2}} \;+\; \mathcal{O}(a), \tag{5.87}$$

$$\frac{\langle 0|A_4^{+}|\pi\rangle}{m_\pi} \;=\; \pm\,\frac{af_\pi}{Z_A}\,\frac{1}{\sqrt{1+(\frac{Z_V}{Z_A}\tan\omega_V)^2}} \;+\; \mathcal{O}(a). \tag{5.88}$$

(The sign in the last equation depends on whether $\omega < \frac{\pi}{2}$ or not.) Comparing the result extrapolated from the conserved vector current to full twist with the obtained value from an untwisted simulation in the same physical situation allows to determine Z_A, too.

Our simulations were done at fixed μ, therefore different angles imply different quark masses and consequently different values for f_π at maximal twist. Taking this into account, we have the following relation:

$$-i\,\frac{\langle 0|V_4^{+\mathrm{cons}}|\pi\rangle}{m_\pi} \;=\; \sin\omega\,[af_\pi](m_q(\omega)) \;+\; \mathcal{O}(a). \tag{5.89}$$

From χPT we expect a quark mass dependence (here equivalent ω-dependence) of af_π, neglecting terms of order a:

$$\frac{[af_\pi](m_q(\omega))}{[af_\pi](m_q(\pi/2))} \;=\; 1 \;+\; 4(\sigma-1)\chi_R L_{R45} \;-\; \frac{\chi_R}{16\pi^2}\,\sigma\log\sigma, \tag{5.90}$$

where χ_R is defined at the reference quark mass at full twist $m_q(\pi/2)$, with

$$\sigma \;=\; \sigma(\omega) \;=\; \frac{m_q(\omega)}{m_q(\pi/2)}. \tag{5.91}$$

A simple ansatz is to take $\sigma = 1/\sin\omega$, since μ is fixed. As Fig. 5.20, left panel shows for the positive quark mass points, this assumption is justified. There M_{r_0} is used to estimate the quark mass, an extrapolation to full twist gives $M_{r_0}^{\omega=\pi/2} \approx 0.58$. The pion decay constant estimate extracted from the conserved vector current in the twisted basis, $af_{\chi\pi}$, should be fitted to the functional form:

$$[af_{\chi\pi}](\omega) \;=\; [af_\pi](\pi/2)\,\sin\omega\left(1 \;+\; 4\Big(\frac{1}{\sin\omega}-1\Big)\chi_R L_{R45} \;+\; \frac{\chi_R}{16\pi^2}\,\frac{\log(\sin\omega)}{\sin\omega}\right). \tag{5.92}$$

Trying a three-parameter (χ_R, L_{R45}, $[af_\pi](\pi/2)$) fit over the whole range resulted in an unstable result for χ_R. Either one could restrict the three-parameter fit to the positive ($\omega < \pi/2$) quark mass points resulting in $\chi_R = 13(3)$ or fix χ_R to its tree-level estimate using the extrapolated M_{r_0} to full twist (see above): $\chi_R^{\mathrm{est}} = M_{r_0}^{\omega=\pi/2}/(r_0 f_0)^2 \approx 11$. Finally, we performed a two-parameter fit (L_{R45}, $[af_\pi](\pi/2)$) using all points with $\chi_R = 13$ fixed, shown in Fig. 5.20, right panel. Anyhow, due to the large errors of the $\omega > \pi/2$ points this fit is mainly constrained by the positive quark mass points. The fit resulted in

$$\begin{aligned} [af_\pi](\pi/2) &= 0.1108(39), \\ L_{R45} &= 6.70(55)\cdot 10^{-3}. \end{aligned}$$

The latter corresponds to $\Lambda_4/f_0 = 30(5)$, which is reasonable compared to our previous findings, cf. Tab. 5.8. Considering $r_0 f_\pi(\pi/2) \approx 0.317$ (using r_0/a measured at $\kappa = 0.1665$) gives $f_\pi(\pi/2) \approx 125$ MeV at a quark mass $\approx 0.19 m_s$ (from the extrapolated $M_{r_0}^{\omega=\pi/2}$). The figure also shows the curve using the fitted value of $[af_\pi](\pi/2)$ with $\sigma \equiv 1$ in Eq. (5.90), i.e., without the quark mass dependence obtained from χPT. Such a curve should have been resulted from different simulations with $M_{r_0} = \text{const}$.

We demonstrated in which way particular ratios of renormalization factors can be obtained from a set of simulations at fixed (bare) twisted mass parameter μ. Especially Z_ω is a useful combination, because it allows to estimate the quark mass obtained via

$$\begin{aligned} m_q &= \sqrt{m_R^2 + \mu_R^2} \\ &= Z_m \sqrt{\tilde{m}^2 + Z_\omega \mu^2} \end{aligned}$$

up to an overall multiplicative renormalization constant. The latter will drop out, if quark mass ratios are to be considered. Also we extracted the pion decay constant at full twist using χPT. Here we neglected $\mathcal{O}(a)$ and NNLO-contributions, which for sure will play a rôle, but we proved the possibility of such a procedure, leading to a reasonable value for the universal low energy scale Λ_4. Performing sets of simulations at different fixed values of μ (where μ still has to be large enough to stay away from the phase transition line) can finally be used to extrapolate the pion decay constant at maximal twist to zero quark mass, like was done before in the untwisted case.

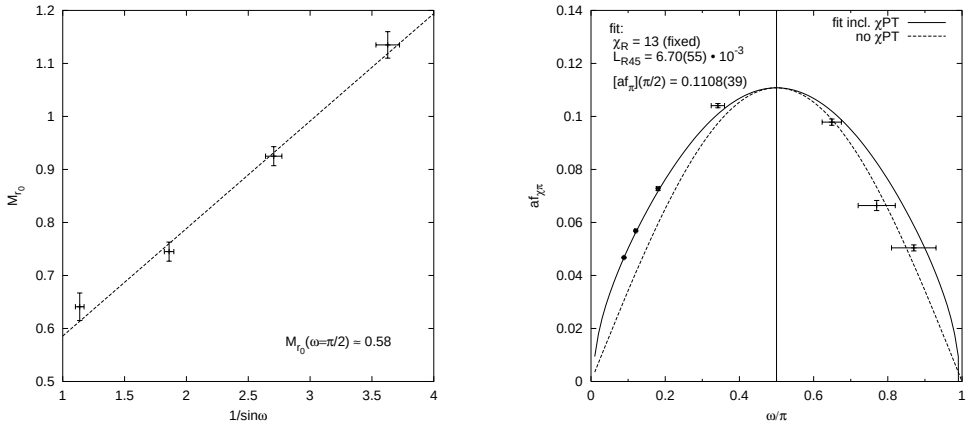

Figure 5.20: Left panel: $M_{r_0} \propto m_q$ *vs.* $1/\sin\omega$, *the dashed line represents a linear fit.* Right panel: *Extrapolating the pion decay constant to its value at maximal twist. Besides the fit (solid line) to Eq. (5.92), also the contribution neglecting the* χPT *part is shown separately (dashed line,* $\sigma \equiv 1$*).*

Conclusions

In this thesis various aspects related to Quantum Chromodynamics with light quark flavors on a lattice have been discussed. In our numerical simulations we aimed for reaching quark masses with dynamical Wilson fermions that are light enough to allow for the application of Chiral Perturbation Theory.

χPT can be used to deal with the low energy behavior of QCD. We outlined the basics of this effective theory and presented its extension if lattice regularized QCD is considered. The inclusion of lattice artifacts into χPT allows to discuss the phase structure of lattice QCD and also to disentangle the physical from the artificial behavior in a χPT analysis of lattice data. We presented the formulae needed to apply χPT to lattice results using partial quenching. It turned out to be advantageous to consider "ratios as functions of ratios" for the quantities in question, i.e., the dependence of the pion masses squared and decay constants on the quark mass. We presented the expressions for these ratios, which were derived from PQχPT-based formulae also including $\mathcal{O}(a)$-effects and modeling NNLO-corrections. Three sets of (untwisted) $N_f = 2$ simulations were performed with Wilson plaquette gauge action, which reached a minimal pion mass of ≈ 370 MeV or a minimal quark mass of $\approx \frac{1}{4}m_s$. Another set even reached $\approx \frac{1}{8}m_s$ by applying the DBW2 gauge action. For the generation of these sets the TSMB-algorithm was used, which has already been proven to be flexible enough, to reach such light quark masses at moderate numerical costs. We were able to demonstrate the applicability of the ansatz to take care of the lattice artifacts in the χPT analysis rather than using a numerically more expensive improved fermion action. The additional information gained by the use of partial quenching allowed to extract particular linear combinations of the low energy constants and universal low energy scales in a reliable way. Surprisingly, the NNLO-corrections turned out to be more important than the lattice artifacts already at the relatively coarse lattice spacings of $a \approx 0.19$ fm. But we also encountered the limitations of this ansatz: at some of our lightest quark masses we were already plagued by the occurrence of exceptional configurations.

For the first time the Wilson twisted mass fermion action has been used in dynamical fermion simulations. We argued, why this formulation is advantageous compared to the usual Wilson fermion formulation. In general, it allows to improve the continuum behavior of relevant quantities, like masses and certain matrix-elements. It renders the fermion determinant strictly positive and therefore avoids exceptional configurations and is thought to weaken the slowing down of algorithms towards small quark masses, too. We listed the methods for the extraction of relevant physical parameters like the pion, rho, and quark masses and the pion decay constant from twisted simulations. The measurement of the twist angle was discussed in detail. The latter is not a physical parameter but is crucial to tune the simulations near to the point, where automatic full $\mathcal{O}(a)$-improvement is

achieved. We developed the extension of PQχPT to include the twisted mass term. With these formulae at hand the program we performed to extract the LECs from untwisted simulations becomes applicable to QCD$^{\mathrm{TM}}$, as well.

The phase structure of lattice QCD near zero quark mass with two flavors of Wilson fermions has been considered both analytically and numerically. The two possible phase structure scenarios—the Aoki phase and normal phase scenario—were discussed. We performed numerical simulations with QCD$^{\mathrm{TM}}$ using the Wilson plaquette gauge action as well as the renormalization group improved DBW2 gauge action. With the unimproved Wilson plaquette gauge action strong metastabilities near the phase transition line occurred. We were able to demonstrate that the usage of an improved gauge action weakens the phase transition and metastabilities. With the DBW2 gauge action a lightest pion mass of ≈ 250 MeV at a lattice spacing of $a \approx 0.20$ fm at a $L^3 \times T = 12^3 \times 24$ lattice has been reached. Because of the mentioned caveats of the DBW2 gauge action further investigations should examine, if the same benefits could also be obtained with the tree-level Symanzik improved gauge action, avoiding the caveats of DBW2.

In a set of simulations at fixed twisted mass parameter we determined a set of physical quantities. Also the twist angle has been determined and we demonstrated a possibility how to extrapolate the pion decay constant to its value at maximal twist. Performing such sets of simulations at different values for the twisted mass parameter and analyzing them in the way presented here, can be used to obtain the data needed for a χPT analysis, studying the quark mass dependence of, e.g., the pion decay constant.

In the numerical twisted mass studies two different algorithms have been used to include the dynamical fermions: the TSMB- and the HMC-algorithm. We focused on implementing QCD$^{\mathrm{TM}}$ into the TSMB-algorithm routines and tuning the update-parameters to be able to perform the simulations at relatively low numerical costs. We argued that the inclusion of split-doublets (twisted mass with mass-non-degenerate fermions) is straightforward in the case of the TSMB-algorithm; we present the necessary modifications on the implementation in the appendix of this thesis. With the experience we gained from the numerical simulations, we are now in the position to start simulations with $N_f = 2+(1+1)$ fermion flavors. By that we mean adding to the un-split twisted doublet of the light quarks, representing the up- and down-quarks as mass-degenerate, a strange-quark and a heavier charm-quark. Simulations at the value of the physical strange-quark mass are clearly possible. The charm-quark could even be effectively removed by choosing the mass-splitting in such a way, that it receives a mass of the order of the cut-off. By such simulations the full SU(3)-flavor content of χPT can be studied by numerical simulations. In a further step, also the mass splitting between the light up- and down-quarks can be incorporated by performing $N_f = (1 + 1) + (1 + 1)$ simulations. In all the proposed simulations the gauge action should be chosen to be an improved one to be able to reach quark masses as close as possible to the physical ones.

Appendix A

Notations and conventions

A.1 Useful notations

We applied natural units $\hbar = c = 1$, resulting in the useful conversion

$$1 \text{ GeV}^{-1} \;=\; 0.197327 \text{ fm}. \tag{A.1}$$

Furthermore, in χPT-formulae we chose a normalization such that the pion decay constant is set to $f_0 = 93$ MeV.

By ∂^*_μ we denote the lattice backward derivative:

$$\partial^*_\mu F(x) \;\equiv\; F(x) \;-\; F(x - \hat{\mu}). \tag{A.2}$$

For a compact notation we also define the Dirac matrices (see App. A.4) and gauge-links with negative index:

$$\gamma_{-\mu} \;\equiv\; -\gamma_\mu, \quad U_{-\mu}(x) \;\equiv\; U^\dagger_\mu(x - \hat{\mu}), \quad \mu = 1, 2, 3, 4. \tag{A.3}$$

A.2 Euclidean space-time

We prefer to work in Euclidean rather than Minkowski space-time throughout this work. The two are related by a *Wick-rotation* of $\frac{\pi}{2}$, which results in a purely imaginary time-component

$$x_0 \;=\; -ix_4, \quad x_4 \in \mathbb{R}. \tag{A.4}$$

Using now the Euclidean, real components $x_{1,2,3,4}$ the metric is defined

$$g_{\mu\nu} \;=\; \delta_{\mu\nu}. \tag{A.5}$$

The symbol t is used for x_4, too: $t \equiv x_4$; the space components are collected in a three-vector $\boldsymbol{x} \equiv (x_1, x_2, x_3)$. For more details we refer to, e.g., [17].

A.3 Generators of SU(N)

Every element of the *Lie-group* SU(N) can be represented as

$$\Lambda \;=\; \exp\left[\sum_{a=1}^{N^2-1} iT_a\omega_a\right], \quad \omega_a \in \mathbb{R}, \tag{A.6}$$

with the generators T_a of the Lie-algebra, being Hermitian, traceless $N \times N$ matrices, normalized according to

$$\mathrm{Tr}(T_aT_b) \;=\; \delta_{ab}, \tag{A.7}$$

and satisfying the commutation relations

$$[T_a, T_b] \;=\; if_{abc}T_c, \tag{A.8}$$

with the structure constants f_{abc} being totally antisymmetric and real.

A.3.1 SU(2), Pauli matrices

In case of $N = 2$ the generators are chosen to be

$$T_a \;=\; \frac{1}{2}\tau_a, \quad a = 1, 2, 3 \tag{A.9}$$

with the Pauli matrices

$$\tau_1 \;=\; \begin{pmatrix} 0 & 1 \\ 1 & 0 \end{pmatrix}, \;\; \tau_2 \;=\; \begin{pmatrix} 0 & -i \\ i & 0 \end{pmatrix}, \;\; \tau_3 \;=\; \begin{pmatrix} 1 & 0 \\ 0 & -1 \end{pmatrix}, \tag{A.10}$$

which satisfy

$$\tau_j\tau_k \;=\; \delta_{jk} \;+\; i\epsilon_{jkl}\tau_l, \tag{A.11}$$

$$\tau_1\tau_2\tau_3 \;=\; i. \tag{A.12}$$

We also define

$$\tau_\pm \;=\; \frac{\tau_1 \pm i\tau_2}{2}. \tag{A.13}$$

A.3.2 SU(3), Gell-Mann matrices

In general the $(N^2 - 1)$ generators T_a of SU(N) can be given by the Gell-Mann matrices λ_a:

$$T_a \;=\; \frac{\lambda_a}{2}. \tag{A.14}$$

The completeness relation of the Gell-Mann matrices reads

$$\sum_{j=1}^{N^2-1} (\lambda_j)_{ab}(\lambda_j)_{cd} \;=\; 2\left(\delta_{ad}\delta_{bc} \;-\; \frac{1}{N}\delta_{ab}\delta_{cd}\right), \tag{A.15}$$

while their anticommutators are

$$\{\lambda_j, \lambda_k\} \;=\; \frac{4}{N}\delta_{jk} \;+\; 2d_{jkl}\lambda_l \tag{A.16}$$

with d_{jkl} totally symmetric. For $N = 3$ the Gell-Mann matrices are

$$\lambda_1 = \begin{pmatrix} 0 & 1 & 0 \\ 1 & 0 & 0 \\ 0 & 0 & 0 \end{pmatrix}, \quad \lambda_2 = \begin{pmatrix} 0 & -i & 0 \\ i & 0 & 0 \\ 0 & 0 & 0 \end{pmatrix}, \quad \lambda_3 = \begin{pmatrix} 1 & 0 & 0 \\ 0 & -1 & 0 \\ 0 & 0 & 0 \end{pmatrix},$$
$$\lambda_4 = \begin{pmatrix} 0 & 0 & 1 \\ 0 & 0 & 0 \\ 1 & 0 & 0 \end{pmatrix}, \quad \lambda_5 = \begin{pmatrix} 0 & 0 & -i \\ 0 & 0 & 0 \\ i & 0 & 0 \end{pmatrix}, \quad \lambda_6 = \begin{pmatrix} 0 & 0 & 0 \\ 0 & 0 & 1 \\ 0 & 1 & 0 \end{pmatrix},$$
$$\lambda_7 = \begin{pmatrix} 0 & 0 & 0 \\ 0 & 0 & -i \\ 0 & i & 0 \end{pmatrix}, \quad \lambda_8 = \frac{1}{\sqrt{3}} \begin{pmatrix} 1 & 0 & 0 \\ 0 & 1 & 0 \\ 0 & 0 & -2 \end{pmatrix}. \tag{A.17}$$

A.4 Dirac matrices

We choose the Euclidean Dirac matrices $\gamma_\mu, \mu = 1, 2, 3, 4$ to be Hermitian. They fulfill

$$\{\gamma_\mu, \gamma_\nu\} = 2\delta_{\mu\nu}. \tag{A.18}$$

Furthermore,

$$\gamma_5 = \gamma_1\gamma_2\gamma_3\gamma_4 = \gamma_5^\dagger \tag{A.19}$$

is defined, which anticommutates with all $\gamma_\mu, \mu = 1, 2, 3, 4$:

$$\{\gamma_5, \gamma_\mu\} = 0. \tag{A.20}$$

In the *chiral representation*, which will be used throughout this work, γ_5 is chosen to be diagonal:

$$\gamma_{1,2,3} = \begin{pmatrix} 0 & -i\tau_{1,2,3} \\ i\tau_{1,2,3} & 0 \end{pmatrix}, \ \gamma_4 = \begin{pmatrix} 0 & \mathbb{1} \\ \mathbb{1} & 0 \end{pmatrix}, \ \gamma_5 = \begin{pmatrix} \mathbb{1} & 0 \\ 0 & -\mathbb{1} \end{pmatrix}. \tag{A.21}$$

The relation to the Dirac matrices in Minkowski space is:

$$\gamma_{1,2,3} = -i\gamma_{1,2,3}^{\text{Minkowski}}, \tag{A.22}$$
$$\gamma_4 = -i\gamma_4^{\text{Minkowski}} = \gamma_0^{\text{Minkowski}}. \tag{A.23}$$

Appendix B

Improved gauge actions

In this appendix we sketch very briefly improved gauge actions, since they were used in our simulations. For a more detailed discussion, we refer to the literature, e.g., [13] contains a recent overview. The idea of improved gauge actions is to reach the continuum limit faster, i.e., by reducing lattice artifacts induced by the gauge part of the action to the level $\mathcal{O}(a^2)$. We already mentioned Symanzik's improvement program, which also can be applied to the gauge part. One has to add counterterms, which correct for the unwanted contributions due to the finite lattice discretization. In case of the gauge action, in general one has to incorporate larger Wilson-loops than just the simple 1×1 plaquette. This leads, e.g., to the *Symanzik tree-level improved* gauge action [128, 129] or the *Lüscher-Weisz* gauge action [130, 131].

A different ansatz uses renormalization-group (RG) equations, as formulated by Wilson [132]. The idea is to stay near a trajectory in the space of lattice actions, which ends in a fixed point and therefore shows an improved scaling behavior. Usually one considers a 2-parameter action space; commonly used RG-improved gauge actions are the DBW2 (doubly blocked Wilson) [133, 134] and the Iwasaki [135] gauge action.

In our numerical simulations we considered improved gauge actions of the form

$$S_g[U] \;=\; \beta \sum_x \left[c_0 \sum_{\substack{\mu,\nu=1 \\ \mu<\nu}}^{4} \left(1 - \frac{1}{3}\mathrm{ReTr} U_{\mu\nu}^{1\times 1}(x)\right) + c_1 \sum_{\substack{\mu,\nu=1 \\ \mu\neq\nu}}^{4} \left(1 - \frac{1}{3}\mathrm{ReTr} U_{\mu\nu}^{1\times 2}(x)\right) \right], \quad \text{(B.1)}$$

with the normalization condition $c_0 = 1 - 8c_1$. Here not only the simple plaquette (now denoted as $U_{\mu\nu}^{1\times 1}(x)$, Eq. (1.6)) enters, but also planar rectangular contributions:

$$U_{\mu\nu}^{1\times 2}(x) \;\equiv\; U_\mu(x) U_\nu(x+\hat{\mu}) U_\nu(x+\hat{\mu}+\hat{\nu}) U_\mu^\dagger(x+2\hat{\nu}) U_\nu^\dagger(x+\hat{\nu}) U_\nu^\dagger(x). \quad \text{(B.2)}$$

For $c_1 = 0$ one obtains Wilson plaquette gauge action, Eq. (1.7), other values refer to:

$$c_1 \;=\; \begin{cases} -0.331 & \text{Iwasaki action} \\ -1.4088 & \text{DBW2 action} \\ -\frac{1}{12} & \text{tree-level improved (Symanzik)} \end{cases} . \quad \text{(B.3)}$$

In case of the Lüscher-Weisz gauge action non-planar contributions have to be taken into account, too.

Appendix C

Update and measurement routines

For the generation of samples of gauge configurations with a TSMB-based algorithm and the measurement of the correlators and the Wilson-loops, different routines were used. These routines differ with respect to the fermion action (untwisted, twisted, or twisted with non-degenerate doublet) and gauge action (just Wilson plaquette or with additional rectangular planar contribution) to be simulated. Furthermore, since computer time was available to us on different computer architectures, the code had to be optimized or even rewritten for that special purposes. Large lattice sizes and the generation of samples with sufficient statistics to keep the statistical error well under control required the use of parallel computing, i.e., distributing the execution of the code on a number of processors. This parallelization has to be implemented into the routines, too. Also the memory requirements on large lattices with light quark masses (cf. the discussion in Sec. 5.1.2 on this point) rule out the possibility to use single processor architectures for the generation of the gauge configurations. The latter point becomes even worse, since with growing lattice sizes, one should use 64-bit precision ("double precision") rather than 32-bit ("single precision") to keep the rounding error, e.g., in so-called global sums under control. For lattice sizes up to 16^4 or $12^3 \times 24$ single precision still is sufficient, while for $16^3 \times 32$ the situation is not clearly decided and may depend on the size of the simulated quark mass. For even larger lattices double precision is required. We mainly used for our simulations the following resources:

- a PC-cluster, consisting of 32 dual processor nodes connected via Myrinet for fast inter-node communication installed at DESY Hamburg,
- the APEmille, installed at DESY Zeuthen,
- the Cray T3E, was installed at FZ Jülich,
- the IBM p690 "JUMP", installed at FZ Jülich (successor of the Cray T3E),
- several PCs at DESY Hamburg and Zeuthen (mainly for measurement-routines and small test-runs)

Routines for untwisted fermions with Wilson plaquette gauge action were already existing: `nf3qcd` and `mbqcd`. They have been developed by C. Gebert and contain the update as well as the measurement routines [98].

`nf3qcd` is written in C++ and can be compiled to run in 32- or 64-bit precision. Parallelization is implemented by dividing the lattice into several sub-lattices, each of them distributed to one processor. The needed communication between the local lattices is done by using the `MPI`-package. The code was already optimized for normal PCs and PC-clusters, like the one installed at DESY Hamburg and also for the Cray T3E, which was operated at the Forschungszentrum Jülich. The latter has been replaced by an IBM p690 (JUMP), which required further optimization of the code. We provided the latter. Also a feature was added to the code, which allows to store the boson fields on the hard disk during the execution just keeping a fraction of the total fields in the memory. This allows to circumvent memory restrictions on large lattices with high first orders (n_1) in the polynomial approximation as needed if light quark masses are to be simulated.

`mbqcd` is written in TAOmille and can be used on the APEmille as installed at DESY Zeuthen. This code is equivalent to `nf3qcd`, but only supports 32-bit precision. The latter is due to APEmille-specific internal data-type processing. The communication-calls are included in the TAOmille language.

We took the both existing codes as a starting point for developing the update- and measurement routines for the twisted mass fermion actions and the improved gauge actions. Modifications will be presented in the remainder of this appendix. Since the HMC-algorithm based code was developed and maintained by our collaborators at DESY Zeuthen, we refer for details on its implementation to [33, 120, 121]. Configurations produced by the latter are stored in a different format; to convert configurations from HMC- to TSMB-format and vice versa, we provided a small routine.[1]

C.1 Twisted mass code

We developed the update code for twisted mass simulations using the QCD$^{\mathrm{TM}}$ action with mass-degenerate doublets (`tmqcd`) and mass-non-degenerate doublets (`tmsplit`), written in C++ and optimized for the architectures listed above. A TAOmille version only exist for the mass-degenerate case. The main changes concerned the internal matrix-vector-multiplication routines and the calculation of the action based on the root-representation for the bosonic fields in case the even-odd preconditioning is used. For the measurement routine the inverter-routines calculating Q^{-1} had to be modified and correlators had to be added.

C.1.1 Updating routines

As already argued in Sec. 5.1.2, it is advantageous to implement the QCD$^{\mathrm{TM}}$ action by introducing separate boson fields for each flavor of the doublet. This allows for even-odd preconditioning of the fermion-matrix and a straightforward generalization for the mass-non-degenerate case. The preconditioning for $\mu_\Delta = 0$ has already been presented (Sec. 5.1.2), here we give the corresponding procedure for $\mu_\Delta \neq 0$. The fermion matrix

[1] The routine is called `fileconvert` and is a further development of a routine, needed for converting between configurations produced with the TAOmille and the C++ code.

can be decomposed as

$$\begin{aligned}
\tilde{Q}_\chi &= \begin{pmatrix} \gamma_5\tau_1(\mu_\kappa + i\mu\gamma_5\tau_3 + \mu_\Delta\tau_1) & -\frac{1}{2}\gamma_5\tau_1 D_{eo} \\ -\frac{1}{2}\gamma_5\tau_1 D_{oe} & \gamma_5\tau_1(\mu_\kappa + i\mu\gamma_5\tau_3 + \mu_\Delta\tau_1) \end{pmatrix} \\
&= \begin{pmatrix} \gamma_5\tau_1(\mu_\kappa + i\mu\gamma_5\tau_3 + \mu_\Delta\tau_1) & 0 \\ 0 & \gamma_5\tau_1(\mu_\kappa + i\mu\gamma_5\tau_3 + \mu_\Delta\tau_1) \end{pmatrix} \begin{pmatrix} 1 & 0 \\ -\frac{1}{2}t_5 D_{oe} & 1 \end{pmatrix} \times \\
&\quad \times \begin{pmatrix} 1 & 0 \\ 0 & 1 - \frac{1}{4}t_5 D_{oe} t_5 D_{eo} \end{pmatrix} \begin{pmatrix} 1 & -\frac{1}{2}t_5 D_{eo} \\ 0 & 1 \end{pmatrix}, \qquad \text{(C.1)} \\
t_5 &\equiv \Big[\gamma_5\tau_1(\mu_\kappa + i\mu\gamma_5\tau_3 + \mu_\Delta\tau_1)\Big]^{-1} \gamma_5\tau_1 \\
&= \frac{\mu_\Delta\gamma_5 - \mu_\kappa\gamma_5\tau_1 - \mu\tau_2}{\mu_\Delta^2 - \mu_\kappa^2 - \mu^2}\gamma_5\tau_1, \qquad \text{(C.2)}
\end{aligned}$$

leading to the preconditioned matrix

$$\bar{Q}_\chi = \gamma_5\tau_1\Big(\mu_\kappa + i\mu\gamma_5\tau_3 + \tau_1\mu_\Delta - \frac{1}{4}D_{oe}t_5 D_{eo}\Big). \qquad \text{(C.3)}$$

The coefficients in Eq. (5.46) now read (also valid for $\mu_\Delta = 0$):

$$\begin{aligned}
A_{ee}^{(i)} &= \mu_\kappa^2 + \mu^2 + \mu_\Delta^2 + 2\mu_\kappa\mu_\Delta\tau_1 + 2\mu\mu_\Delta\gamma_5\tau_2 + 4 \qquad \text{(C.4)} \\
A_{oo}^{(i)} &= A_{ee}^{(i)} + |\rho_i|^2 - (\rho_i + \rho_i^*)\gamma_5\tau_1(\mu_\kappa + i\mu\gamma_5\tau_3 + \mu_\Delta\tau_1) \qquad \text{(C.5)} \\
b_x^{(i)} &= \frac{1}{4}\sum_{\mu,\nu=\pm1}^{\pm4}(1 + \gamma_\mu - \gamma_\nu - \gamma_\mu\gamma_\nu)U_\mu^\dagger(x)U_\nu^\dagger(x+\hat{\mu})\phi_{x+\hat{\mu}+\hat{\nu}}^{(i)} \\
&\quad - \sum_{\mu=\pm1}^{\pm4}\Big[\mu_\kappa + \mu_\Delta\tau_1 + \frac{R}{2}\gamma_5\tau_1(1-\gamma_\mu)\Big]U_\mu^\dagger(x)\phi_{x+\hat{\mu}}^{(i)}, \qquad \text{(C.6)} \\
R &= \begin{cases} \rho & \text{, even sites} \\ \rho^* & \text{, odd sites} \end{cases}, \qquad \text{(C.7)}
\end{aligned}$$

and depend in general on the site-parity: A_{ee} for even-even and A_{oo} for odd-odd sites.

Also the definition of the auxiliary boson fields has to be slightly modified. These fields allow for a quick computation of the change in the fermionic action, if only local gauge field updates are performed (cf. Sec. 1.4.1 in [98] for more details). Writing the fermionic action with explicit dependence on the particular link variable $U_\mu(x)$ as

$$\Delta S_\phi(U_\mu(x), \phi) = \mathrm{ReTr}\Big(U_\mu(x)\Delta S_{x,\mu}^{(1)}(\phi) + U_\mu(x)\Delta S_{x,\mu}^{(2)}(\phi, [U]\backslash\{U_\mu(x)\})\Big), \qquad \text{(C.8)}$$

the change of the action if only this link is updated can be easily computed, if a further decomposition of $\Delta S^{(2)}$ is applied:

$$\Delta S_{x,\mu}^{(2)} = \sum_{\substack{\nu=1 \\ \mu\neq\nu}}^{4}\Big(f_{x,\mu\nu}^{++}U_\nu(x+\hat{\mu}) + f_{x,\mu\nu}^{+-}U_\nu^\dagger(x+\hat{\mu}-\hat{\nu}) + U_\nu^\dagger(x)f_{x+\hat{\nu},\nu\mu}^{-+} + U_\nu(x-\hat{\nu})f_{x-\hat{\nu},\nu\mu}^{++}\Big). \qquad \text{(C.9)}$$

Here the terms $f^{xx} = f^{xx}(\phi)$ only depend on the boson fields and not on the gauge fields. In the twisted case $\Delta S^{(2)}$ remains unchanged compared to the untwisted one, while now

$$\Delta S_{x,\mu}^{(1)}(\phi) = 2\sum_i \phi_x^{(i)\dagger}\Big[\mu_\kappa + \mu_\Delta\tau_1 + \gamma_5\tau_1\frac{R}{2}(1-\gamma_\mu)\Big]\phi_{x+\hat{\mu}}^{(i)}, \qquad \text{(C.10)}$$

with R being defined in Eq. (C.7).

C.1.2 Measuring correlators

The measurement routines for the correlators are implemented for the mass-degenerate case. In practice the twisted basis is used, written in terms of $\tau_\pm, \tau_3$. Defining operators

$$X_x^\pm \;=\; \bar{\chi}'(x)\Gamma_X\tau_\pm\chi(x) \;=\; \begin{cases} \bar{u}'(x)\Gamma_X d(x), & + \\ \bar{d}'(x)\Gamma_X u(x), & - \end{cases}, \tag{C.11}$$

we compute correlators[2](compare with Sec. 1.2.2)

$$\begin{aligned} C_{XY}(x_4 - y_4) \;&=\; \frac{1}{V_s}\sum_{\boldsymbol{x},\boldsymbol{y}} \Big\langle {X_x^-}^\dagger(x) Y_y^-(y)\Big\rangle \\ &=\; \frac{1}{V_s}\sum_{\boldsymbol{x},\boldsymbol{y}} \mathrm{Tr}\Big(\Delta^{d\dagger}_{yx}\gamma_5\Gamma_X^\dagger\Delta^d_{xy}\Gamma_Y\gamma_5\Big). \end{aligned} \tag{C.12}$$

Here Δ^d denotes the propagator $d\bar{d} = {Q_\chi^d}^{-1}$ and we made use of $\gamma_5 {Q_\chi^u}^{-1}\gamma_5 = {Q_\chi^{d\dagger}}^{-1}$ following from Eq. (2.12). So it is sufficient to calculate the inverse of the fermion matrix with just one sign for the twisted mass term, i.e., working in the subspace of just one flavor.

In the measurement routines the part calculating the inverse of the fermion matrix had to be modified, too. Here we applied the even-odd preconditioned version of the fermion matrix to gain a speed-up in the number of iterations used for the inversion. This can be done in the usual way, using the decomposition

$$Q \;=\; A\,L\,\bar{Q}\,R \tag{C.13}$$

(compare with Eq. (5.37) and note that A^{-1}, L^{-1}, and R^{-1} are easily obtained). Instead of solving

$$Q\,x \;=\; s \;\Leftrightarrow\; x \;=\; Q^{-1}\,s$$

one considers

$$\bar{Q}\,x' \;=\; L^{-1}\,A^{-1}\,s \;\Leftrightarrow\; x \;=\; R^{-1}\,x' \;=\; Q^{-1}\,s.$$

Since as has been argued above only the inverse of the fermion matrix corresponding to one flavor is needed, we will modify the even-odd preconditioning accordingly. Writing in the flavor subspaces

$$Q_\chi^{u,d} \;=\; \mu_\kappa \;\pm\; i\mu\gamma_5 \;-\; \frac{1}{2}D$$

[2]Observe that

$$O^- \;=\; \begin{cases} (O^+)^\dagger, & O = P, V \\ -(O^+)^\dagger, & O = A \end{cases}.$$

the even-odd preconditioning is achieved by (note that $(\tilde{Q}^{u,d})^\dagger = \tilde{Q}^{d,u}$)

$$\begin{aligned}
\gamma_5 Q_\chi^{u,d} &= \tilde{Q}^{u,d} = A_\pm \, L_\pm \bar{Q}_\pm R_\pm \\
A_\pm &\equiv \gamma_5 \mu_\kappa \pm i\mu \\
L_\pm &\equiv \begin{pmatrix} 1 & 0 \\ -\frac{A_\pm^{-1}}{2}\gamma_5 D_{oe} & 1 \end{pmatrix} \\
R_\pm &\equiv \begin{pmatrix} 1 & -\frac{A_\pm^{-1}}{2}\gamma_5 D_{eo} \\ 0 & 1 \end{pmatrix} \\
\bar{Q}_\pm &\equiv \begin{pmatrix} 1 & 0 \\ 0 & 1 - \frac{A_\pm^{-1}}{2}\gamma_5 D_{oe} \frac{A_\pm^{-1}}{2}\gamma_5 D_{eo} \end{pmatrix}.
\end{aligned}$$

Here the matrices are written in the subspaces of even and odd lattice sites. Instead solving

$$\gamma_5 Q_\chi^d \, x = \gamma_5 s$$

one considers only the odd lattice site subspace of

$$\bar{Q}_- \, (Rx) = L_-^{-1} A_-^{-1} \gamma_5 s.$$

Here some care has to be taken, since $\bar{Q}_-^\dagger$ is not equal to $\bar{Q}_-$ but

$$\bar{Q}_\pm^\dagger = \begin{pmatrix} 1 & 0 \\ 0 & 1 - \gamma_5 D_{oe} \frac{(A_\pm^{-1})^\dagger}{2}\gamma_5 D_{eo} \frac{(A_\pm^{-1})^\dagger}{2} \end{pmatrix},$$

where $A_\pm^\dagger = A_\mp$ might be used.

We compute the correlators C_{XY} with the following combinations for XY:

$$PP, A_4P, V_4P, A_4A_4, A_4V_4, V_4A_4, V_4V_4, \frac{1}{3}\sum_{i=1}^{3} V_iV_i, \frac{1}{3}\sum_{i=1}^{3} A_iA_i, \frac{1}{3}\sum_{i=1}^{3} V_iA_i, \frac{1}{3}\sum_{i=1}^{3} A_iV_i,$$

whose implementation is trivial. In addition also combinations with the conserved (point-split) vector current (Eq. (2.58))

$$V_4^{\mathrm{cons}}P, V_4^{\mathrm{cons}}A_4, V_4^{\mathrm{cons}}V_4,$$

and the (lattice backward) derivatives of A_4P and V_4P: $(\partial_4^* A_4)P$, $(\partial_4^* V_4)P$ are evaluated. Each correlator is calculated with a Jacobi-smeared source and local or smeared sink (cf. Sec. 1.2).

C.2 Improved gauge actions

We also implemented improved gauge actions (cf. App. B) into our routines. We only considered such actions, which can be described by including additional planar rectangular plaquette contributions like, e.g., the tree-level (Symanzik), DBW2, or Iwasaki gauge action, Eq. (B.1). The routines containing this feature are named like before with the suffix `_DBW2` added.[3] This name hides somehow the fact, that the parameter c_1 specifying

[3] We did not extend the TAOmille code to include improved gauge actions.

the particular gauge action, is not fixed but can be varied to obtain the different improved gauge actions, Eq. (B.3).

The modifications necessary for using these actions for the gauge part were the following: (1) including the rectangular pieces in the calculation for the change of the action ΔS after a gauge field update was done, and (2) extending the communication in the parallel version, since now also the gauge fields with distance two are needed to calculate ΔS.

The measurement codes are, of course, unaffected by this change. But one has to keep in mind, that the change in the gauge action influences the computation of r_0/a as indicated in Eq. (1.22).

C.3 MSMB-algorithm

For some first exploratory studies we implemented the MSMB-algorithm (Sec. 5.1.2) with $m = 2$ into the C++-version yielding `msmbqcd`. The changes just incorporate the additional needed polynomials and a reorganization of the update-sequence.

Bibliography

[1] K. G. Wilson, New Phenomena In Subnuclear Physics. Part A. Proceedings of the First Half of the 1975 International School of Subnuclear Physics, Erice, Sicily, July 11 - August 1, 1975, ed. A. Zichichi, Plenum Press, New York, 1977, p. 69, CLNS-321.

[2] J. Callan, Curtis G., Phys. Rev. **D2**, 1541 (1970).

[3] K. Symanzik, Commun. Math. Phys. **18**, 227 (1970).

[4] R. Sommer, Nucl. Phys. **B411**, 839 (1994), hep-lat/9310022.

[5] ALPHA, M. Guagnelli, R. Sommer, and H. Wittig, Nucl. Phys. **B535**, 389 (1998), hep-lat/9806005.

[6] APE, M. Albanese *et al.*, Phys. Lett. **B192**, 163 (1987).

[7] UKQCD, C. R. Allton *et al.*, Phys. Rev. **D47**, 5128 (1993), hep-lat/9303009.

[8] C. Michael, Nucl. Phys. **B259**, 58 (1985).

[9] S. Perantonis, A. Huntley, and C. Michael, Nucl. Phys. **B326**, 544 (1989).

[10] UKQCD, C. R. Allton *et al.*, Phys. Rev. **D65**, 054502 (2002), hep-lat/0107021.

[11] M. Lüscher and U. Wolff, Nucl. Phys. **B339**, 222 (1990).

[12] R. G. Edwards, U. M. Heller, and T. R. Klassen, Nucl. Phys. **B517**, 377 (1998), hep-lat/9711003.

[13] S. Necco, *The static quark potential and scaling behavior of SU(3) lattice Yang-Mills theory*, PhD thesis, Humboldt University Berlin, 2003, hep-lat/0306005.

[14] S. Necco, Nucl. Phys. **B683**, 137 (2004), hep-lat/0309017.

[15] M. Creutz, Phys. Rev. **D21**, 2308 (1980).

[16] M. Creutz, Phys. Rev. Lett. **45**, 313 (1980).

[17] I. Montvay and G. Münster, *Quantum fields on a lattice* , Cambridge, UK: Univ. Pr. (1994) 491 p. (Cambridge monographs on mathematical physics).

[18] CP-PACS, A. Ali Khan *et al.*, Phys. Rev. **D65**, 054505 (2002), hep-lat/0105015.

[19] F. Farchioni, C. Gebert, I. Montvay, and L. Scorzato, Eur. Phys. J. **C26**, 237 (2002), hep-lat/0206008.

[20] ALPHA, R. Frezzotti, M. Hasenbusch, U. Wolff, J. Heitger, and K. Jansen, Comput. Phys. Commun. **136**, 1 (2001), hep-lat/0009027.

[21] K. Osterwalder and E. Seiler, Ann. Phys. **110**, 440 (1978).

[22] S. Aoki and A. Gocksch, Phys. Lett. **B231**, 449 (1989).

[23] S. Aoki and A. Gocksch, Phys. Rev. **D45**, 3845 (1992).

[24] W. A. Bardeen, A. Duncan, E. Eichten, and H. Thacker, Phys. Rev. **D59**, 014507 (1999), hep-lat/9806002.

[25] E.-M. Ilgenfritz, W. Kerler, M. Müller-Preussker, A. Sternbeck, and H. Stüben, Phys. Rev. **D69**, 074511 (2004), hep-lat/0309057.

[26] R. Frezzotti and G. C. Rossi, JHEP **08**, 007 (2004), hep-lat/0306014.

[27] A. D. Kennedy, Nucl. Phys. Proc. Suppl. **140**, 190 (2005), hep-lat/0409167.

[28] XLF, W. Bietenholz *et al.*, JHEP **12**, 044 (2004), hep-lat/0411001.

[29] R. Frezzotti and G. C. Rossi, JHEP **10**, 070 (2004), hep-lat/0407002.

[30] C. Pena, S. Sint, and A. Vladikas, JHEP **09**, 069 (2004), hep-lat/0405028.

[31] R. Frezzotti and G. C. Rossi, Nucl. Phys. Proc. Suppl. **128**, 193 (2004), hep-lat/0311008.

[32] S. Aoki and O. Bär, Phys. Rev. **D70**, 116011 (2004), hep-lat/0409006.

[33] F. Farchioni *et al.*, Eur. Phys. J. **C42**, 73 (2005), hep-lat/0410031.

[34] S. R. Sharpe and J. M. S. Wu, Phys. Rev. **D71**, 074501 (2005), hep-lat/0411021.

[35] R. Frezzotti, G. Martinelli, M. Papinutto, and G. C. Rossi, (2005), hep-lat/0503034.

[36] XLF, K. Jansen, A. Shindler, C. Urbach, and I. Wetzorke, Phys. Lett. **B586**, 432 (2004), hep-lat/0312013.

[37] A. M. Abdel-Rehim and R. Lewis, Phys. Rev. **D71**, 014503 (2005), hep-lat/0410047.

[38] XLF, K. Jansen, M. Papinutto, A. Shindler, C. Urbach, and I. Wetzorke, Phys. Lett. **B619**, 184 (2005), hep-lat/0503031.

[39] A. M. Abdel-Rehim, R. Lewis, and R. M. Woloshyn, Phys. Rev. **D71**, 094505 (2005), hep-lat/0503007.

[40] Alpha, R. Frezzotti, P. A. Grassi, S. Sint, and P. Weisz, JHEP **08**, 058 (2001), hep-lat/0101001.

[41] F. Farchioni, private communication.

[42] S. Weinberg, Phys. Rev. **166**, 1568 (1968).

[43] J. Gasser and H. Leutwyler, Ann. Phys. **158**, 142 (1984).

[44] J. Gasser and H. Leutwyler, Nucl. Phys. **B250**, 465 (1985).

[45] Particle Data Group, S. Eidelman *et al.*, Phys. Lett. **B592**, 1 (2004).

[46] S. L. Adler, Phys. Rev. **177**, 2426 (1969).

[47] J. S. Bell and R. Jackiw, Nuovo Cim. **A60**, 47 (1969).

[48] D. B. Kaplan and A. V. Manohar, Phys. Rev. Lett. **56**, 2004 (1986).

[49] S. Weinberg, Physica **A96**, 327 (1979).

[50] O. Bär, Nucl. Phys. Proc. Suppl. **140**, 106 (2005), hep-lat/0409123.

[51] K. Symanzik, Nucl. Phys. **B226**, 187 (1983).

[52] M. Lüscher, S. Sint, R. Sommer, and P. Weisz, Nucl. Phys. **B478**, 365 (1996), hep-lat/9605038.

[53] G. Rupak and N. Shoresh, Phys. Rev. **D66**, 054503 (2002), hep-lat/0201019.

[54] O. Bär, G. Rupak, and N. Shoresh, Phys. Rev. **D70**, 034508 (2004), hep-lat/0306021.

[55] G. Colangelo, Nucl. Phys. Proc. Suppl. **140**, 120 (2005), hep-lat/0409111.

[56] J. Gasser and H. Leutwyler, Nucl. Phys. **B307**, 763 (1988).

[57] D. Becirevic and G. Villadoro, Phys. Rev. **D69**, 054010 (2004), hep-lat/0311028.

[58] M. Lüscher, Commun. Math. Phys. **105**, 153 (1986).

[59] G. Colangelo and S. Dürr, Eur. Phys. J. **C33**, 543 (2004), hep-lat/0311023.

[60] G. Colangelo and C. Haefeli, Phys. Lett. **B590**, 258 (2004), hep-lat/0403025.

[61] G. Colangelo, S. Dürr, and C. Haefeli, (2005), hep-lat/0503014.

[62] G. Münster and C. Schmidt, Europhys. Lett. **66**, 652 (2004), hep-lat/0311032.

[63] S. Aoki, Prog. Theor. Phys. Suppl. **122**, 179 (1996), hep-lat/9509008.

[64] T. Blum *et al.*, Phys. Rev. **D50**, 3377 (1994), hep-lat/9404006.

[65] JLQCD, S. Aoki *et al.*, (2004), hep-lat/0409016.

[66] S. R. Sharpe and R. L. Singleton, Jr., Phys. Rev. **D58**, 074501 (1998), hep-lat/9804028.

[67] S. R. Sharpe and R. L. Singleton, Jr., Nucl. Phys. Proc. Suppl. **73**, 234 (1999), hep-lat/9808047.

[68] S. Aoki, Phys. Rev. **D30**, 2653 (1984).

[69] G. Münster, JHEP **09**, 035 (2004), hep-lat/0407006.

[70] G. Münster, C. Schmidt, and E. E. Scholz, Nucl. Phys. Proc. Suppl. **140**, 320 (2005), hep-lat/0409066.

[71] S. R. Sharpe and J. M. S. Wu, Phys. Rev. **D70**, 094029 (2004), hep-lat/0407025.

[72] S. R. Sharpe and J. M. S. Wu, Nucl. Phys. Proc. Suppl. **140**, 323 (2005), hep-lat/0407035.

[73] L. Scorzato, Eur. Phys. J. **C37**, 445 (2004), hep-lat/0407023.

[74] A. Morel, J. Phys. (France) **48**, 1111 (1987).

[75] C. W. Bernard and M. F. L. Golterman, Phys. Rev. **D46**, 853 (1992), hep-lat/9204007.

[76] C. W. Bernard and M. F. L. Golterman, Phys. Rev. **D49**, 486 (1994), hep-lat/9306005.

[77] S. R. Sharpe and N. Shoresh, Phys. Rev. **D62**, 094503 (2000), hep-lat/0006017.

[78] S. R. Sharpe and N. Shoresh, Phys. Rev. **D64**, 114510 (2001), hep-lat/0108003.

[79] S. R. Sharpe and R. S. Van de Water, Phys. Rev. **D69**, 054027 (2004), hep-lat/0310012.

[80] M. F. L. Golterman and K.-C. Leung, Phys. Rev. **D57**, 5703 (1998), hep-lat/9711033.

[81] S. R. Sharpe, Phys. Rev. **D56**, 7052 (1997), hep-lat/9707018, Erratum-ibid. **D 62**, 099901 (2000).

[82] J. Bijnens, N. Danielsson, and T. A. Lahde, Phys. Rev. **D70**, 111503 (2004), hep-lat/0406017.

[83] J. Bijnens and T. A. Lahde, Phys. Rev. **D71**, 094502 (2005), hep-lat/0501014.

[84] qq+q, F. Farchioni, C. Gebert, I. Montvay, E. Scholz, and L. Scorzato, Phys. Lett. **B561**, 102 (2003), hep-lat/0302011.

[85] H. Leutwyler, Nucl. Phys. Proc. Suppl. **94**, 108 (2001), hep-ph/0011049.

[86] S. Aoki, Phys. Rev. **D68**, 054508 (2003), hep-lat/0306027.

[87] S. R. Sharpe and R. S. Van de Water, Nucl. Phys. Proc. Suppl. **129**, 245 (2004), hep-lat/0308010.

[88] G. Münster, C. Schmidt, and E. E. Scholz, Europhys. Lett. **86**, 639 (2004), hep-lat/0402003.

[89] SPQcdR, D. Becirevic *et al.*, Nucl. Phys. Proc. Suppl. **140**, 246 (2005), hep-lat/0409110.

[90] N. Metropolis, A. W. Rosenbluth, M. N. Rosenbluth, A. H. Teller, and E. Teller, J. Chem. Phys. **21**, 1087 (1953).

[91] G. Bhanot, Rept. Prog. Phys. **51**, 429 (1988).

[92] R. T. Scalettar, D. J. Scalapino, and R. L. Sugar, Phys. Rev. **B34**, 7911 (1986).

[93] S. L. Adler, Phys. Rev. **D23**, 2901 (1981).

[94] S. L. Adler, Phys. Rev. **D37**, 458 (1988).

[95] F. R. Brown and T. J. Woch, Phys. Rev. Lett. **58**, 2394 (1987).

[96] M. Creutz, Phys. Rev. **D36**, 515 (1987).

[97] A. D. Kennedy and B. J. Pendleton, Phys. Lett. **B156**, 393 (1985).

[98] C. Gebert, *Light quark fields in lattice gauge theories*, PhD thesis, University of Hamburg, 2002, DESY-THESIS-2002-044.

[99] S. Duane, A. D. Kennedy, B. J. Pendleton, and D. Roweth, Phys. Lett. **B195**, 216 (1987).

[100] M. Lüscher, Nucl. Phys. **B418**, 637 (1994), hep-lat/9311007.

[101] C. Alexandrou, A. Borrelli, P. de Forcrand, A. Galli, and F. Jegerlehner, Nucl. Phys. **B456**, 296 (1995), hep-lat/9506001.

[102] I. Montvay, Nucl. Phys. **B466**, 259 (1996), hep-lat/9510042.

[103] C. Gebert and I. Montvay, (2003), hep-lat/0302025.

[104] S. D. Katz and B. C. Toth, Comput. Phys. Commun. **158**, 137 (2004), hep-lat/0401007.

[105] I. Montvay and E. Scholz, (2005), hep-lat/0506006.

[106] B. Jegerlehner, Nucl. Phys. Proc. Suppl. **53**, 959 (1997), hep-lat/9612013.

[107] DESY-Münster, I. Campos *et al.*, Eur. Phys. J. **C11**, 507 (1999), hep-lat/9903014.

[108] qq+q, F. Farchioni, I. Montvay, E. Scholz, and L. Scorzato, Eur. Phys. J. **C31**, 227 (2003), hep-lat/0307002.

[109] qq+q, F. Farchioni, C. Gebert, I. Montvay, E. Scholz, and L. Scorzato, Nucl. Phys. Proc. Suppl. **129**, 179 (2004), hep-lat/0309094.

[110] qq+q, F. Farchioni, I. Montvay, and E. Scholz, Eur. Phys. J. **C37**, 197 (2004), hep-lat/0403014.

[111] qq+q, F. Farchioni, I. Montvay, and E. E. Scholz, Nucl. Phys. Proc. Suppl. **140**, 249 (2005), hep-lat/0409004.

[112] CP-PACS and JLQCD, A. Ukawa, Nucl. Phys. Proc. Suppl. **106**, 195 (2002).

[113] UKQCD, A. C. Irving, C. McNeile, C. Michael, K. J. Sharkey, and H. Wittig, Phys. Lett. **B518**, 243 (2001), hep-lat/0107023.

[114] MILC, C. Aubin *et al.*, Phys. Rev. **D70**, 114501 (2004), hep-lat/0407028.

[115] J. Bijnens, G. Ecker, and J. Gasser, (1994), hep-ph/9411232, , also: *Chiral Perturbation Theory*, in *The DAΦNE Physics Handbook*, 2nd ed., eds. L. Maiani, G. Pancheri, and N. Paver, Frascati (1994).

[116] CP-PACS, Y. Namekawa *et al.*, Phys. Rev. **D70**, 074503 (2004), hep-lat/0404014.

[117] G. Colangelo, J. Gasser, and H. Leutwyler, Nucl. Phys. **B603**, 125 (2001), hep-ph/0103088.

[118] F. Farchioni *et al.*, Eur. Phys. J. **C39**, 421 (2005), hep-lat/0406039.

[119] F. Farchioni *et al.*, Nucl. Phys. Proc. Suppl. **140**, 240 (2005), hep-lat/0409098.

[120] C. Urbach, PhD thesis, Freie Universität Berlin, in preparation.

[121] C. Urbach, K. Jansen, A. Shindler, and U. Wenger, (2005), hep-lat/0506011.

[122] S. Dürr, Eur. Phys. J. **C29**, 383 (2003), hep-lat/0208051.

[123] S. R. Sharpe, Twisting vs. staggering: is twisted-mass lattice qcd a viable alternative to improved staggered fermions?, talk given at "Modern Challenges for Lattice Field Theory", KITP (2005).

[124] R. Frezzotti and K. Jansen, Phys. Lett. **B402**, 328 (1997), hep-lat/9702016.

[125] R. Frezzotti and K. Jansen, Nucl. Phys. **B555**, 395 (1999), hep-lat/9808011.

[126] R. Frezzotti and K. Jansen, Nucl. Phys. **B555**, 432 (1999), hep-lat/9808038.

[127] QCDSF, R. Horsley, H. Perlt, P. E. L. Rakow, G. Schierholz, and A. Schiller, Nucl. Phys. **B693**, 3 (2004), hep-lat/0404007, Erratum-ibid. **B713**, 601 (2005).

[128] P. Weisz, Nucl. Phys. **B212**, 1 (1983).

[129] P. Weisz and R. Wohlert, Nucl. Phys. **B236**, 397 (1984).

[130] M. Lüscher and P. Weisz, Commun. Math. Phys. **97**, 59 (1985), Erratum-ibid. **98**, 433 (1985).

[131] M. Lüscher and P. Weisz, Phys. Lett. **B158**, 250 (1985).

[132] K. G. Wilson and J. B. Kogut, Phys. Rept. **12**, 75 (1974).

[133] QCD-TARO, P. de Forcrand *et al.*, Nucl. Phys. Proc. Suppl. **53**, 938 (1997), hep-lat/9608094.

[134] T. Takaishi, Phys. Rev. **D54**, 1050 (1996).

[135] Y. Iwasaki, UTHEP-118 , unpublished.

Acknowledgments

In the first place, I want to thank my supervisor Prof. Dr. István Montvay for offering me such an interesting topic. He always took the time to explain the little details as well as broader context of the project, and he started many interesting and stimulating discussions.

Also, I would like to thank the people from the qq+q Collaboration and the twisted mass study: Prof. Dr. István Montvay, Prof. Dr. Gernot Münster, Prof. Dr. Karl Jansen, Dr. Federico Farchioni, Dr. Luigi Scorzato, Dr. Claus Gebert, Dr. Naoya Ukita, Dr. Ines Wetzorke, Dr. Andrea Shindler, Dr. Urs Wenger, and Carsten Urbach for many interesting discussions, sharing the work, and debugging various lines of computer code. Many thanks for special discussions on the twisted mass formulation go to Prof. Dr. Giancarlo Rossi and Dr. Roberto Frezzotti.

I am very grateful to Dr. Hartmut Wittig, who organized a lot of interesting "Lattice Discussion Forum"-sessions with enlightening talks and discussions, as well as to all the other participants of the forum.

The numerical simulations were done in part at DESY Hamburg and Zeuthen and at the NIC in Jülich. I acknowledge the support from the various IT-staff-members.

A big "thank you" to Stefan Ukena and Focko Meier for the careful proofreading of the manuscript.

For the excellent atmosphere at the office 2a.306 at the DESY campus I want to thank Dr. Huitzu Tu, Prof. Dr. Barbara Schrempp, Lily Schrempp, Tobias Kleinschmidt, and Dirk Brömmel; also many thanks to all the other staff members, secretaries, post-docs, Ph.D.- and Diploma-students of the DESY and University Theory Groups.

The financial support by DESY Hamburg is gratefully acknowledged.

Oodles of thanks go to Silvia Kloster, Focko Meier, Simone Ukena, and Stefan Ukena for many evenings full of fun with good wine and delicious food.

Most of all, I want to thank my parents, Gerhard and Fentke Scholz, for their continuous love and support.